

## ENERGY METER TO PREVENT ELECTRICITY THEFT BY POWER TAPPING WITH AUTOMATIC BILLING FACILITY

P.Jamodkar<sup>1</sup>, P.Kumbhare<sup>2</sup>, S.Kubde<sup>3</sup>, S. Sahasrabuddhe<sup>4</sup> and N.D.Ghawghawe<sup>5</sup>

Government College of Engineering, Nagpur

<sup>1</sup>jamodkarpranjali@gmail.com, <sup>2</sup>kumbharep628@gmail.com

### ABSTRACT

*The energy lost during distribution due to pilferage or theft by diverting electricity i.e., taking illegal connections from the distribution lines using hooks causes a loss of revenue of crore rupees in India. The world annually loses billions of dollars due to illegal access of electricity. Implementing a modified energy meter eliminates this energy theft done by diverting electricity i.e., power tapping or cable hooking. This is achieved by sending a relatively higher voltage than 230V (around 300 V) using tap changers on transformers or power stations, substations for some duration which will trip or damage the devices of unauthorized users, but the modified energy meter for authorized users will lower the voltage values within acceptable limits using thyristor-based control. Incorporating the automatic billing facility using a radio frequency transceiver (RF) module saves the revenue lost due to corruption of meter reading personnel to show lesser bills, revenue lost in payment of manpower required for meter reading and avoids the inconvenience caused to consumers due to incorrect meter readings and errors in electricity bill. It also disconnects the electricity supply to the consumer in case of failure of timely payment of electricity bill.*

**Keywords:** Anti-theft energy meter, Automatic Meter Reading, by-passing connection, Cable hooking, Energy Meter, Electricity Pilferage, Power Tapping, RF module

### Introduction

Between power generation and distribution, there are two types of losses, namely technical and non-technical loss. Technical loss is the loss in transmission and distribution lines, whereas non-technical loss includes loss due to energy theft, pilferage, or unauthorized usage of electricity. Electricity theft is done by different methods:

1. Diverting electricity by taking illegal connections from distribution lines.
2. Tampering meters or Bypassing connection from the meter.
3. Corruption of meter reading personnel to show lesser bills causing loss of revenue.

The existing technologies that aim to estimate power theft collect the data from the transformer side and consumer side. This data is then compared and the difference between the two values gives the amount of energy lost. However, the drawbacks of the existing technologies are that they only give the estimated amount of energy theft but neither control the theft nor regulates it. The mode of electricity theft of power tapping (diverting electricity by taking direct connection from distribution line using hooks) constitutes around 80% of power theft which is not addressed in the existing systems. Similarly, the currently used method of manual reading of

electricity meters involves a meter reading personnel visiting every meter location periodically and reading the meter value manually. For meter reading, electric impulse counting is done and the readings are given to the electricity board. The information is recorded by a meter reading photo provided to the data collection office. Thereafter the details of the photo taken are entered in the database for billing. Then the bill is generated. This process requires a great amount of manpower and resources and poses scope of human errors. To overcome these problems, an anti-theft energy meter to prevent electricity theft along with automatic meter reading and billing facility is to be implemented. This will completely eliminate electricity theft by power tapping permanently and the automatic billing facility will avoid revenue lost due to corruption, discrepancy due to human error and also save manpower required for a meter reading.

### Methodology

The first step is to issue a warning to all unauthorized users to get legal connections and a modified anti-theft energy meter. A sufficient time frame will be given to implement the guidelines. Consumers will be warned about the consequences of damage to their domestic electrical appliances if they fail to get legal

connections and meters. Every authorized user will get the modified anti-theft energy meter.

All the domestic appliances are designed to operate at 220 V to 240V which is received from distribution lines. If the voltage varies beyond the acceptable voltage limit, the devices/appliances may trip or damage. The next step is to send a relatively higher voltage of around 300V to 320 V for a small duration through distribution lines by changing tap changers of transformers at substations. The devices of all the consumers who do not have modified anti-theft energy meters will be subjected to 320 V and thus their devices will trip or may get damaged. However, the anti-theft energy meter of the authorized users is modified to have a thyristor-based microcontroller action that will step down the voltage to the acceptable limits of 220V to 240V thus keeping balanced voltage across the load and ensuring smooth operation of all devices.

The incoming AC voltage from distribution lines is sent to a step-down transformer. The step-down transformer steps the voltage down to 12V AC, which is further sent to a rectifier to get 12 V pulsating DC. This pulsating DC is filtered to get 12 V pure DC using a filter capacitor. Since the microcontroller PIC 16886, LCD, and RF module operate at 5V DC, thus a regulator IC LM7805 is used to convert 12V DC to 5V DC. The 5V DC from the output of regulator IC is also stored in another capacitor to the fulfilled excessive requirement of charge in case overloading of regulator IC, causing the voltage to drop below 5V which may cause the microcontroller to reset. A ceramic capacitor and resistor are used to reset the microcontroller when it is switched ON.

When the incoming voltage from distribution lines increases beyond 240 V, a zero-crossing detection circuit indicates the starting points of positive and negative half cycles of incoming sinusoidal voltage for input to the microcontroller. Based on this input, the microcontroller increases the firing angle when the incoming voltage increases. An optocoupler is used to maintain electrical isolation between high voltage and low voltage sides of the energy meter. The microcontroller sends a triggering command to TRIAC through

this optocoupler. The triggering time of TRIAC decreases with an increase in firing angle causing the TRIAC output voltage to decrease. This voltage is then measured through the potential transformer and stepped down. Further, a rectifier is used to convert the AC input to DC output. As the microcontroller only accepts input less than 5V DC, a potential divider, potentiometer arrangement is used to divide the voltage by 100 to be used as input to the microcontroller. The input value is then multiplied by 100 inside the microcontroller to get the actual voltage value. If this value of voltage is not between 220 V to 240 V, then the microcontroller again changes the firing angle and triggers the TRIAC. This process is repeated until the voltage is within the acceptable limit of 220 to 240V. The voltage is then displayed on the LCD screen. An RC snubber circuit is used to compensate regenerative emf. The voltage and current through the current transformer are used to calculate the power. The microcontroller converts the information in a readable manner and displays the voltage, current, average power, energy usage, and bill amount on the LCD. MP LAB IDE is used for programming. The protocol followed for automatic billing is that, first the receiver section of the energy meter listens for requests. When the request is received, the microcontroller program checks the validity of the header information. The meter ID is extracted from the received data and is compared to the ID in the software database. The energy meter reading is transmitted in the form of packets from the transmitter section. From the base station, a single meter can be selected by clicking on the icon corresponding to each consumer's unique consumer ID. The software displays instantaneous readings for the selected meter. Complete meter information such as the meter address, meter ID, owner's name, last read date, last bill paid, current account, etc. is stored in the database and can be viewed or edited. The PC software uses the parameters of energy meter reading, the fixed cost, the cost per KWh, tariff, and VAT to calculate the current month's bill. This information is obtained from the database. The software has tabs to read the meter, generate the bill. The meter usage chart, meter information, and customer's statement of

account can also be retrieved from the information stored. The communication technique used is RS-232 interface which serves as a link between the main computer running the billing software and the receiving unit in the base station. The microcontroller program is implemented using the integrated development environment (IDE) Keil  $\mu$  Vision version 3. The total power consumed is sent to the server via the radio frequency (RF) module. All the transmitters from the consumers' end send data to the RF receiver. After collecting all data, the RF receiver is connected to the PC with the help of MAX 232 port. Automatic Meter Reading via Radio 4 Frequency (RF) remotely gathers the electricity consumption data from consumers' meters employing radio frequency technology thus improving the efficiency due to remote communication. The PC uses a central database

for billing and analyzing and displays the customer ID and current consumption in units and calculates the exact billing amount. The receiver module is ported onto a server, computer/laptop to display the meter reading, bill, and bill payment status for each consumer. Automating the meter reading procedure and providing all-inclusive data to the electricity board improves the efficiency of the electricity billing system. Based on the tariff set on the computer, the bill is generated. This bill is displayed on the LCD on the energy meter. A timer starts the countdown for 10 days within which the bill must be paid. If the consumer fails to pay the bill within the stipulated time, the connection will be disconnected using a relay through the microcontroller. The relay operates at 12 V DC thus, a driver IC is used to convert 5 V from the microcontroller to 12 V for input to relay.

**2.1 Block Diagram & Circuit Diagram**

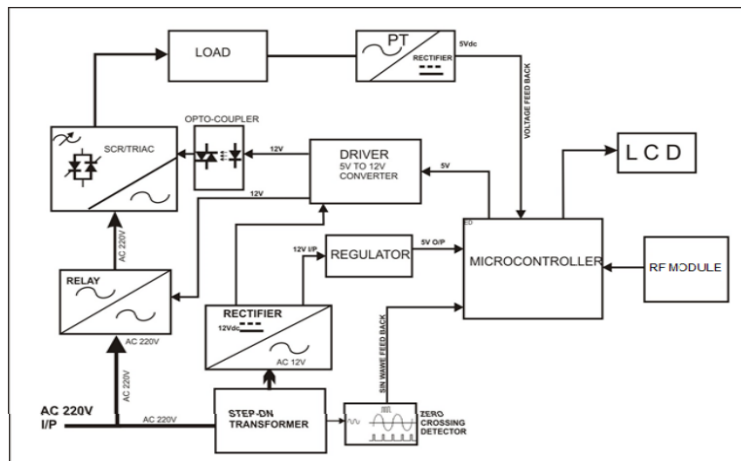


**Figure.1 Block Diagram**

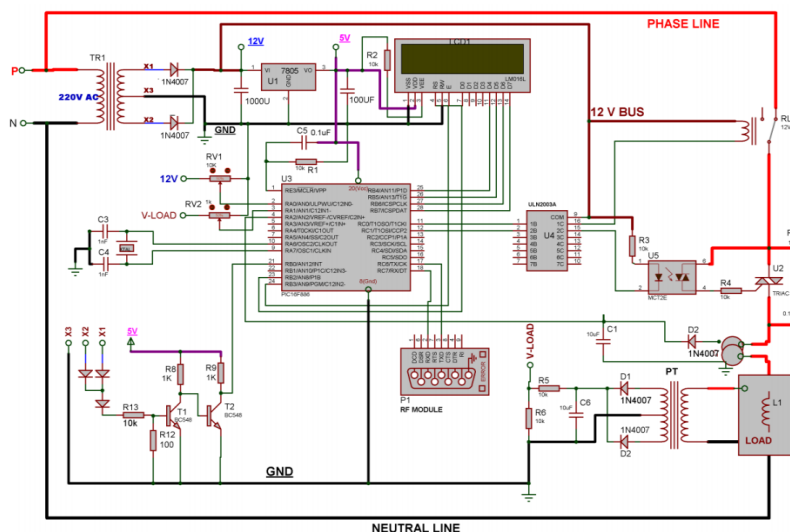


**Figure 2. Circuit Diagram**

**2.1 Results**

For practical applications, the meter will be designed to record the units consumed for one month, but to represent the results in the hardware model proposed, it gives the consumption reading for one minute proportionate to one month. Similarly, the duration of 30 seconds in the hardware model is set proportionately to the 10 days in actual implementation for the bill payment deadline. Tariff is set to Rs. 2/- in the computer system

for bill calculation. The software displays each user's unique consumer ID and also has options to turn the meter ON or OFF based on the status of bill payment.

Parameter	Results displayed on LCD screen
Voltage (in V)	238V
Current (in Amperes)	0.4 A
Power used (in Watts)	102 W
Bill generated (in Rupees)	Rs. 204/-

**Table 1. Output**



**Figure 3. Setup in Working Mode**

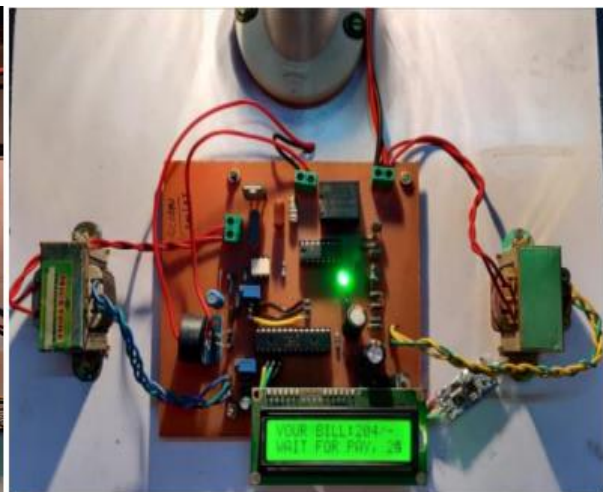


**Figure 4. Bill displayed on the energymeter at the end of the month and countdown begins for time left for payment of bill**

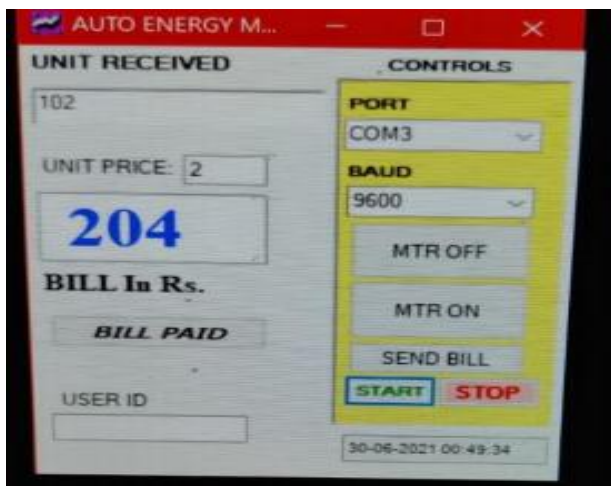


**Figure 5. Unit consumption received on interfaced computer for each user based on unique consumer ID payment**

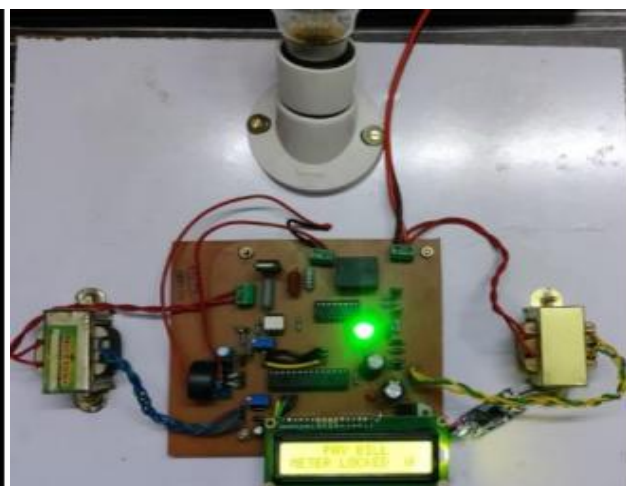


**Figure 6: Energy meter blocked in case of failure of electricity bill.**



**Figure 7. LCD displaying voltage ,current and wattage reading**



**Figure 8: LCD displaying Bill amount**



**Figure 9. LCD displaying message “Meter locked” when previous month bill is unpaid**

### 2.2 Merits

1. Power theft due to cable hooking, which constitutes around 80% of total power theft is completely eliminated.
2. Energy theft can be monitored and controlled at any instant of time in the future without the need for any additional arrangements.
3. Electricity connections can be cut if the user fails to pay electricity bills on time.
4. Eliminates the manual meter reading.
4. Gives accurate meter reading in real-time.
5. Improves reading schedule and reduces delay in bill payments.
6. Running and maintenance cost is low.

### 3 Conclusion

Testing is completed to make sure that the reduction of relatively higher voltage levels to permissible limits is ensured so that devices are not damaged. Tripping is provided in case if voltage exceeds the permissible range. The integration between transmitter and receiver is proper

### References

1. Wikipedia Page (08/05/2021) [Online] available: [http://en.wikipedia.org/wiki/Automatic\\_meter\\_reading](http://en.wikipedia.org/wiki/Automatic_meter_reading)
2. Bharath P., Ananth N, Vijetha S, Jyothi Prakash K.V., “Wireless Automated Digital Energy Meter”, IEEE 2008.
3. A. Ali, N.A. Razali, N.H. Saad, N. Vitee., “Implementation of Automatic Meter Reading (AMR) Using Radio Frequency (RF) Module”, IEEE 2012
4. Shital S. Bobade, Vibhuti S. Jadhav, Anuja A. Mokal, Prof Mrs. K. D. Mahajan, “Automatic Energy Meter Billing System with Theft Detection”, IRJET 2016
5. Wikipedia Page (08/05/2021) [Online] available: <https://en.wikipedia.org/wiki/MAX232>
6. International Journal of Scientific and Engineering Research, Volume 6, Issue 10, October- 2015 ISSN 2229-551

## INTEGRATED ASSESSMENT OF URBAN MICROCLIMATE PARAMETERS USING OPEN FOAM

S.Mirza <sup>1</sup>, A.Niwalkar <sup>2</sup>, S.Anjum <sup>3</sup>, H.Bherwani <sup>4</sup>, A.Singh <sup>5</sup> and R.Kumar <sup>6</sup>

<sup>12346</sup>CSIR-National Environmental Engineering Research Institute, Nagpur-440020, Maharashtra, India

<sup>46</sup>Academy of Scientific and Innovative Research (AcSIR), Ghaziabad-201002, Uttar Pradesh India

<sup>5</sup>National Institute of Industrial Engineering (NITIE), Mumbai -400087, Maharashtra, India

<sup>4</sup>h.bherwani@neeri.res.in

### ABSTRACT

*The growing population of cities necessitates dense and fascinating building systems. As a result, the green spaces of urban societies are reducing day by day. Global warming and pollutant release are primarily caused by anthropogenic activities in correlation with infrastructure development. Urban dwellers are suffering as a result of ignoring the urban heat island effect. To better regulate these fundamental issues, it is necessary to study the microclimatic change in urban areas. Using OpenFOAM, the current study attempts to develop a mechanism for dealing with changes in microclimate caused by dense infrastructure. OpenFOAM is a free (Computational Fluid Dynamics)CFD modelling software that works for a variety of fluid flows. The study can deal with a variety of microclimatic variables such as wind speed, air temperature, building temperature, heat transfer, and wind direction, with a particular emphasis on vegetation cooling effects. A comparison of OpenFOAM modelling with real-time onsite monitoring is attempted in this study. With the uncertainty of 0.03 to 0.05 in the calculation of OpenFOAM, modelling results of wind speed and air temperature behave exactly like actual monitoring results. The results of the study will provide urban planners with expertise and strategies for reducing heat stress in cities*

**Keywords:**CFD, Heat Transfer, Microclimate, OpenFOAM, Urbanization, Vegetation, Wind flow

### Introduction

The growing population of cities necessitates dense construction and intricate structures. Urban areas, in comparison to rural areas, have the most cost-effective services, but people need a high level of energy consumption to meet their needs, which results in an increase in heat emissions and causes global warming through GHG emissions (Gagliano et al., 2017; Veenae et al. 2020). According to World Population Prospects (2015), the current scenario stated that the global urban population has crossed the 50 percent mark, and by 2050, it is projected to cross 66 percent. The use of local resources and the construction of infrastructure raises the temperature of the urban area concerning the surrounding rural area, a phenomenon known as Urban Heat Island (UHI) (Howard, 1820). The dense building systems in urban areas are to blame for the rise in air temperature caused by UHI. When a warm environment is supposed to be considered for the outdoor air, the UHI effects are usually underestimated in the study of indoor environments, but they can be a significant factor (Bueno et al., 2013; Mackey et al., 2017).

Fluctuations in wind patterns and reduced wind velocity are caused by the dense structures in

the urban areas, leading to lower convective heat exchange and lower energy losses due to heat stuck in the sub-atmospheric layer at night. These factors have a direct impact on building energy consumption because they affect conductive heat transfer and energy exchange by ventilation, necessitating the use of passive design at night-time (Santamouris et al., 2001; Kolokotroni et al., 2006; Allegrini et al., 2012; Ghiaus et al., 2006). Since they change wind flow patterns and increase air temperature, urban building systems contribute to changing the local microclimate (Allegrini et al., 2013; Bherwani et al., 2020). Urban dwellers are experiencing serious issues such as heat cramps, heat exhaustion, heatstroke, and human distress as a result of the Urban Heat Islands impact, which raises the temperature in metropolitan cities. The UHI effect can be determined by determining the UHI intensity factor, which indicates temperature differences between the urban and rural areas (Chen et al., 2014; Taha, 2017). The temperature of dense building structures contributes to higher surrounding ambient temperature in urban areas due to the high emissivity of building materials (Bherwani et al., 2021; Nair et al., 2020).

Verma (2009) investigated the impact of various wind speeds on the statured buildings. The wind movement around buildings and other terrains such as hills and parks are directly affected by temperature. Several researchers have devised methods and techniques for analyzing wind movement through dense structures and peaks (Dhunni et al.; Murakami, 1998; Stathopoulos and H. Wu, 2004; Costola et al., 2009). The use of OpenFOAM is one of the methods for studying the wind flow pattern over single and multiple buildings, as well as the effect of temperature behind the complex structure (Veena et al., 2016; Veena et al.; Diego et al., 2009; Borges and Viegas, 1988; Smitham, and Nicol, 1991; Yoon and Patel, 1996).

The main purpose of this study is to show that microclimatic parameters such as wind velocity, wind direction, and ambient temperature can be dealt with using OpenFoam, a CFD software. The real-time monitoring of temperature, wind velocity and wind direction is carried out using a temperature sensor, humidity sensor and anemometer and likewise, simulation is executed using OpenFOAM in the CSIR-NEERI (National Environmental Engineering Research Institute), Nagpur, India. Researchers in most microclimatic studies undervalue the importance of considering vegetation impact in their study. The influence of vegetation on microclimatic parameters around building structures is investigated in this study. It is a small attempt to compare and interpret the Openfoam findings with the actual monitoring data through this analysis.

### Research Methodology

In the present study, to analyse and predict the effect of infrastructure on the surrounding environment, CFD simulations with an open-source software OpenFOAM is carried out. In consideration of buildings as the highest temperature, the buildings are considered to be a source of temperature in this modelling. In this work, the wind has been flowing from different directions according to the meteorological updates. The interaction of

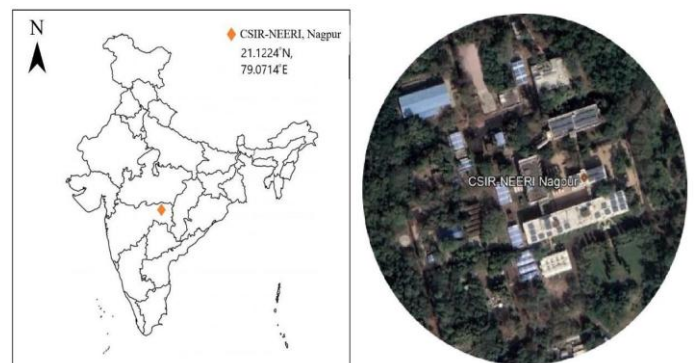
wind with the warmed building structures and trees has been analysed. In this section, the detailed description of selected areas for modelling with the CFD setup is discussed.

### Study Area

For the present study, a part of CSIR-NEERI, Nagpur, India is selected. It is situated in the central part of India in Nagpur city, having rapidly increasing urbanization and population (Chavan et al., 2015). The reason for choosing this area is the highly built-up infrastructure surrounded by dense greenery so that the effect of concrete buildings, as well as vegetation, can be studied. Nagpur is listed in the top 10 fastest economically growing cities over the globe. In summer, Nagpur city temperature generally reaches up to 48 °C (Bhonsle, 2010). Because of this, the built-up infrastructure is getting warm unexpectedly. As Nagpur is an arid region so there is an adequate temperature variation throughout the day. Figure 1 represents the selected study area with an India map and aerial view.

Figure 1

India map showing study area (left) aerial view of the study area (right)



### Field Monitoring

Wind speed and ambient air temperature onsite monitoring is carried out using specific weather instruments. For the validation with OpenFOAM models, dissimilar area points are chosen like greenery areas, paved surfaces, sunny and shadow areas. The onsite monitoring is carried out for six consecutive days from March 19, 2020, to March 24, 2020. There are 20 points selected for the measuring of wind speed and air temperature which can be seen with a white polygon in Figure 2. The weather instruments used for the onsite monitoring are listed in Table 1. Figure 2

Point locations in the study area for the analysis



Table 1  
Instruments used for onsite monitoring

Parameter	Instrument	Details	Remark
Temperature	Thermographic camera (TestoT-868)	Emissivity range: 0.01-1 Accuracy: ± 2%	Emissivity was adjusted as per the literature (Usament iaga, 2014).
Wind speed	Vane type anemometer (Extech AN100)	Range: 0.3–30 m/sec Accuracy: ± 3%	Readings are taken at a height of 1.5 m

**CFD Model Setup**

Reynolds-Averaged Simulation (RAS) turbulence model is used for all the simulations. There are three regions in this model with different properties hence CHT multi-region solver is used for modelling. This solver is generally used for the analysis of conduction, transient fluid flow, turbulence and

heat transfer between regions. Table 2 is showing all the parameters and boundary conditions used in this study.

Table 2

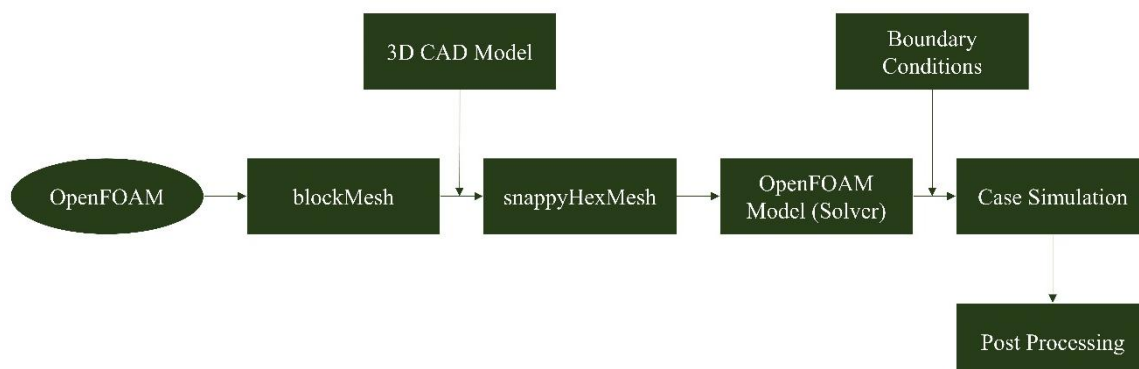
Boundary conditions and the input parameter

Parameter	Summary
Study area	14,308 square meters
Block mesh dimension	length = 300, width = 300, height = 50
Reynolds number	4,71,688
Physical model	RAS Turbulence
Temperature range	288.15 K to 318.15 K
Wind Speed range	0.54 m/s to 0.86 m/s
Emissivity of concrete	0.85
Emissivity of vegetation	0.94

The governing equations used in this modelling are mainly derived from the fundamental laws. The continuity equation followed by conservation of linear momentum and conservation of energy is the equations used in series. Then comes a final equation, which describes the solid-fluid relationship known as coupling equation (elAbbassia et al., 2017; Aguerre et al., 2018; Moukalled et al., 2016; Veena, et al., 2016). The overall workflow of the modelling of the present study can be illustrated in Figure 3.

Figure 3

OpenFOAM Workflow of the present study

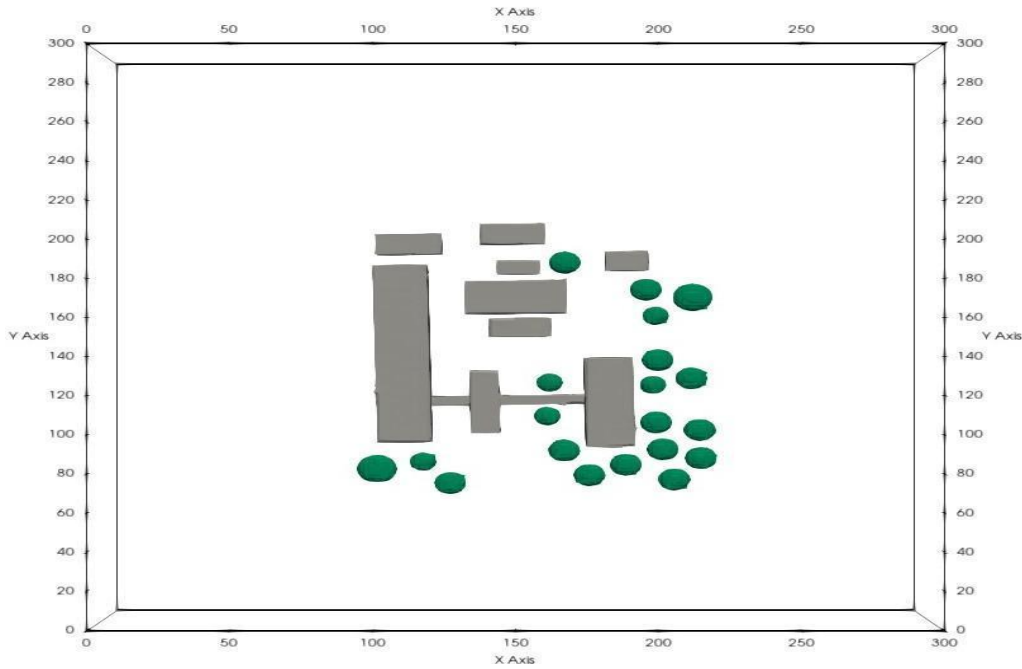




Buildings and trees 3D geometry has been created using an open-source CAD software ‘Blender’. The file of the 3D model is exported in stereolithography (.stl) format. With the help of the ‘blockMeshDict’ utility of OpenFOAM, the block in which the whole model is

supposed to be considered is generated. Outlined blockMesh with required dimensions and meshed model of the buildings and trees can be seen in Figure 4. Green and grey coloured objects shown are the models of trees and buildings respectively.

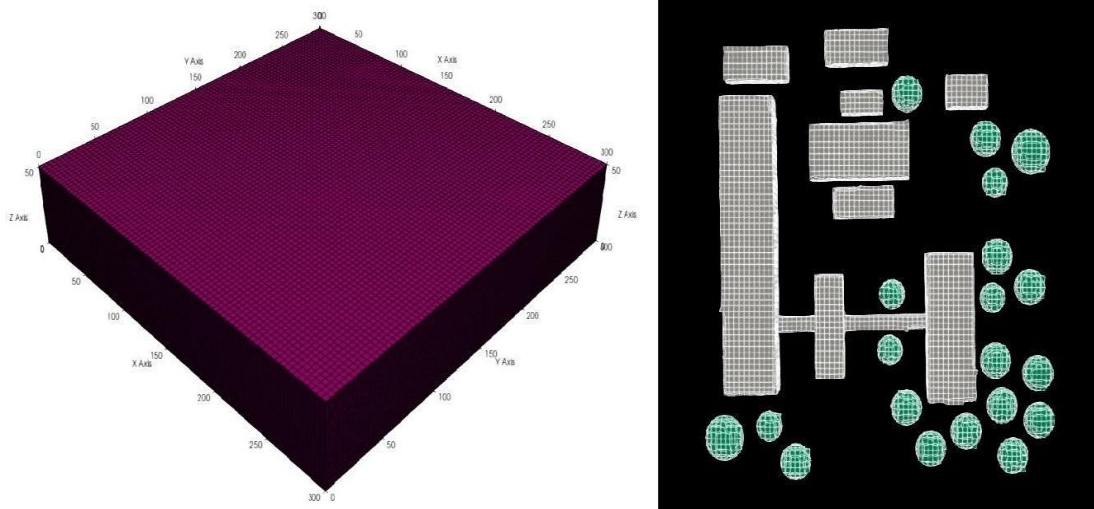
Figure 4  
Block-Mesh with required dimensions and 2D mesh



The left side of Figure 5 shows the block mesh of the needed dimensions. The model of buildings and trees have then meshed with the OpenFOAM meshing utility ‘snappyHexMesh’. With this utility, a model

created in the geometry tool overwrites the Block-Mesh. The right side part of Figure 5 is showing the refined meshed model of the buildings and trees with white and green coloured edges respectively.

Figure 5  
Block-Mesh of OpenFOAM (left) and refined mesh 3D models (right)



**Results**

**Solver Validation**

The validation study is conducted for wind flow over the two separate buildings. The two buildings of height 18 m separated by 4 m passage with experimental and numerical results are considered for validating the OpenFOAM model for wind flow analysis as shown in Figure 6.

Figure 6

Solver Validation setup: schematic view (left) and wind profile (right)

Reynolds number	4,71,688
Physical model	RAS Turbulence
Temperature range	288.15 K to 318.15 K
Wind Speed range	0.54 m/s to 0.86 m/s
Emissivity of concrete	0.85
Emissivity of vegetation	0.94

The governing equations used in this modelling are mainly derived from the fundamental laws. The continuity equation followed by conservation of linear momentum and conservation of energy is the equations used in series. Then comes a final equation, which describes the solid-fluid relationship known as coupling equation (elAbbassia et al., 2017; Aguerre et al., 2018; Moukalled et al., 2016; Veena, et al., 2016). The overall workflow of the modelling of the present study can be illustrated in Figure 3.

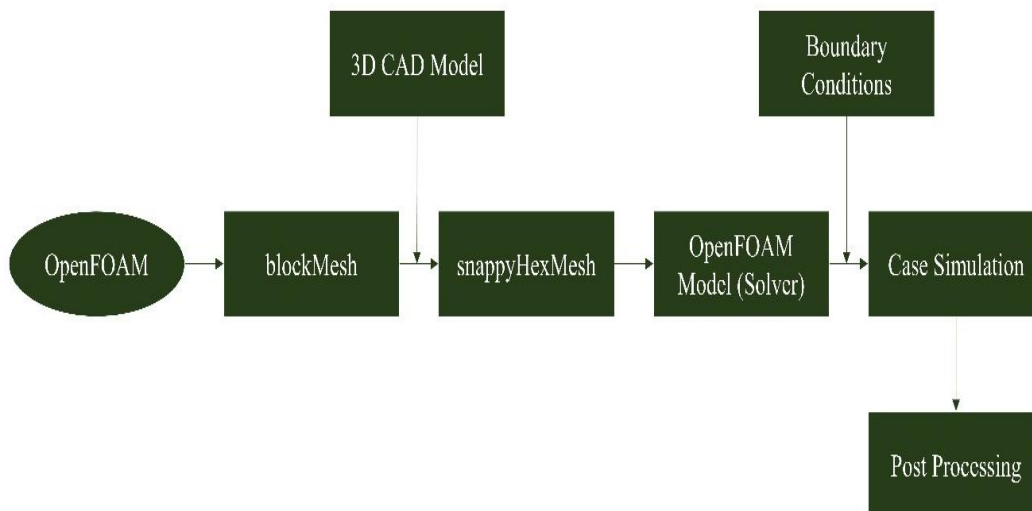
Table 2

Boundary conditions and the input parameter

Parameter	Summary
Study area	14,308 square meters
Block mesh dimension	length = 300, width = 300, height = 50

Figure 3

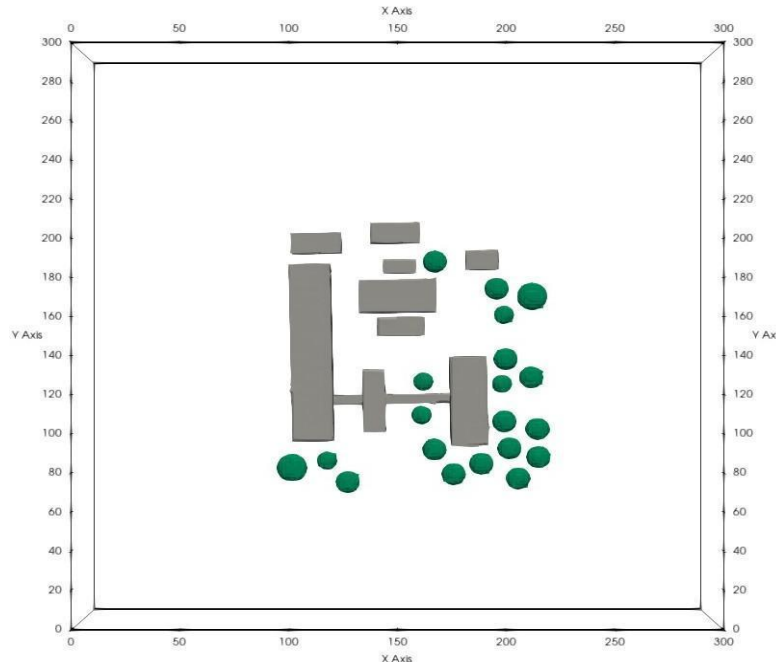
OpenFOAM Workflow of the present study



Buildings and trees 3D geometry has been created using an open-source CAD software ‘Blender’. The file of the 3D model is exported in stereolithography (.stl) format. With the help of the ‘blockMeshDict’ utility of OpenFOAM, the block in which the whole model is

supposed to be considered is generated. Outlined blockMesh with required dimensions and meshed model of the buildings and trees can be seen in Figure 4. Green and grey coloured objects shown are the models of trees and buildings respectively.

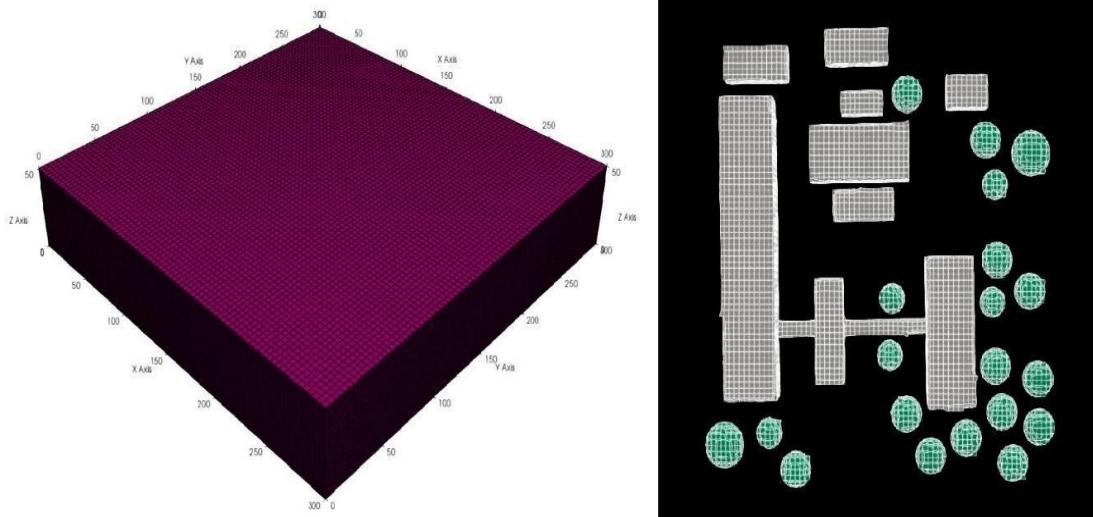
Figure 4  
Block-Mesh with required dimensions and 2D mesh



The left side of Figure 5 shows the block mesh of the needed dimensions. The model of buildings and trees have then meshed with the OpenFOAM meshing utility ‘snappyHexMesh’. With this utility, a model

created in the geometry tool overwrites the Block-Mesh. The right side part of Figure 5 is showing the refined meshed model of the buildings and trees with white and green coloured edges respectively.

Figure 5  
Block-Mesh of OpenFOAM (left) and refined mesh 3D models (right)



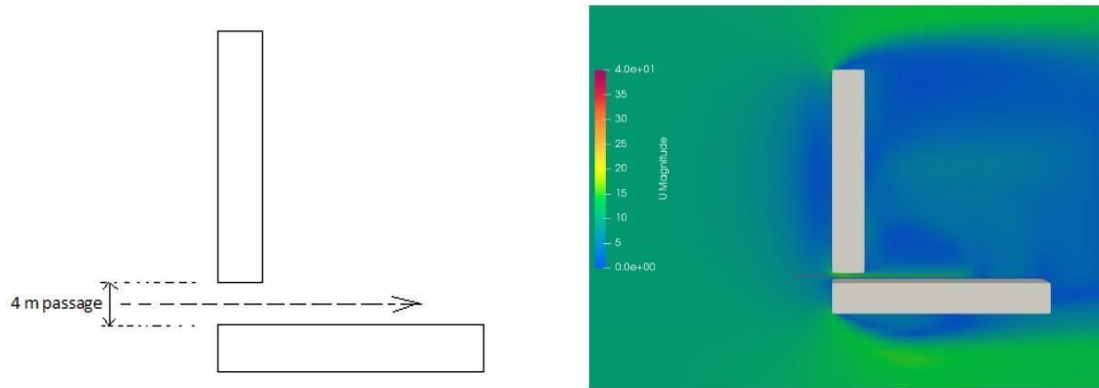
**Results**

**Solver Validation**

The validation study is conducted for wind flow over the two separate buildings. The two buildings of height 18 m separated by 4 m

passage with experimental and numerical results are considered for validating the OpenFOAM model for wind flow analysis as shown in Figure 6.

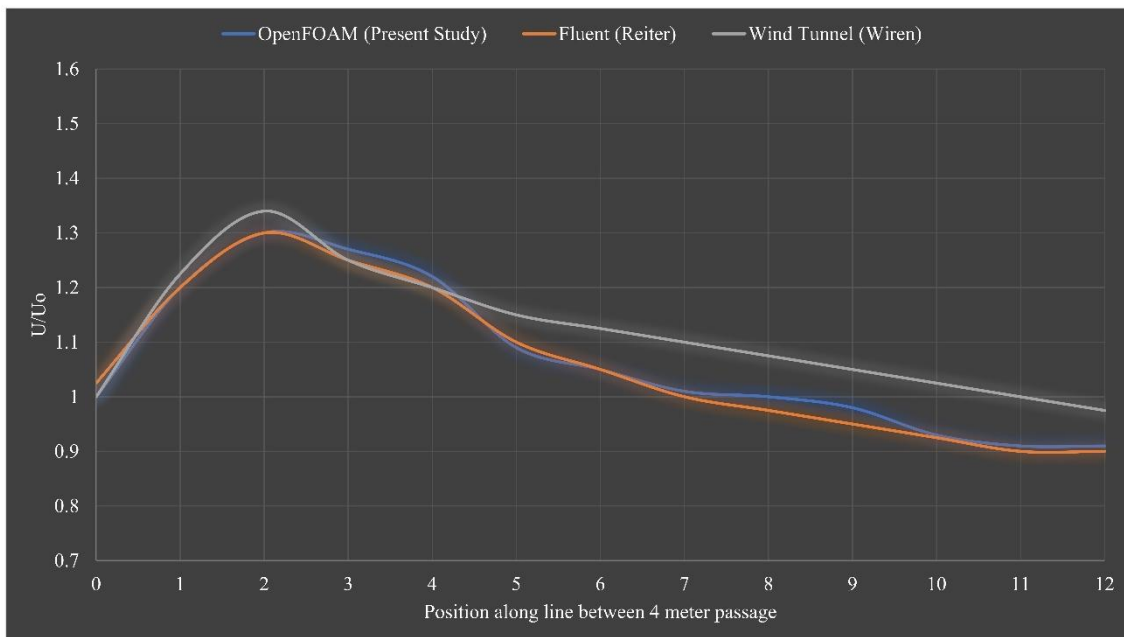
Figure 6  
 Solver Validation setup: schematic view (left) and wind profile (right)



In OpenFOAM, the Reynolds Averaged Simulation (RAS) turbulence model is used for the present study. The result of the RAS turbulence model is then compared with the result of the Fluent and Wind Tunnel test (Reiter, 2008; Wiren, 1977). In Figure 7, the ratio of wind velocity to the free stream velocity ( $U/U_0$ ) is plotted at the different points along the 4 m passage between the two

buildings. Veena, K., et al. elucidated, if the graph of  $U/U_0$  vs. position represents a similar pattern of corresponding references then the model is validated with the study. As it can be seen in Figure 5, the OpenFOAM result shows a similar pattern compared to corresponding studies verifying the current OpenFOAM model is valid.

Figure 7  
 Validation for wind flow showing normalized velocity variation

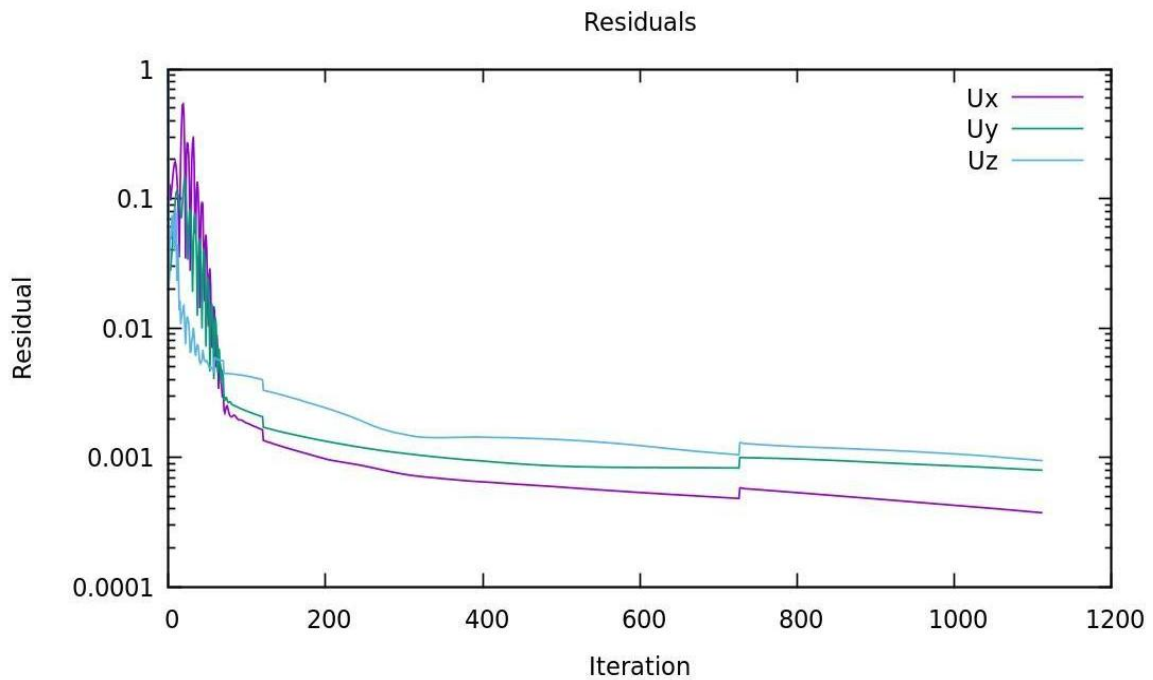


**Mesh Validation**

The numerical simulation approach of mesh independence is described in **Figure 8**. CHT multi-region RAS simulations are carried out using the ‘chtMultiregionFoam’ solver. The criterion for residual convergence is taken as  $10^{-3}$ . Here the components of velocity

produced the sinusoidal pattern from 0 to 18 iterations and residuals have dropped to  $10^{-3}$  and then flattened up. The variation for internal iteration convergence is found from 0.4 to 0.001. It can be seen from the residual plot that all the residuals are decreasing and getting constant with the number of iterations which shows the simulation results are converging.

Figure 8  
Residual plot for RAS turbulence simulation on the fine mesh

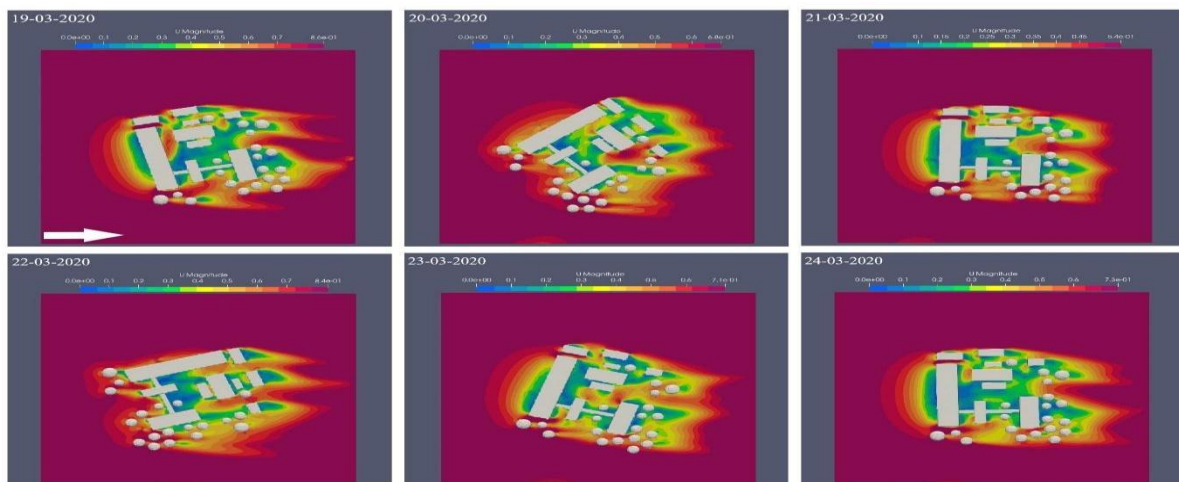


**Post Processing of Results**

Results have been viewed and analysed using an open-source post-processing software ‘ParaView-V5.6’. The different types of scenarios have been observed successfully. All the velocity results are analysed through the ‘Rainbow Uniform’ colour map. Contour plots of all the velocities are taken at 1.5 m height of the mesh along the XY-plane which can be seen in Figure 9. A white arrow on the lower-left corner of the first image shows the direction of wind flow over the model. The magnitude of the air velocities can be illustrated by the scales present on the top of

each plot with colour range. The dark red pattern represents the highest velocity magnitude while the blue one is for the lowest velocity magnitude. As seen in Figure 9, due to the interaction of wind with the objects (buildings and trees) the magnitude of velocities suddenly drops. The central part of each plot shows the minimum velocity magnitude because of fewer free spaces. Furthermore, after travelling enough parts of objects, the magnitude of wind velocities is recombined again and flows with the input corresponding velocities.

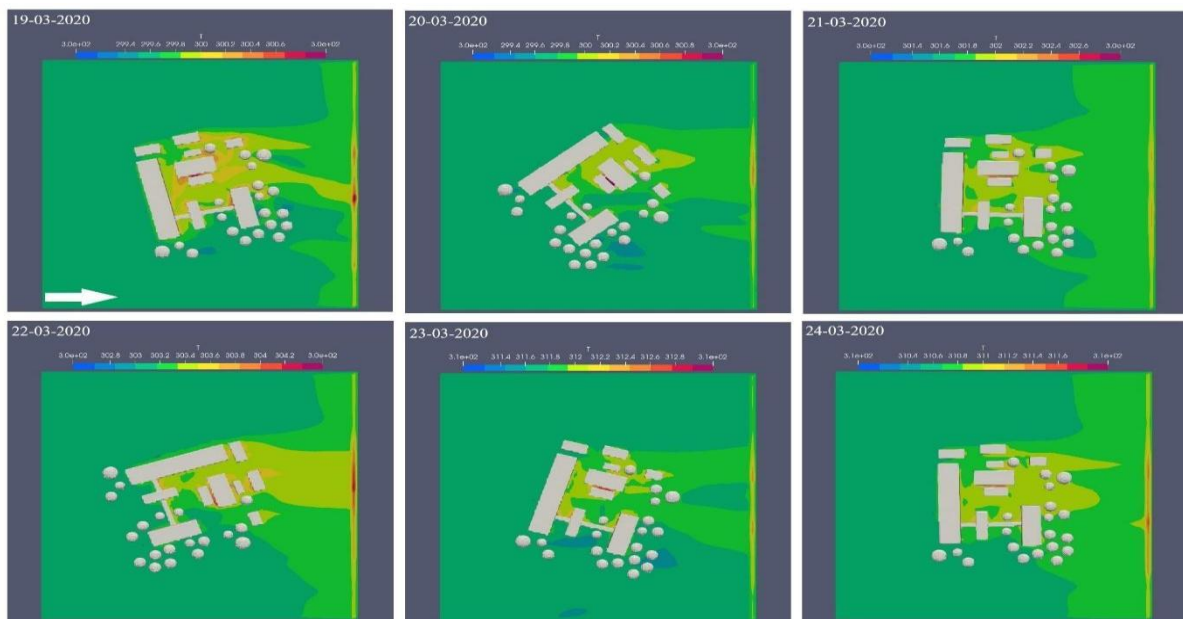
Figure 9  
Contour plots of velocities for all the days



Similarly, the temperature contours are plotted along the XYplane at a 1.5-meter height of corresponding meshes. 'Uniform Rainbow' colour maps are used to represent temperature plots. As the highest temperature was set to the buildings and the lowest temperature was to trees, the heat maps of all the days came out with an intermediate colour range of Rainbow Pattern which is nothing but the temperatures of the input wind can be seen in Figure 10. A white arrow of the first image represents the

direction of wind flow. Maximum yellowish colours are depicted throughout the plots which show the slight but huge change in consideration of the microclimate. Dense building structures having less gap in between show the reddish-yellow colour which depicts the higher heat transfer between the buildings and surrounding air. Some blue regions in the temperature contour show the vegetation effect by transferring lower heat to the surroundings.

Figure 10  
Contour plots of temperatures for all the days



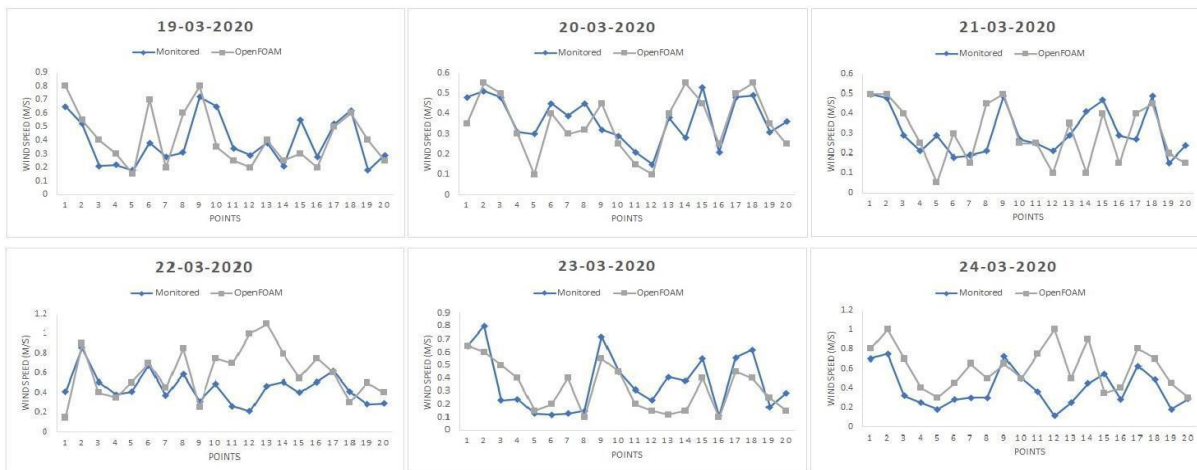
### Discussion

Solver validation with the standard procedure has been performed to check whether the solver chosen for the present study is valid or not. According to the referred literature, it is confirmed that the solver can deal with the airflow with heat transfer conditions. The mesh validation in CFD modelling becomes necessary to perform the quality of the mesh. Because it can affect the solutions and fluid flow patterns of respected studies (Kulkarni et al., 2016). The mesh independence study is confirming the residual plots of needed variables. Residual plots are of some fundamental measure of solutions of convergence. Not convergent means there is some imbalance concerning variables. The residuals do not fall to exactly zero but near to

zero which is the sign of a solution to be more accurate (Mike, 2015).

Velocity and temperature profiles with selected points for all six days are plotted and can be seen in Figure 11 and Figure 12 respectively. The blue lines of graphs of Figure 11 are representing the onsite monitored data while grey lines are used to show the values obtained from OpenFOAM. It is observed from the graph that most of the points' values are strongly matched while few are not. But all the values of OpenFOAM results follow the pattern of monitored results. In the case of the temperature profiles, similar things have happened. The orange lines are used for the OpenFOAM values. Temperature profiles of OpenFOAM results followed the same trend of monitored results. Temperature values of OpenFOAM results are also matched to some extent with monitored values.

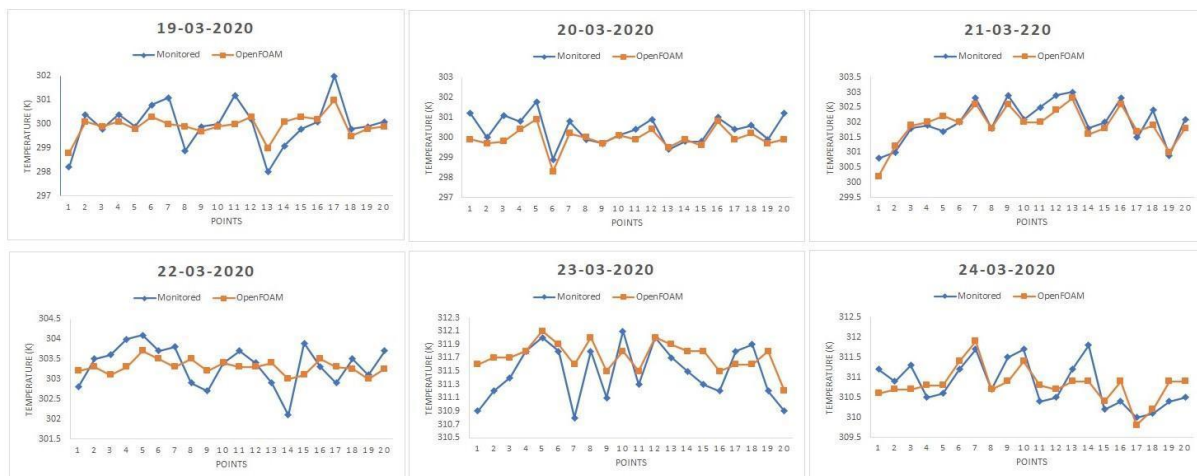
Figure 11  
Velocity profiles with corresponding points for all days



The uncertainty in the measurement of OpenFOAM is found to be in the range of 0.03 to 0.05. However, the uncertainty in this low scale microclimatic study is enough but the biggest thing of this study is that the

OpenFOAM model is showing quite similar results to the actual surrounding environment. This uncertainty in measurement is due to the less mesh refinement of the area near the 3D models of objects.

Figure 12  
Temperature profiles with corresponding points for all days



**Conclusion**

The present study illustrates the change in microclimate due to the warmed building structures in the summertime in Nagpur, a city of India. In particular, how the OpenFOAM can deal with the microclimatic parameters like wind speed and air temperature are presented and discussed briefly. The major aim of this study is to quantitatively compare the CFD models with the actual climatic conditions. This study becomes necessary because it is revealed that the abrupt change in building

structure in summertime hits the surrounding environment (Liu et al., 2019). These sudden temperature changes are mainly responsible for heat cramps, heat exhaustion, heatstroke, and human discomfort (Młynarczyk et al., 2021). The current research explains a unique approach to deal with climatic parameters and to model the air temperature and wind speed over the clusters of buildings. The merit of this study came out with the visualization of vegetation cooling effects on the surrounding environment which makes this study more unique. Several researchers discussed a unique

approach to the evaluation of urban microclimate parameters through Python programming (Bherwani et al., 2021). Few researchers explained the technique of CFD for modelling an airflow over the complex structure but did not succeed to cover the vegetation effects and warmed building structure simultaneously. However, this research is a small attempt of CFD to be introduced in the discipline of microclimate. The present study is carried out in consideration of only a few types of objects (buildings, trees and air). According to this study, it is clear that there is a scope of CFD especially of OpenFOAM in the field of climate change. It becomes possible and important to study with consideration of more objects and parameters like water bodies, humidity, albedo etc. in future.

In the field of research, assessing urban thermal comfort is a difficult task. The results of the present study show that the CFD modelling can assess and predict urban airflow conditions with heat transfer. According to this study, it is concluded that CFD can reliably predict urban microclimate. CFD simulations can therefore be used to detect problem areas and assess the impact of climate adaptation strategies such as green infrastructure and natural ventilation. To increase comfort during the summer, it was planned to lower and homogenize ambient and surface temperatures as much as possible, as well as improve airflow in areas with low wind

speeds. The optimal design of public places, which includes advanced monitoring and modelling techniques as well as effective passive cooling, will help to improve the local urban microclimate significantly. Future research should concentrate on cities with varying climatic conditions to assess the park cooling impact. Later CFD studies on the subject may also include mass transfer in addition to wind flow and heat transfer for a more practical and comprehensive depiction of urban microclimate.

The present study is also able to disclose the ventilation conditions of the well built-up infrastructure and auditoriums. This work is also helpful in the betterment of aerodynamic and good ventilation designs of urban society. It is also seen throughout the study where there is dense vegetation, a sudden temperature drop is observed. The temperature drop by 1°C is considered as enough change to the microclimate. The cooling effect of the trees in the summer season is heavily influenced by weather conditions. It is concluded that trees, as a key component of urban green infrastructure, are extremely effective at regulating urban microclimate and improving thermal comfort on a local level. It is also suggested by this study that if greenery areas are increased in the urban areas, then the problem faced by dwellers can be regulated.

## References

1. Aguerre, H. J., Pairetti, C. I., Venier, C. M., Damián, S. M., & Nigro, N. M. (2018). An oscillation-free flow solver based on flux reconstruction. *Journal of Computational Physics*, 365, 135-148.
2. Allegrini, J., Dorer, V., & Carmeliet, J. (2012). Influence of the urban microclimate in street canyons on the energy demand for space cooling and heating of buildings. *Energy and Buildings*, 55, 823-832.
3. Allegrini, J., Kämpf, J. H., Dorer, V., & Carmeliet, J. (2013). Modelling the urban microclimate and its influence on building energy demands of an urban neighbourhood (No. CONF, pp. 867-872). EPFL Solar Energy and Building Physics Laboratory (LESO-PB).
4. Bherwani, H., Anjum, S., Gupta, A., Singh, A., & Kumar, R. (2021). Establishing influence of morphological aspects on microclimatic conditions through GIS-assisted mathematical modeling and field observations. *Environment, Development and Sustainability*, 1-24.
5. Bherwani, H., Singh, A., & Kumar, R. (2020). Assessment methods of urban microclimate and its parameters: A critical review to take the research from lab to land. *Urban Climate*, 34, 100690.



6. Bhonsle, K. D. (2010). A study of urbanization in Nagpur district. Institute of Town Planners India Journal, 7(3), 88-95.
7. Borges, A. R., & Viegas, D. X. (1988). Shelter effect on a row of coal piles to prevent wind erosion. Journal of Wind Engineering and Industrial Aerodynamics, 29(1-3), 145-154.
8. Bueno, B., Norford, L., Hidalgo, J., & Pigeon, G. (2013). The urban weather generator. Journal of Building Performance Simulation, 6(4), 269-281.
9. Chavan, S., Panwar, V., & Rathod, R. (2015). Review on thermal energy storage techniques. International Journal of Engineering Development and Research, 3(4).
10. Chen, F., Yang, X., & Zhu, W. (2014). WRF simulations of urban heat island under hot-weather synoptic conditions: The case study of Hangzhou City, China. Atmospheric research, 138, 364-377.
11. Costola, D., Blocken, B., & Hensen, J. L. M. (2009). Overview of pressure coefficient data in building energy simulation and airflow network programs. Building and environment, 44(10), 2027-2036.
12. Dhunny, A. Z., Lollchund, M. R., & Rughooputh, S. D. D. V. WIND FLOW ANALYSIS OVER COMPLEX HILLY TERRAINS USING COMPUTATIONAL FLUID DYNAMICS.
13. Diego, I., Pelegry, A., Torno, S., Toraño, J., & Menendez, M. (2009). Simultaneous CFD evaluation of wind flow and dust emission in open storage piles. Applied Mathematical Modelling, 33(7), 3197-3207.
14. elAbbassi, M., Lahaye, D., & Vuik, K. (2019). Modelling Turbulent Combustion Coupled with Conjugate Heat Transfer in OpenFOAM. In ENUMATH (pp. 1137-1145).
15. Gagliano, A., Nocera, F., & Aneli, S. (2017). Computational fluid dynamics analysis for evaluating the urban heat island effects. Energy Procedia, 134, 508-517.
16. Ghiaus, C., Allard, F., Santamouris, M., Georgakis, C., & Nicol, F. (2006). Urban environment influence on natural ventilation potential. Building and environment, 41(4), 395-406.
17. Howard, L. (1818). The climate of London: deduced from meteorological observations, made at different places in the neighbourhood of the metropolis (Vol. 1). W. Phillips, George Yard, Lombard Street, sold also by J. and A. Arch, Cornhill; Baldwin, Cradock, and Joy, and W. Bent, Paternoster Row; and J. Hatchard, Picadilly.
18. Veena, KM Parammasivam and T N Venkatesh. Numerical simulation of wind flow and heat transfer over a cluster of buildings.
19. Kolokotroni, M., Giannitsaris, I., & Watkins, R. (2006). The effect of the London urban heat island on building summer cooling demand and night ventilation strategies. Solar Energy, 80(4), 383-392.
20. Kulkarni, S. S., Chapman, C., & Shah, H. (2016). Computational fluid dynamics (CFD) mesh independency study of A straight blade horizontal Axis tidal turbine.
21. Kuron, M. (3). Criteria for Assessing CFD Convergence 2015. Diponívelem: <[http://www. engineering. com/DesignSoftware/DesignSoftwareArticles/ArticleID/9](http://www.engineering.com/DesignSoftware/DesignSoftwareArticles/ArticleID/9), 296.
22. Liu, J., Heidarinejad, M., Nikkho, S. K., Mattise, N. W., & Srebric, J. (2019). Quantifying Impacts of Urban Microclimate on a Building Energy Consumption—A Case Study. Sustainability, 11(18), 4921.
23. Mackey, C., Galanos, T., Norford, L., Roudsari, M. S., & Architects, P. (2017, August). Wind, sun, surface temperature, and heat island: critical variables for high-resolution outdoor thermal comfort. In Proceedings of the 15th international conference of building performance simulation association. San Francisco, USA.
24. Młynarczyk, M., Bogdan, A., & Jankowski, T. (2021). The influence of local temperature and air velocity changes on the thermal sensations of users' working in surgical clothing. Indoor and Built Environment, 1420326X21990815.

25. Moukalled, F., Mangani, L., & Darwish, M. (2016). The finite volume method in computational fluid dynamics (Vol. 113, pp. 10-1007). Berlin, Germany:: Springer.
26. Murakami, S. (1998). Overview of turbulence models applied in CWE–1997. *Journal of Wind Engineering and Industrial Aerodynamics*, 74, 1-24.
27. Nair, M., Bherwani, H., Kumar, S., Gulia, S., Goyal, S., & Kumar, R. (2020). Assessment of contribution of agricultural residue burning on air quality of Delhi using remote sensing and modelling tools. *Atmospheric Environment*, 230, 117504.
28. Reiter, S. (2008). Validation process for CFD simulations of wind around buildings. In *Proceedings of the European Built Environment CAE Conference* (p. 18). Londres.
29. Santamouris, M., Papanikolaou, N., Livada, I., Koronakis, I., Georgakis, C., Argiriou, A., & Assimakopoulos, D. N. (2001). On the impact of urban climate on the energy consumption of buildings. *Solar energy*, 70(3), 201-216.
30. Smitham, J. B., & Nicol, S. K. (1991). Physico-chemical principles controlling the emission of dust from coal stockpiles. *Powder technology*, 64(3), 259-270.
31. Stathopoulos, T., & Wu, H. (2004). Using computational fluid dynamics (CFD) for pedestrian winds. In *Structures 2004: Building on the Past, Securing the Future* (pp. 1-9).
32. Taha, H. (2017). Characterization of urban heat and exacerbation: Development of a heat island index for California. *Climate*, 5(3), 59.
33. United Nations, Department of Economic and Social Affairs, Population Division. (2015). *World population prospects: The 2015 revision. Key Findings and Advance Tables*.
34. Usamentiaga, R., Venegas, P., Guerediaga, J., Vega, L., Molleda, J., & Bulnes, F. G. (2014). Infrared thermography for temperature measurement and non-destructive testing. *Sensors*, 14(7), 12305-12348.
35. Veena, K., Asha, V., Shameem, C. A., & Venkatesh, T. N. (2016). Simulations of flow past multiple high-rise buildings using OpenFOAM. In *18th AeSI CFD Symposium*.
36. Veena, K., Parammasivam, K. M., & Venkatesh, T. N. (2020). Urban Heat Island studies: Current status in India and a comparison with the International studies. *Journal of Earth System Science*, 129(1), 1-15.
37. Veena, K., KM Parammasivam and T N Venkatesh. Numerical simulation of wind flow and heat transfer over a cluster of buildings.
38. Veena, K., Parammasivam, K. M., & Venkatesh, T. N. Estimation of turbulent heat transfer rates for flow over buildings using OpenFOAM.
39. Verma, S. K. (2009). *Wind Effects on Structurally Coupled Tall Buildings* (Doctoral dissertation, Ph. D Thesis, Indian Institute of Technology, Roorkee).
40. Wiren, B. G. (1977). *A WIND TUNNEL STUDY OF WIND VELOCITIES IN PASSAGES BETWEEN AND THROUGH BUILDINGS*.
41. Yoon, J. Y., & Patel, V. C. (1996). Numerical model of turbulent flow over sand dune. *Journal of Hydraulic Engineering*, 122(1), 10-18.

**ANALYSIS AND DESIGN OF BOX CULVERT BY IRC LOADING****K. Thakare<sup>1</sup>, P. Bhandari<sup>2</sup> and K. Tajne Asutkar<sup>3</sup>**<sup>1,2</sup>Department of Civil Engineering, PCE, Nagpur<sup>3</sup>Department of Civil Engineering, GCE, Nagpur**ABSTRACT**

Culvert is a hydraulic structure that allows water to flow under a road, railroad, trail, or similar obstruction from one side to the other side. Culverts can be constructed of a variety of materials including cast-in-place or precast concrete. A culvert may be a bridge-like structure designed to allow vehicle or pedestrian traffic to cross over the waterway while allowing adequate passage for the water. Culverts come in many sizes and shapes including round, elliptical, and box-like constructions. In this work, the study of Box culvert (1m x 5m x 4m) is analyzed for IRC Class A-1 Lane + Class 70R loading and Class A-3 Lanes. conclusions made based on bending moments and shear forces.

**Keywords** – Box culvert, Loading class, Moment calculations, Reinforcement, Sidewalls, Topslab, Bottom slab.

**1. Introduction**

Box culverts are low rise bridge or structure which is used to drain water in crossing of railway, flyover, roads, etc. Culverts are always economical than bridges where the discharge in the opening depends on the number of cells which is generally used where the roadway crosses the high embankment. Box culverts are generally cast in situ in India, but in other countries, the box culverts are preferred due to their low cost and economically with having fast workmanship. The box act as a minor bridge when the number of cells increases and spans greater than 6m in length. Its height depends on the span. Box culverts are used to discharge all water coming from irrigation, surface water, river, and canals. They also control all the stormwater and floodwater during the rainy season. Box culverts that have four corners are monolithically jointed. In other cases the box will be of three sides means which has a

bottom slab (Raft) and vertical walls. The top slab is made up by a precast slab which is available in the market but we cannot joint it monolithically. Cushioning is very important in every box culvert which is decided by road profile and bearing capacity of soil available at the site.

**2. Types of box culverts****According to the Classification by Materials**

- 2.1.1) Concrete                      2.1.2) Steel  
2.1.3) Aluminum

**According to the Classification by Shape**

- Box culvert    2.2.2) Pipe culvert    2.2.3) Pipe  
arch culvert    2.2.4) Bridge culvert  
2.2.5) Arch culvert

**According to the Classification by Loading as per IRC**

- IRC-CLASS-70 R    2.3.2) IRC-CLASS-A  
2.3.3) IRC-CLASS-B

**3. Preliminary Data****General Arrangement of Box Culvert**

Clear span	= 4.00 m
Clear height	= 5.00 m
No. Of span	= 2
	= 0.50 m
Bottom slab thickness	= 0.50 m
Side wall thickness	= 0.50 m
Middle wall thickness	= 0.25 m
Dimension of haunch	= 0.30 m x 0.30 m
Height of cushion on top	= 0.00 m

Thickness of wearing coat=0.065 m  
 Width of structure = 14.00 m  
 Width of carriageway = 12.00 m  
 Width of crash barrier = 0.50 m  
 Effective span of box = 4.50 m  
 Effective height of box = 5.50 m

**Material Density and Safe Bearing Capacity of Soil**

Unit weight of concrete = 25 kN/m<sup>3</sup>  
 Unit weight of earth = 20 kN/m<sup>3</sup>  
 Unit weight of wearing coat = 22 kN/m<sup>3</sup>  
 Safe bearing Capacity of Soil = 150 kN/m<sup>2</sup>

**Grade of Materials**

Concrete grade = M30  
 Steel grade = Fe500

**3.4 Modulus of Sub-grade Reaction**

From Equation 9-9, on page no. 503 of Joseph E. Bowles book

Where, SF = Factor of safety = 2.5  
 qo = Safe bearing capacity of soil = 150 kN/m<sup>2</sup>

Ks = 40 x 2.5 x 150 = 15000 kN/m<sup>3</sup>  
 Adopt a value of say 15000 kN/m<sup>3</sup> on a conservative side.

- 1) Bottom slab divided into Parts = 10.0
- 2) Spacing of springs m = 0.45
- 3) Size of element (1 x 0.450) = 0.45m<sup>2</sup>
- 4) Value of spring constant = 15000 / 0.45 = 33750 kN/m
- 5) Area of support corner spring (Type 1) = 0.225 m<sup>2</sup>
- 6) Area of all intermediate springs (Type 2) = 0.45 m<sup>2</sup>
- 7) Modulus of Subgrade reaction = 15000 kN/m<sup>3</sup>
- 8) Spring stiffness at end support = 3375 kN/m
- Spring stiffness at Intermediate supports = 6750 kN/m

**4. Methodology and problem solving approach steps**

**Design steps [6]**

Silent features

- Load calculations 1.2.1) Top slab 1.2.2) Bottom slab 4.2.3) Total load

- Moment calculations 1.3.1) Top slab 1.3.2) Bottom slab 1.3.3) Side walls
- Distribution factors
- Moment distribution 1.5.1) Fixed end moment due to dead load 1.5.2) Fixed end moment due to live load 1.5.3) Fixed end moment due to total load
- Design of section 1.6.1) Top slab 1.6.2) Bottom slab 1.6.3) Side walls

**4.2. Design Constant**

Grade of steel, fyk = 50 N/mm<sup>2</sup>  
 Design tensile reinforcement of steel, fyd = 435 N/mm<sup>2</sup>  
 Grade of concrete, fck = 30 N/mm<sup>2</sup>  
 Partial safety for concrete, Ym = 1.5 (for basic & seismic combination)  
 1.2 (for accidental combination)  
 Factor, α = 0.67 .... As per IRC 112-2011, clause 6.4.2.8  
 Design compressive strength of concrete, fcd = αfck/Ym = 13.40 N/mm<sup>2</sup>  
 Mean axial tensile strength of concrete, fctm = 2.5 N/mm<sup>2</sup> .... As per IRC 112-2011, Annexure A2, eq. A2-2  
 Elastic modulus of concrete, Ecm = 31000 N/mm<sup>2</sup> .... As per IRC 78-2014, cl 706.3.1.1  
 Elastic modulus of steel, Es = 200000 N/mm<sup>2</sup>  
 Ultimate compressive strain in concrete, εu3 = 0.0035 .... As per IRC 112-2011, table 6.5  
 Ultimate compressive strain in concrete, εst (IRC 112.2011, clause 6.2.2)  
 Limiting neutral axis depth ratio, xu,max / d = 0.62 ... xu,max / d = εcu3 / (εcu3 + εst)  
 Factor, η = 1 .... As per IRC 112-2011, clause A2.9  
 Factor, λ = 0.8 .... As per IRC 112-2011, clause A2.9  
 ηfcd = 13.40 N/mm<sup>2</sup>  
 Lever arm of internal forces, z = (1 - λx/2)d = 0.75d  
 Compressive strength of c/s, Fc = 4.98 N/mm<sup>2</sup>  
 = 15000 kN/m<sup>3</sup>  
 = 3375 kN/m  
 Where, Fc = λx\*ηfcd\*(1-λx/2)Ru  
 lim = 0.36\*fck\*(xu/d)\*(1-0.416Xu/d)bd<sup>2</sup> = 3.29 bd<sup>2</sup> N/mm<sup>2</sup>

**4.3 Clear cover to reinforcement**

- For top Slab = 40 mm
- For Base Slab = 75 mm
- For Side Wall Earth Face = 75 mm
- Inner Face = 50 mm
- For middle wall = 50 mm

5. Figures and Tables

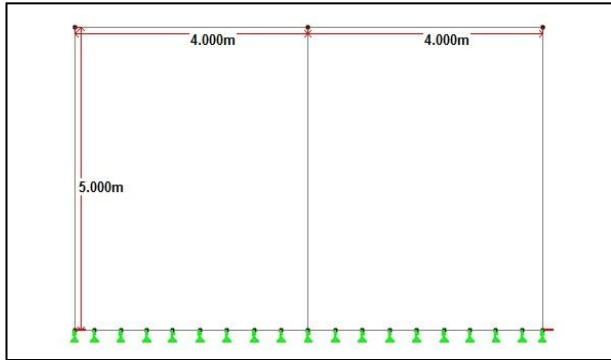


Fig1. Drawing of Box Culvert

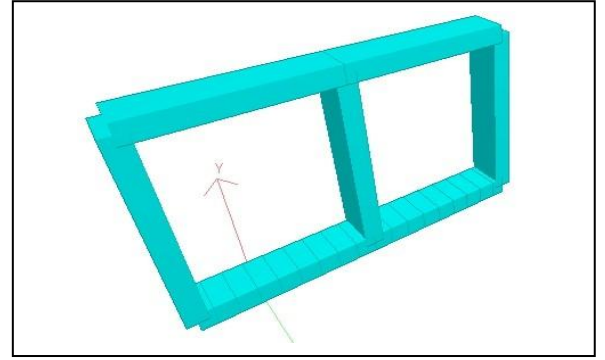


Fig2. Box Culvert 3D view

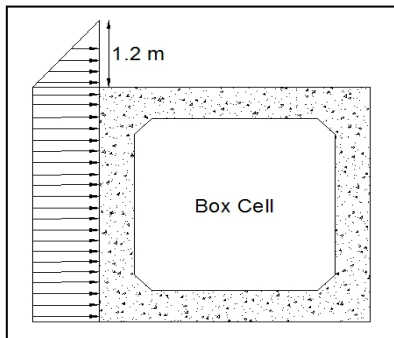


Fig. 3 Live load Surcharge at one side

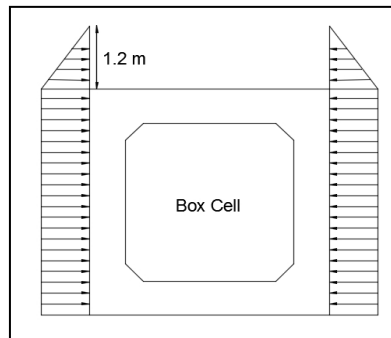


Fig.4 Live load Surcharge at both side

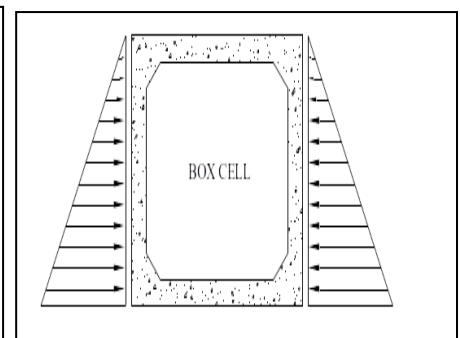


Fig.5 Earth Pressure at side wall in saturated condition

6. Result and Discussions

Class of Vehicle		Max. Dispersed load at MidSpan (Kn/m <sup>2</sup> )	Max. Dispersed load at Support (Kn/m <sup>2</sup> )
Case 1 :	IRC Class A-1 Lane +Class 70R - wheeled vehicle	34.512	65.495
Case 2 :	IRC Class A-3 Lanes	22.880	43.663

Table 1. Values of Total Load (Impact Load + Breaking Load)

Particulars	Bending moment (kN-m)
1) Top Slab Mid Span	243.82
2) Top Slab Supports	138.53
3) Side Wall Mid Span	125.65
4) Side Wall Supports	287.62
5) Bottom Slab Mid Span	282.65
6) Bottom Slab Supports	324.25

Table 2. Values of Bending Moment due to Class A-1 Lane + Class 70R loading

Particulars	Shear Force (kN)
1) Top Slab	382.56
2) Side Wall	142.86
3) Bottom Raft	395.68

Table 3. Values of Shear Force due to Class A-1 Lane + Class 70R loading

Particulars	Area of steel provided (mm <sup>2</sup> )
1) Top Slab Mid Span	2262
2) Top Slab Supports	2618
3) Side Wall Mid Span	1131
4) Side Wall Supports	2618
5) Bottom Slab Mid Span	2618
6) Bottom Slab Supports	2618

**Table 4. Values of Steel Provided for Class A-1 Lane + Class 70R loading**

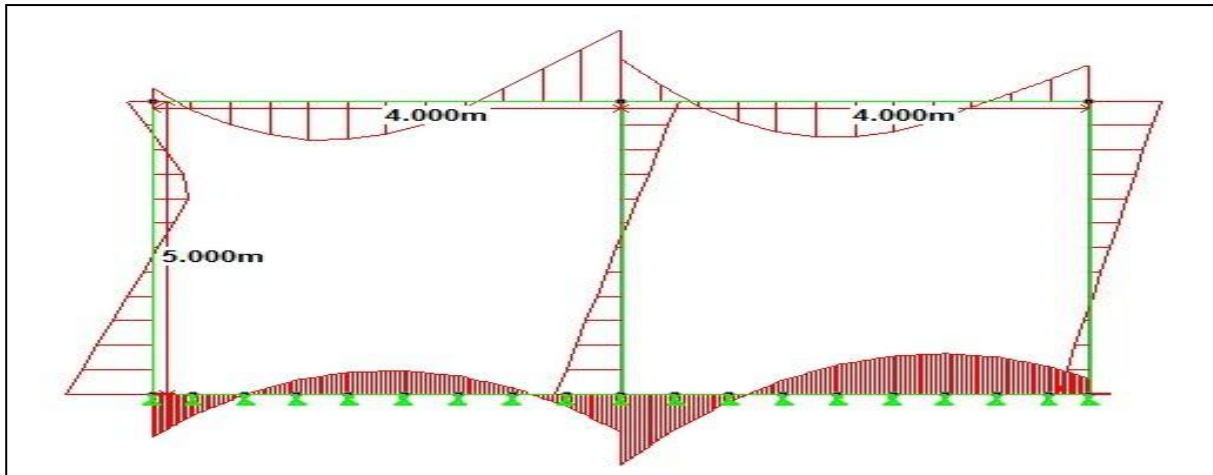


**Fig 6. Bending Moment on Box Culvert due to Class A-1 Lane + Class 70R loading**

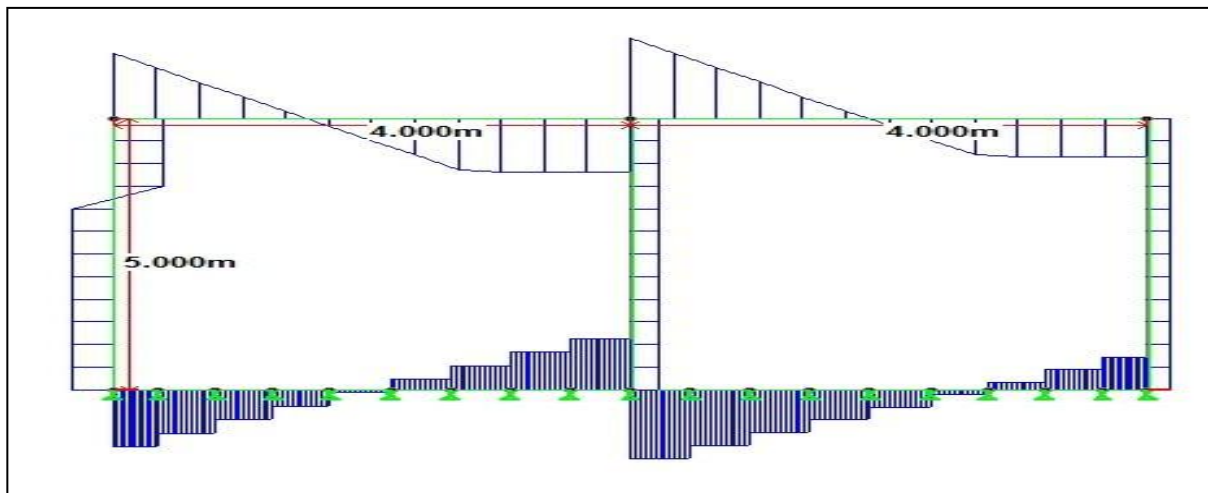


**Fig 7. Shear Force on Box Culvert due to Class A-1 Lane + Class 70R loading**

**7. Conclusion**

In view of achieving the aim and objectives of this project the detailed design of Box Culvert (1m x 5m x 4m) is carried out in excel sheets and the comparative statement is given as per the results obtained.

- Box Culvert is found to be good for large

- span.
- Bending moment are found more at mid span of the top and bottom slab.
- Bending moment is found more at Support of Side wall.
- Shear force results are more at top slab and bottom raft of Box Culvert.

### References

1. A. D. Patil, A.A. Galatage (2016) , " Analysis of box culvert under cushion loading ", International advanced research journal in science, engineering &technology, 03(03): 163-166.
2. Sujata Shreedhar, R. Shreedhar (2013)," Design coefficients for single and two cell box culvert" International journal of civil & structural engineering, 03(03):475-494.
3. Mahesh D. Kakade, Rajkuwar A. Dubai (2017), " A study of behavior of R.C.C. box culvert under the influence of static & dynamic loads in accordance with IRC " International researchjournal of engineering and technology , 04(10): 30-35.
4. M. Bilal khan, M. Parvez alam (2015)," Hydraulic design of box culvert for highway at coastal region" International journal of advanced in engineering research,09(02): 31-40.
5. Ketan Kishor Sahu, Shraddha Sharma (2015), "Comparison & study of different aspect of box culvert" International journal of scientific research &development,03(07):167-175.
6. Roshan Patel, Sagar Jamle (2019),"Analysis and Design of Box Culvert: A Manual Approach"International Journal of Advanced Engineering Research and Science, 6(3): 286-291.
7. IRC 6 (2016), "Standard specification and code of practice for road bridge section : II loadsand stresses"
8. IRC 112 (2011), "Code of practice for concrete road bridges"
- IRC 78 (2014), "Standard specification and code of practice for road bridges"

## SIMULATION REALIZATION BY PYTHON FOR PV ARRAY INTERFACING THREE PHASE AC GRID

P.Kale<sup>1</sup>, H.Patil<sup>2</sup> and M. M. Renge<sup>3</sup>

Shri Ramdeobaba College of Engineering and Management, Nagpur

<sup>1</sup>kalepa@rknec.edu, <sup>2</sup>patilhr@rknec.edu, <sup>3</sup>rengemm@rknec.edu

### ABSTRACT

As we know due to the expanding interest for petroleum products and natural components thought about, we are very nearly confronting energy emergency in not-so-distant future. In this manner, sustainable power regularly named as spotless energy comes from normal sources which are scant in nature and additionally advance from measures that are continually recharged. Sun oriented energy is one approach to connect energy hole. Therefore, power electronic interface for grid connected PV system has been proposed using Force Commuted Converter. In this Paper, different operating modes of a forced commuted converter are been designed and developed using python programming language so that to present result in different point of view to get new things and implement it. Here, the system monitors average voltage value with the help of slider position. Further different perspectives are carried out that will display the MPP which reflects its result on Arduino port (serial communication) with personal computer (python programming).

**Keywords:** AC Grid, Force Commutated Converter, Photovoltaic (PV) Array, Python Programming Language, Serial Communication.

### 1. Introduction

With the expanding need for current appliances and an extravagant way of life of individuals, the demand for power has expanded. This has likewise been an extraordinary issue in the general public. The arrangement of expanding quanta of energy is an imperative pre-essential for the financial development of a country[2]. As we realize that India is on one of the top chiefs on the planet's most alluring sustainable power markets. Power creation from photovoltaic frameworks has gotten not so much expensive but rather more productive as of late. The improvement in sustainable power sources replaces the other conventional fuel sources. Among the environmentally friendly power sources, sunlight-based energy assumes a significant part because of its contamination free nature, no expense of energy, long lifetime, no pivoting parts. For prudent reasons the sun powered energy isn't straightforwardly interfaced with the utility network[1]. Subsequently a power electronic interface for grid connected PV system has been proposed using Force Commuted Converter.

Therefore, as infiltration of photovoltaic (PV) produced electrical energy into the grid system is expanding broadly. A force commutated converter is the innovation that empowers proficient and adaptable interconnection of dc

connection and ac network[3]. The integrity of two sources powers to remember a few boundaries like Force quality, which includes recurrence, power, voltage, and so on of the two sources. To keep a synchronism of the two sources and give a superior quality yield at the consumer end[4]. The solar PV array used in this system has a MPPT method carried out with it to catch most extreme measure of power while using limited sources[5]. The technique empowers quick prototyping of control system and force converters parts by real time simulation of the system. As we know that observing is essential to keep a system's supported operability and comprehend the issues that happen during PV system operation. Data on PV attributes and meteorological information is fundamental to guarantee the performance of PV system[6]. Further, the work has focused on how to get maximum power point from python-based program by controlling slider moment and to get communicate with Arduino to get those points.

### 2. Proposed Scheme

System configuration of the proposed grid-connected photovoltaic (PV) array using FCC is shown in Fig. 1. A basic plan utilizing FCC for interfacing solar PV array with AC three phase utility grid.



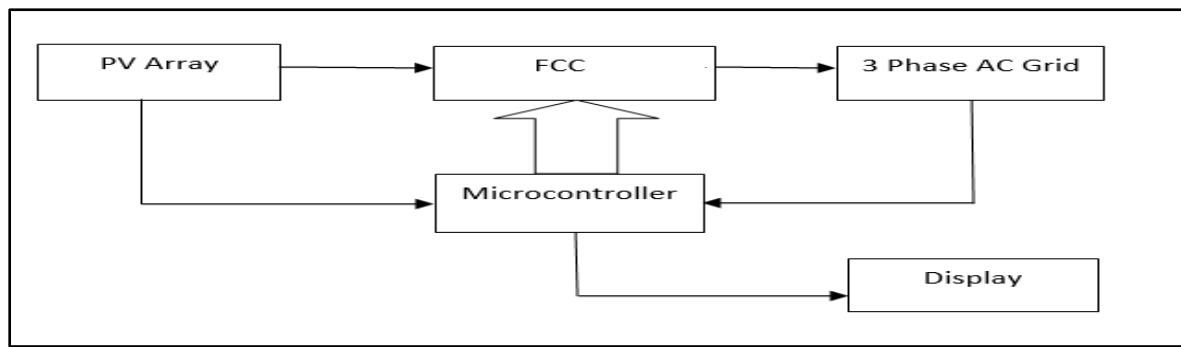


**Fig.1: Block diagram of proposed scheme**

Here in the proposed scheme, from the computer python-based waveform through USB signal is given to microcontroller to generate a firing angle and further leads to operate the converter. That is microcontroller output in the form of pulses is given to converter here Converter gets three phase input supply and at output side PV panel is connected. Further two inputs are given to microcontroller that is from three phase sensor input in order to detect ZCD to measure a firing angle and one from PV panel i.e., control signal in order to sense voltage and current.

**2.1 Converter**

Converters are the devices which changes over the DC supply voltage into Rotating voltage supply and AC voltage into DC supply voltage. The yield voltage is controlled with the control of switches opening and shutting time terms. For consistent brace tied PV interconnections, a typical solar PV should provide two-way flows of power and communication between the solar PV system and the smart grid. The conventional line commutated converters consume high reactive power from the system i.e., where high capacity and efficiency are needed. In order to turning on and natural commutation Such converters use switching devices (SCR). Significant drawback is that it

delivers a square wave current yield rich with harmonics which further can be diminished by the utilization of filters, if not proper voltage than switching problem may occur and if the current goes below the latching current than commutation failure takes place. To overcome this, reverse voltage is applied forcefully i.e., forced commutated inverters were suggested. In this circuit based on output voltage Vdc and firing angle  $\alpha$  different converter modes are shown based on python-based programming. When firing angle ( $\alpha$ ) is somewhere in the range of  $0^\circ$  and  $90^\circ$ , the converter is said to be in rectification mode and when  $\alpha$  is somewhere in range of  $90^\circ$  and  $180^\circ$ , it is said to be in inversion mode (reversal mode).

Libraries used for simulation of converter waveform using python-based programming language is as MATPLOTLIB, NUMPY, etc.

**2.2 Simulation of converter waveform using PYTHON are as follows**

Output waveform of single-phase full wave converter for resistive load at  $\alpha = 30^\circ$  is shown in Fig.2 here point on waveform is traced with the help of a slider. Similarly Output waveform of single-phase full wave converter for highly Inductive load at  $\alpha = 30^\circ$  is shown in Fig.3 using python-based programming.

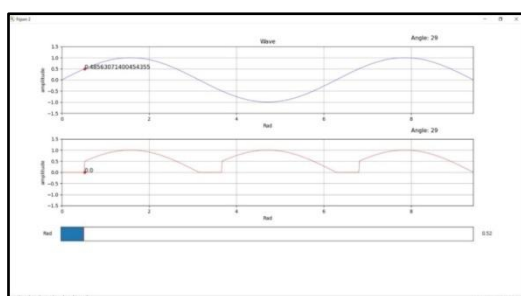


**Fig.2:  $\alpha = 30^\circ$  for resistive load**

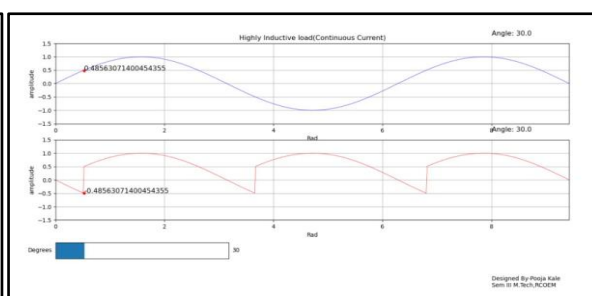


**Fig.3:  $\alpha = 30^\circ$  for highly inductive load**

Output waveforms of the converter operation in different mode is depicted below in Fig.4

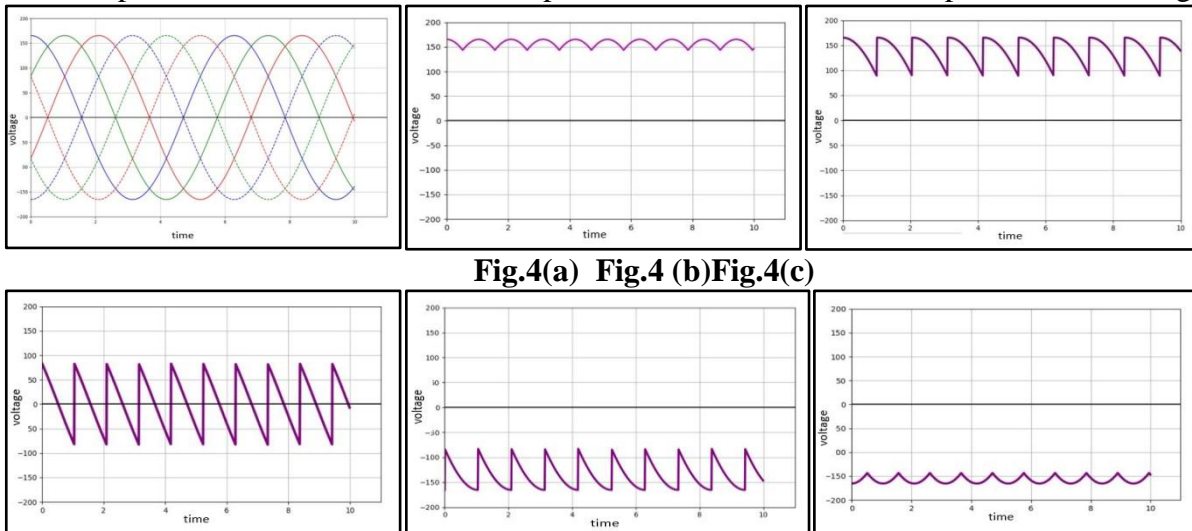


Fig.4(a) Fig.4 (b)Fig.4(c)

Fig.4(d)Fig.4(e) Fig.4(f)

Fig.4 :(a) Output waveform of three phase full wave converter, (b)for  $\alpha = 0^\circ$ , (c)  $\alpha = 0^\circ - 90^\circ$ , (d)  $\alpha = 90^\circ$ , (e)  $\alpha = 90^\circ - 180^\circ$  and (f)  $\alpha = 180^\circ$  using python-based programming.

### 2.3 Photovoltaic Arrays

Photovoltaic cell is an essential unit of sunlight-based board i.e., solar panel. This device is used to convert light energy into electrical structure. Electrical energy is made in type of DC supply. Depending upon the requirement of load the photovoltaic cells may be connected in series or parallel combinations. That is based on power interest, the quantity of PV boards needed in series and in parallel are figured. Parallel cells bring about addition of currents

while keeping voltage steady though the series combination adds the voltage magnitude. Most residential solar panels have the power output ratings from 250 to 400 watts, depending on panel size and how well they convert sunlight into energy. In the proposed scheme python-

based programming is carried out for 1000 W/m<sup>2</sup> constant irradiance. Programming has been carried out to get the I-V characteristics of the solar photovoltaic module. The model (Waaree Energies WU-240) is selected to generate I-V characteristic of solar photovoltaic module. Model's aim is to accomplish an I-V curve like the graph that presents the makers datasheet of solar panel in which  $V_{mp}$  is at 36.5 V and  $I_{mp}$  is at 8.25 A. PV plot i.e., power curve below is a result of point-to-point multiplication of current and voltages for all voltages from SC to OC conditions considering a fixed radiation level. Here slider plays an important role to trace plot from point to point by changing its position which further display its correspondence value as shown in Fig.6

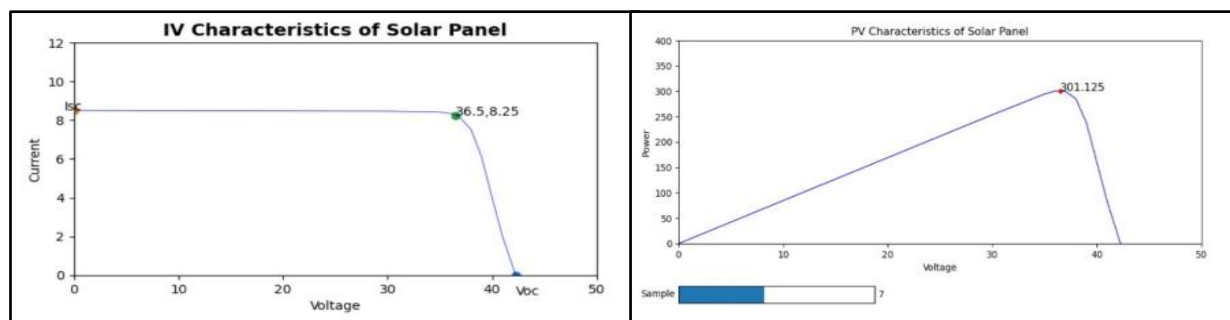


Fig.5: I-V plot Fig.6: P-V plot

In the proposed scheme, the converter is worked as an inverter. From Fig.7 observing P-

V and I-V plot it is observed that maximum output voltage that is 36.5 V according to the

characteristics of solar panel, it is multiplied by number of series panels required in order to get  $V_{avg}$  average voltage, here horizontal line indicates  $V_{avg}$ , Therefore, at  $\alpha = 135^\circ$  in inversion mode value of  $V_{avg}$  is -116 V and from the I-V characteristics as maximum voltage at 36.5 V and required  $V_{avg}$  for

converter in inversion mode to operate 116 volt, therefore P-V panel voltage  $V_{pv}$  given to converter as  $36.5 \times 3.17 = 115.70$  i.e. negative voltage is applied forcefully, were approx. 3 panels are required in series to get average voltage value required for converter.

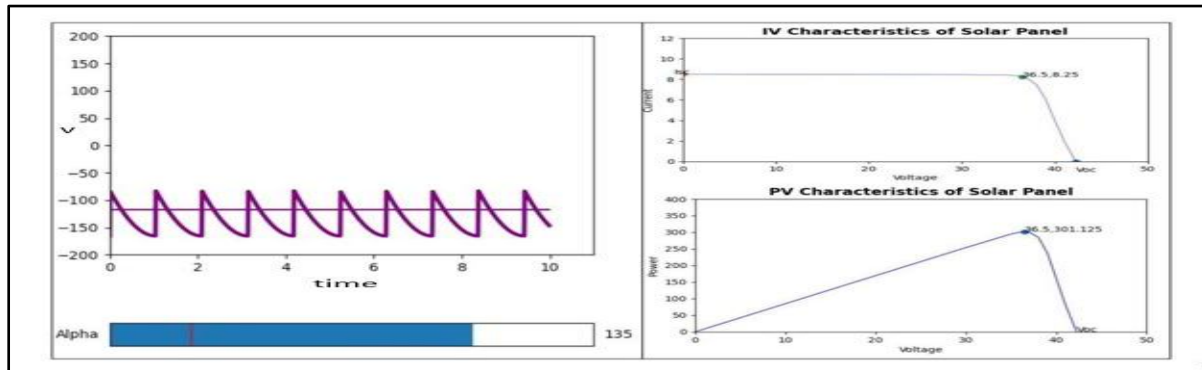


**Fig.7: Converter in inversion mode at  $\alpha 135^\circ$ , according to the solar panel characteristics here  $V_{pv}$  voltage injected to converter side is decided by adding no. of appropriate panel in series**

### 2.3 Advantages and Disadvantages of simulation realization using python rather than using other language

#### Advantages:

1. Matplotlib provide high quality graph if we use python, we can use Matplotlib
2. Python is easy to use, and it has large number of that we can use according to requirement.
3. Using python help us to use many in built function rather than using third party functions.
4. The main advantage of using python is easy connection (pyserial) between PC to Arduino.

#### Disadvantages:

1. Python main issue is it gives us runtime error.
2. Its speed is less as compared to other programming language such as C.

### 2.4 Monitoring the plot and exchanging the data from personal computer (pc) to Arduino by different ways.

**Serial Communication** - Whenever we would move slider as shown Fig.6 first it would create one text file if it's not created previously. And it would append the plots in the file. Afterwards as soon as we close the graph window the serial communication would take place. For that we have used pyserial library for the communication between pc to Arduino using COM ports. In python we have to specify the COM port number where Arduino is connected in order to communicate which means need to mention same COM port in pc as well as Arduino and baud rate should be also same in order to exchange data. After closing the graph, it would read the text file data and establish serial communication with Arduino and start sending the value one by one in the Arduino which was stored on the text file. In this case we have use (write) in order to write data from pc to Arduino and in Arduino side we have used readString in order to read the data and display it on Arduino port.

```

pooja@pooja: ~/Desktop/PROJECT
here is the data b'Date&Time 2021-05-08 17:56:36.527401,x axis:10,y axis:84.8
\n'
Date&Time 2021-05-08 17:56:37.258836,x axis:20,y axis:169.4
\n'
here is the data b'Date&Time 2021-05-08 17:56:37.258836,x axis:20,y axis:169.4
\n'
Date&Time 2021-05-08 17:56:38.337142,x axis:30,y axis:253.8
\n'
here is the data b'Date&Time 2021-05-08 17:56:38.337142,x axis:30,y axis:253.8
\n'
Date&Time 2021-05-08 17:56:39.058809,x axis:35,y axis:294.7
\n'
here is the data b'Date&Time 2021-05-08 17:56:39.058809,x axis:35,y axis:294.7
\n'
Date&Time 2021-05-08 17:56:40.573321,x axis:35.5,y axis:297.49
\n'
here is the data b'Date&Time 2021-05-08 17:56:40.573321,x axis:35.5,y axis:297.49
\n'
Date&Time 2021-05-08 17:56:42.846612,x axis:36,y axis:300.6
\n'
here is the data b'Date&Time 2021-05-08 17:56:42.846612,x axis:36,y axis:300.6
\n'

```

Fig.8: p-v plot values on python console

```

/dev/ttyUSB0
Date&Time 2021-05-08 17:56:36.527401,x axis:10,y axis:84.8
Date&Time 2021-05-08 17:56:37.258836,x axis:20,y axis:169.4
Date&Time 2021-05-08 17:56:38.337142,x axis:30,y axis:253.8
Date&Time 2021-05-08 17:56:39.058809,x axis:35,y axis:294.7
Date&Time 2021-05-08 17:56:40.573321,x axis:35.5,y axis:297.49
Date&Time 2021-05-08 17:56:42.846612,x axis:36,y axis:300.6

```

Fig.9: Data on Arduino port

Also, we can achieve this thing by using two more methods:

### 2.4.1 SD card module

In order to exchange the data from pc to Arduino we would need a SD card module hardware and we need to do communication of SD card module with Arduino. After doing connection we need to transfer file from pc to

Arduino. And we need to write a method in order to send the data as well as on the other end we need to write the method to read the data. But every time we need transfer updated file in SD card before running the code in order to get the latest reading. Fig.11 shows the Output on COM3 in Arduino by interfacing SD Card Module with Arduino.

```

demo - Notepad
File Edit Format View Help
2021-04-09 16:54:30.557051,x axis:10,y axis:84.8
2021-04-09 16:54:30.685073,x axis:35.5,y axis:297.49
2021-04-09 16:54:30.817915,x axis:36.5,y axis:301.125
2021-04-09 16:54:30.934236,x axis:37,y axis:299.7
2021-04-09 16:54:31.068322,x axis:37.5,y axis:292.5
2021-04-09 16:54:31.267534,x axis:38,y axis:285
2021-04-14 16:39:59.045856,x axis:10,y axis:84.8
2021-04-14 16:39:59.432110,x axis:20,y axis:169.4
2021-04-14 16:39:59.574475,x axis:30,y axis:253.8
2021-04-14 16:40:00.224794,x axis:35,y axis:294.7
2021-04-14 16:40:00.900725,x axis:35.5,y axis:297.49
2021-04-14 16:40:01.504235,x axis:36,y axis:300.6

```

Fig.10: Text file created in pc

```

COM3
Initializing SD card...card initialized.
2021-04-09 16:54:30.557051,x axis:10,y axis:84.8
2021-04-09 16:54:30.685073,x axis:35.5,y axis:297.49
2021-04-09 16:54:30.817915,x axis:36.5,y axis:301.125
2021-04-09 16:54:30.934236,x axis:37,y axis:299.7
2021-04-09 16:54:31.068322,x axis:37.5,y axis:292.5
2021-04-09 16:54:31.267534,x axis:38,y axis:285
2021-04-14 16:39:59.045856,x axis:10,y axis:84.8
2021-04-14 16:39:59.432110,x axis:20,y axis:169.4
2021-04-14 16:39:59.574475,x axis:30,y axis:253.8
2021-04-14 16:40:00.224794,x axis:35,y axis:294.7
2021-04-14 16:40:00.900725,x axis:35.5,y axis:297.49
2021-04-14 16:40:01.504235,x axis:36,y axis:300.6

```

Fig.11: Output on COM3 in Arduino

### 2.4.2 Ethernet Module

In this case with help of ethernet module on Arduino we can transfer the data from pc to Arduino with the help of internet. We need to connect both pc and Arduino on same network in order to communicate. But advantage of using serial communication is that we can transfer data in real time without using any extra hardware. It reduces the cost and efforts. And user can easily use application in pc(python) and in Arduino (C)

### 3. Discussion

Outline of the PV array monitoring system: The PV monitoring system was design using ATmega328P microcontroller. Where, it is to save graph plots in file and send it to the Arduino using serial communication. The computer is used to present data and control the monitoring system operations. Thus, ability to trace P-V curve is one of its novelty. This allows to measure PV panel characteristics directly from the python-based programming language. Monitoring the plot and exchanging the data from pc to Arduino by different ways

#### 4. Conclusion

In this paper, a simple power electronic interface based on the FCC for utility grid-connected PV array was proposed. Different operating modes of converter is discussed based on firing angle alpha by using python-based programming language, out of which in this scheme converter operate in inverter mode. The purpose of this project is to trace the

highest P-V point from the graph to pc in the text file with the movement of slider and send the P-V points to the Arduino. Based on the analysis and research, it can be concluded that there are multiple ways that can be used in order to exchange the data (P-V points) between pc to Arduino. But by using serial communication we can do it in a cheaper way as well as it is too easy to use.

#### References

1. J. M. Kumbhare, M. M. Renge. (2014). Line commutated Converter for grid interfacing of solar photovoltaic array. IEEE International Conference on Power Electronics, Drives and Energy.
2. Bimal K. Bose. (2000). Energy, Environment, and Advances in Power Electronics. IEEE Trans. on Power Electronics, Vol. 15, pp. 688- 701.
3. Murat Unlu, Sabri Camur, Ersoy Bser. (Number 2, 2015). A Current-Forced Line-Commutated Inverter for Single-Phase Grid-Connected Photovoltaic Generation Systems. Volume 15.
4. Ignatova, V., Villard D., Hypolite J., M (2015). Simple indicators for an effective Power Quality monitoring and analysis. IEEE 15th International Conference on Environment and Electrical Engineering (EEEIC), doi:10.1109/eeeic.2015.7165321.
5. Elzein, I. A., Petrenko, Y., Kurdi, M (2018). Improving the Accuracy and Response Time of P&O in Detecting the Maximum Power Point for a Photovoltaic System Environment, 8<sup>th</sup> International Conference on Power and Energy Systems (ICPES) doi:10.1109/icpesys.2018.8626952.
6. Ahmad Rivai, Nasrudin Abd. Rahim, (2014). GUI for Photovoltaic (PV) array Monitoring System. UM Power Energy Dedicated Advanced Centre (UMPEDAC), Level 4, Wisma R & D, Lembah Pantai, University of Malaya, 59990 Kuala Lumpur, Malaysia Tel.
7. 7. Yasir Sheikh, Sudarshan Khond, Dr. M. M. Renge, (Dec 2019). Interfacing of PV Array with AC Grid using Twelve Pulse Converter. Helix, Vol. 9, No. 6, pp. 5884-5888.
8. T. Shanthi, N. Ammasai Gounden, (2007). Power Electronic Interface for Grid-Connected PV array using Boost Converter and Line-Commutated Inverter with MPPT. International Conference on Intelligent and Advanced Systems, pp. 882-886.
9. Koosuke Harada, Gen Zhao. (October 1993). Controlled power interface between solar cells and ac source. IEEE transactions on Power Electronics, Vol. 8, No. 4, pp. 654-662.

## INVESTIGATION ON EFFECT OF VARYING RAKE ANGLE AND FEED RATE ON STRESS INDUCED IN SPCT USING FEA

S. Randhir<sup>1</sup> and P. Karande<sup>2</sup>

Department of Mechanical Engineering, Veermata Jijabai Technological Institute Mumbai, India  
<sup>1</sup>randhirswapnil007@gmail.com, <sup>2</sup>pmkarande@me.vjti.ac.in

### ABSTRACT

This paper is a study of the effect of the variation in rake angle and feed rate on forces developed in a single point cutting tool (SPCT) during an orthogonal turning operation. Different values of induced forces are observed as a result of the variation in the rake angle of the tool and feed rate of the process. The effect of forces is measured by induced stress in the tool. For this study, three types of stress viz. Von-Mises, Max Principal, and Max Shear Stress are considered. The aim of this study is to investigate whether the increase in rake angle significantly reduces stresses and does not compromise on tool strength. A total of 30 sets of values of forces developed due to variation in rake angle and feed rate are considered and these values are obtained for six distinct values of rake angles (0°, 4°, 8°, 12°, 16°, 20°) and feed rates (0.022, 0.048, 0.088, 0.108, 0.132). A simulation for stress developed on the cutting tool was carried out in ANSYS Workbench 17.2. The simulation model was created in Solid Works and the results obtained indicate a considerable reduction in stress values as the rake angle increases irrespective of the decrease in lip angle and decrease in tool cross-section area.

**Keywords:** Feed rate, FEM, Orthogonal turning, Rake angle, SPCT.

### Introduction

The location of the cutting tool is critical in metal cutting operations. Its location is used as a basis to classify the cutting operations in two types viz. orthogonal cutting and oblique cutting.

The orthogonal cutting additionally known as two-dimensional metal cutting has its cutting edge oriented parallel to the workpiece. In the turning process, the workpiece is rotated about its axis while the tool traverses laterally along its length. During the process, the tool removes the material in the form of layers (chips) which creates three types of cutting forces on the tool i.e., the tangential force ( $F_y$ ), the feed force ( $F_x$ ), and the radial force ( $F_z$ ). The forces acting on the tool are shown in Figure.1. One important aspect of the orthogonal cutting process is that there does not exist any force in the direction perpendicular to the relative motion of the tool and workpiece. These developed forces act at the tip and on the sharp cutting edges of the tool. The magnitude of these forces is directly dependent on the parameters like feed rate, cutting speed, depth of cut, and rake angle of the tool.

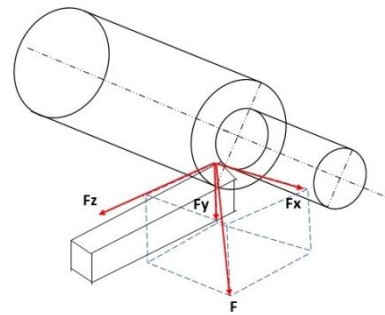


**Figure 1. Forces on Single Point Cutting Tool**  
**Machining Process Parameters**

The main parameters involved in metal cutting or machining are mentioned as follows:

- Feed rate: It can be described as the amount of lateral movement of the tool against the workpiece. The unit of the feed rate can be mm/rev or mm/mm. In the unit, the numerator is related to the tool while the denominator is related to the workpiece.
- Cutting speed: It is the rate of cutting edge's relative motion on the material of the workpiece.
- Depth of cut: It is the value of distance the tool is fed into the workpiece's surface.
- The geometry of the tool: The geometry of the tool is related to its various angles. The angles are denoted by the tool signature.
- Geometry and material type of workpiece.

## Cutting Forces

In the case of oblique cutting, there exist three forces as shown in Figure.1 and given below:

- $F_t$  signifies feed force, also known as thrust force which operates in a horizontal plane parallel to the workpiece's axis.
- $F_c$  is the tangential cutting force acting in the vertical plane on the workpiece surface. It is also called tangential force.
- $F_r$  denotes the radial force that acts along the radius of the workpiece in the horizontal plane.

We have considered the orthogonal turning process. In the orthogonal turning process, there exist only two components i.e., feed force and tangential force. Hence, the radial force is ignored or considered negligible in comparison to the other two forces.

### 1.3 Significance of Rake angle

Rake angle is the angle measured between the rake surface and the reference plane ( $\pi R$ ) or workpiece's perpendicular surface. Rake angle is the most important aspect while designing a cutting tool. It is provided on the tool to enable the chip flow during the machining away from the workpiece. Other than its primary function, it can improve the sharpness of the tool and also reduce the cutting forces and power requirements. Rake angle is classified into three types viz. positive rake angle, zero rake angle, and lastly negative rake angle.

A positive rake angle is used when the tool has to machine ductile workpiece and form a continuous chip. It also helps to avoid built-up edge (BUE) formation. However, a positive rake angle can indirectly affect the strength of the tool by decreasing the lip angle.

A negative rake angle is used for machining hard and brittle materials. The chips formed by these tools are non-continuous and broken. Due to its negative value, tool strength is more and it can bear a higher load. A negative rake angle does have some detrimental effects such as high deformation of chip material during its shearing process and requirement of high force and power since the negative angle decreases tool edge sharpness. Also, the high frictional force generated on the rake face during machining has a tendency of BUE.

## 2. Literature Review

Kosaraju, Anne, & Ghanta (2011) performed an experimental study to understand the effect of varying rake angle and feed rate on forces acting on SPCT. The experimental results showed that with the increase in feed rate, forces acting on the tool increased whereas they decreased as the rake angle increased. Rathod & Razik (2014) investigated the effect of temperature generated on a SPCT during the high-speed machining operation. Experimental and simulation data were compared and results indicate that the key factors accountable for heat generation are feed rate, tool's cutting speed, and depth of cut. Shambharkar, Kawale, & Choudhari (2016) performed an experimental and analytical study on SPCT to examine the effect of varying temperature and depth of cut on cutting forces. The results from the analytical study were compared with theoretical values and it was revealed that a sudden temperature rise weakens the tool near the tip area and promotes its failure. Kurekar & Khamankar (2017) performed an experimental and FEM analysis on SPCT to examine the outcome of cutting force and thrust force on the tool, and the comparative study showed that the cutting force affected the tool more than the thrust force. Shih (1996) created a plane-strain FEA method to employ it on a model of SPCT and hence, to investigate the effect of different back rake angles on the metal removal process. The outcomes from the study suggested that the dynamic coefficient friction will have less impact on cutting with a large value of back rake angle. Mahnama & Movahhedy (2012) combined a FEM model for chip generation in orthogonal turning with a dynamic framework for machine tool arrangement to accurately predict chatter and machine stability. The combined model was tested for stability by inputting different cutting conditions such as cut speed and width of cut. The results from the model indicated that a stability border is

obtained for cutting speed values ranging from mid to high speed. Also, the model showed the process damping phenomenon at lower speed range. Krishnan, Thakur, & Garg(2015) did a comparative study of FEM and theoretical analysis on deflection in SPCT due to machining parameters like feed rate, depth of cut, and tool's geometrical parameters or tool angles viz. side clearance angle and side rake angle. The analysis was carried out by varying the two geometrical parameters. The results indicated a decrease in tool deflection to some degree with increment in the side rake angle. The tool's deflection in axial direction decreased with increment in the side rake angle. But in the case of tangential deflection, it decreased with an increment in the side cutting edge angle. Radial deflection increased in both cases. Daniel, Terfa, & Kingsley(2017) conducted an experimental study on the effect of varying feed rate and rake angle on machining forces in orthogonal turning operation. Around 12 experiments were conducted and for three different values of rake angle ( $-5^\circ$ ,  $0^\circ$ ,  $5^\circ$ ) and four values of feed rate (0.1, 0.17, 0.24, 0.31 mm/rev). Results showed that the thrust force came out to be higher than the cutting force whereas the radial force was negligible. The values of forces increased with an increase in feed rate and decreased with increments in rake angle. Baldoukas et. al. (2008) performed an experimental study to observe the effects of rake angle, depth of cut, and type of workpiece material on the main cutting force and pattern or form of the chip for the orthogonal metal turning process. They removed chips from the machining process during the experiment, that were later collected and analyzed with important calculated forces to determine the optimum rake angle for each type of material. The results from the experiment denoted that the main cutting force increased with an increase in the depth of cut. Patil et. al.(2015) performed a FEM and theoretical analysis on SPCT to observe the

effect of varying rake angle and nose radius on force developed on tool edge and body during machining. The analysis was performed for  $30^\circ$ ,  $50^\circ$  rake angle and 0.3mm, 0.5mm nose radius values. The results showed that the tool with a  $5^\circ$  rake angle and 0.3mm nose radius had better cutting forces, lower wear, and yielded more tool life. Also, the nose radius affected the tool life and stress values. The higher nose radius value (0.5mm) has lower wear but less tool life and high stress as compared to the lower value (0.3mm). Batwara (2016) numerically simulated the turning process by FEM explicit dynamic tool. The study involved using the DOE technique to find the relationship among factors viz. input factors (depth of cut, cut speed, and back rake angle) and response factors (stress, strain). Regression analysis is performed to find input and output parameters relation and significant parameters. The result depicted that the depth of cut and cut speed are the most significant parameters. The optimum set of values from DOE are 250 (cutting speed), 0.6 (depth of cut), and 7.5 (rake angle). Uhlmann, Schulenburg, & Zettler (2007) performed a process simulation for high-speed cutting of Inconel 718. The issue related to segmented chip generation during machining high-affinity material is depicted in simulation for better understanding. The FEA solutions were obtained in ABAQUS for 2D and 3D simulations. Grzesik, Bartoszek, & Nieslony (2005) in their paper, had presented a combined thermal-mechanical model of plane strain. This model was used for orthogonal metal cutting with continuous chip forming. The model was integrated with thermal properties and heat partition values that were derived analytically for surface coated tools that have multiple layers. The results from finite element simulations show that the secondary shear zone exists and is localized. Coatings, in particular, have been affected by high temperatures. The highest temperature values are concentrated near the



interface between the chip and workpiece. Patil and Sarange(2014) presented a method for calculating tool powers, temperature distributions, and stress and deformation distributions on a SPCT during the metal cutting operation. An experimental study was performed and the results of which depicted that the temperature produced in the tool at the tooltip increased with the rise in the values of the depth of cut. It was noticed that the tool begins to vibrate at a cut depth of 2.5 mm. More heat is dissipated at the tool in this state, causing the tool to blunt. Kishawy & Elbestawi (1998) studied the impact of cutting temperature on the machined surface's integrity. It was concluded from the results that temperature during the cutting process has a considerable amount of impact on the integrity of the machined surface. The temperature produced during machining was the cause of the unwanted tensile residual stresses generated on the surface. Hence, it was concluded that the temperature during cutting is impacted due to various method parameters and it is essential for controlling the induced tensile residual stresses. Lalwani, Mehta, & Jain(2007) in their paper had investigated cutting forces viz. thrust force, feed force, and cutting force generated on tool and surface roughness of workpiece. The experimentation was performed by finishing operation of hard turning on steel (Grade MDN250) using a coated ceramic tool. The cutting parameters considered in his experiment are the rate of feed, cutting speed, and depth of cut. The results showed that cutting forces and surface roughness do not differ significantly with experimental machining speeds value fluctuating from 55 to 93 m/min. Gunay et. al.(2004) had conducted experiments on AISI 1040 workpiece material to investigate the effect of varying the rake angle on the main

machining force. The experimental and empirical findings were compared using the Kienzle approach, and it was discovered that with the increase in the rake angle value increased from negative to positive, the main cutting force decreased. The difference between the analytical method and the experiments was in the range of 10%–15%. Özel, Hsu, & Zeren(2004) in their paper, had used CBN as tool material and hardened AISI H13 steel bars as workpiece material to investigate the effects on workpiece toughness, edge geometry of tool's cutting edge, rate of feed, cutting speed, and surface roughness. In the results, the effect of two factors' interactions of workpiece hardness and tool's edge geometry, feed rate, and edge geometry appeared to be significant. Better surface roughness results had been found in the case of lower workpiece hardness and honed edge geometry of the tool.

### 3. Methodology

A FEM simulation is carried out on a SPCT to analyse the effect of forces by considering stress induced in the tool.

#### 3.1 Modelling

The first step is to model the cutting tool on which analysis will be performed. The cutting tool is modelled in Solid works CAD software. The tool is a High-speed tool and the tool signature is 0-7-7-7-15-15-0.5. In this particular study, the rake angle and feed rate are varied and the corresponding values of forces and are used to determine respective stresses. Six values of rake angle ( $0^\circ$ ,  $4^\circ$ ,  $8^\circ$ ,  $12^\circ$ ,  $16^\circ$ ,  $20^\circ$ ) and five feed rates (0.022, 0.044, 0.088, 0.108, 0.132) are considered. Fig. 2 shows the cad model of  $4^\circ$  rake angle SPCT. Correspondingly six cad models of the cutting tool are designed for different rake angles

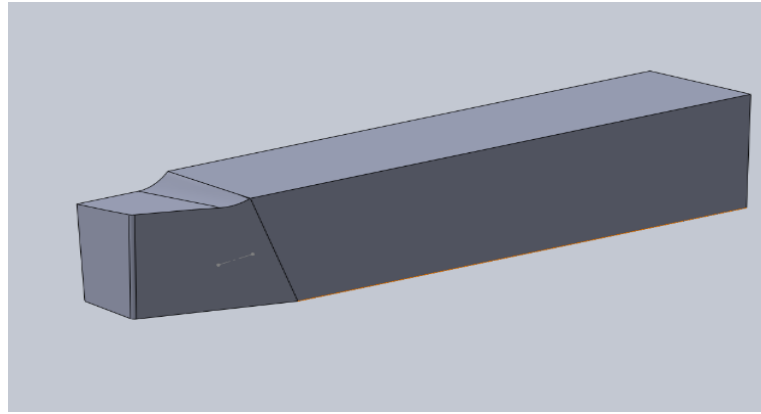


**Figure2. CAD Model of SPCT of 4° Rake Angle**

### FEM analysis

The FEM simulation is carried out on ANSYS workbench 17.2. The no. of FEM simulation carried out are 30, 5 simulations for each value of rake angle. The 5 simulations correspond to the 5 values of feed rates. The forces which are input values for simulation are referred from [1]. The forces and appropriate boundary

conditions are applied and results are evaluated.

### Material Properties

The material used for the tool is HSS and for the workpiece is EN8. Table 1 has the mechanical properties of both materials. These values are the input parameters during the simulation.

**Table1. Material Properties**

	HSS	EN8
Density (Kg / m <sup>3</sup> )	8160	7850
Young's Modulus (Gpa)	200	190
Poisson's Ratio	0.27	0.3
Tensile Strength (Mpa)	1000	280
Compressive Strength (Mpa)	3250	860
Ultimate tensile Strength (Mpa)	1200	550

## 4. Results and Discussion

The input values for simulation are shown as per in Table 2. The table shows feed rate, rake angle, and its corresponding forces. Three forces namely Feed force  $F_x$ , cutting force  $F_y$  and radial force  $F_z$  are observed. These values are considered to be acting on the cutting edge and edge of nose radius. The stresses obtained from simulation are of three types Von-Mises, Max principal, and Max Shear, and their values are expressed in tabular form as shown in table 2. The simulation results are shown in fig.3 (a), (b), and (c). The values from table 2 are represented in graphical format. The line graphs as shown in fig.4 (a), (b), (c), (d), (e),

and (f) are plots of stress to feed rate for a particular rake angle. These graphs show that the value of all three stresses increases as the feed rate increases. Von-Mises have the highest value followed by Max Shear and lastly Max principal Stress. It is observed by comparing these graphs that a smaller rake angle has a high value of stresses and it starts to descend relative to each other as the rake angle increases. From the graph of 8° rake angle, the max shear and max principal have a flat trend whereas vonmises have the highest value for 0° amongst all the other values of rake angles. The stresses start to decrease from 12°, 16° and

are significantly reduced in 20°. The lowest values are observed for 20°.

The graph as shown in fig.5 (a), (b), and (c) are plots of stress vs rake angle. For the plot of Von-Mises vs Rake angle, the different curve line is for different values of feed rate. The lowest feed rate has correspondingly lower induced stresses. The highest value is observed at 0° and the curve descends to meet the lowest value at 20°. The stresses in the plot of Max principal stress vs Rake angle have its highest value at 4° for all feed rates and it descends to give the lowest value at 20°. The stresses in the plot of Max Shear vs Rake angle show high variation near 8° value. The max shear stress attains the lowest value at 8° followed by a steep increase for further values of angle.

Here 20° is the second lowest value for max shear.

The graph in fig.6 (a), (b), and (c) are % variation of stress as rake angle increases. In the case of the graph for Von-Mises and Max principal, the highest positive variation is for 4° and the stress variation is 85% and 132% respectively. Similarly, the highest negative variation is 8° and 20° and the value of variation is -37%, -49%, and -42%, -50% respectively. The plot of max shear stress is different than the previous two. The max and minima occur at 12° and 8° respectively and their values are -84% and 285% respectively. All the values of variations are considered for 0.044 and 0.132 feed rate values.

**Table2. Simulation Data**

Group No.	Independent Variables			Dependent Variables			Stress (Mpa)		
	Exp No.	Feed	Rake Angle	Fx (Feed Force)	Fy (Cutting Force)	Fz (Radial Force)	Equivalent Von -Mises	Max Principal	Max Shear
1	1	0.022	0	132.14	58.78	5.69	119.42	43.78	68.08
	2	0.044		220.36	101.32	10.14	175.80	49.57	100.59
	3	0.088		623.83	217.37	17.84	497.69	140.35	284.77
	4	0.108		819.48	262.82	22.36	653.78	184.36	374.08
	5	0.132		910.93	306.05	31.27	726.74	204.94	415.83
2	1	0.022	4	151.40	62.97	2.62	149.57	50.86	85.21
	2	0.044		332.40	125.99	1.33	324.74	114.78	185.35
	3	0.088		500.90	191.43	0.47	490.61	173.42	280.01
	4	0.108		604.00	222.93	2.66	587.53	209.17	335.46
	5	0.132		737.10	267.49	7.55	713.51	254.04	407.41
3	1	0.022	8	87.75	54.48	2.41	96.85	26.92	14.89
	2	0.044		187.38	111.20	3.99	204.00	58.02	29.19
	3	0.088		329.37	191.25	6.03	356.36	102.48	49.17
	4	0.108		414.29	228.97	8.70	440.78	128.83	56.15
	5	0.132		618.08	228.97	14.28	636.55	193.69	65.69
4	1	0.022	12	103.04	49.09	3.94	105.53	31.88	59.51
	2	0.044		183.77	93.22	8.18	190.78	55.95	107.41
	3	0.088		306.04	156.10	11.92	318.92	93.81	173.57
	4	0.108		371.81	189.30	15.10	387.01	113.75	217.90
	5	0.132		430.57	224.30	21.02	449.54	129.98	252.88
5	1	0.022	16	104.69	50.70	3.48	108.35	31.71	61.08
	2	0.044		184.41	90.28	5.51	191.63	56.04	108.02
	3	0.088		290.85	147.07	8.63	304.81	88.02	171.68
	4	0.108		345.62	177.14	9.75	363.73	104.63	204.81
	5	0.132		489.41	239.98	14.93	508.46	148.58	286.70
6	1	0.022	20	89.75	49.13	7.51	86.03	23.59	48.27
	2	0.044		147.88	86.21	12.90	144.59	38.41	80.95
	3	0.088		217.62	135.50	18.91	218.05	56.25	121.81
	4	0.108		243.77	157.40	19.44	248.45	63.48	138.65
	5	0.132		289.15	190.90	25.57	296.48	74.28	165.27

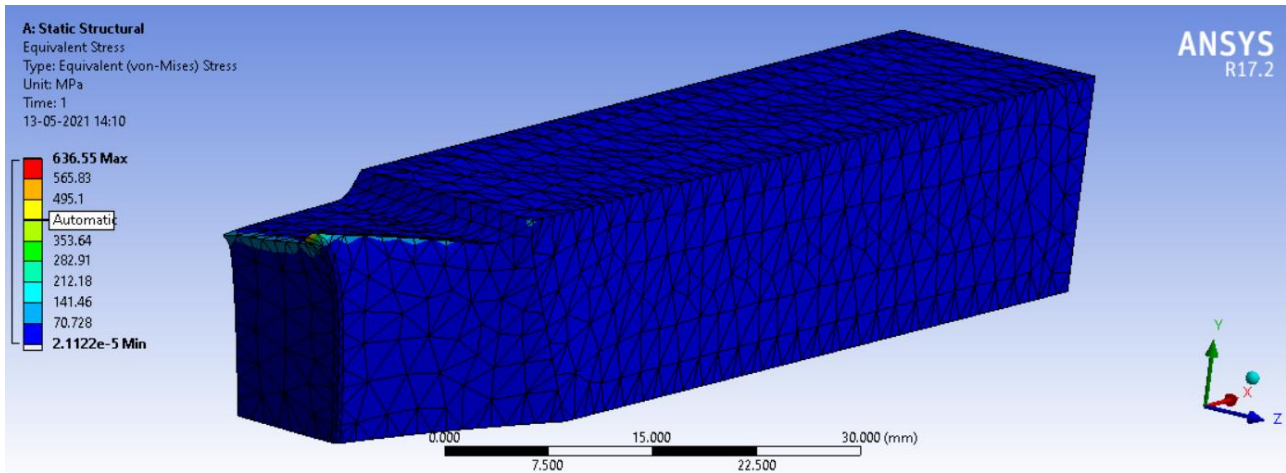


**Fig.3**  
**Figure3(a). FEM Von-Mises Solution**

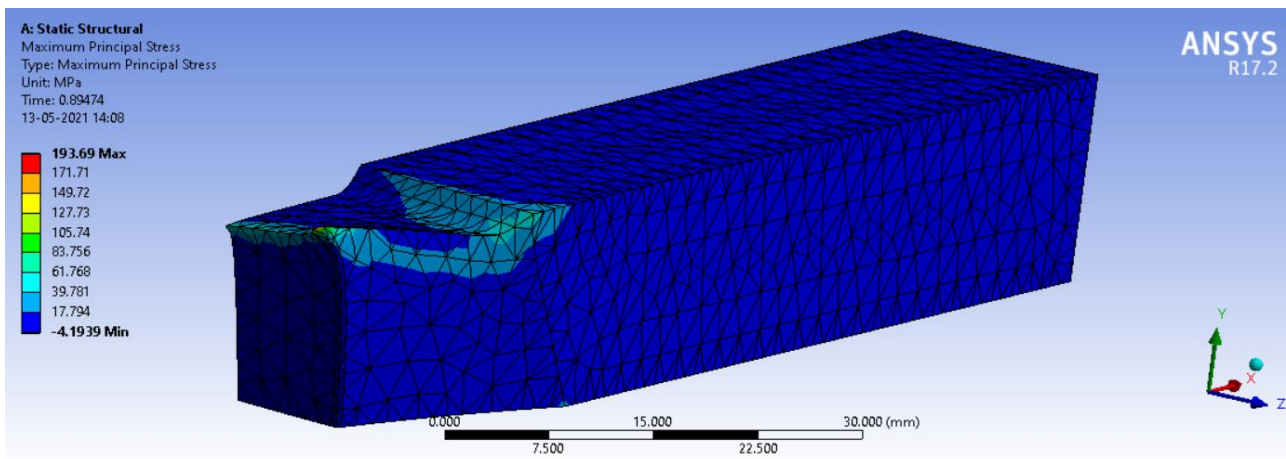


**Figure3(b). FEM Max Principal Solution**

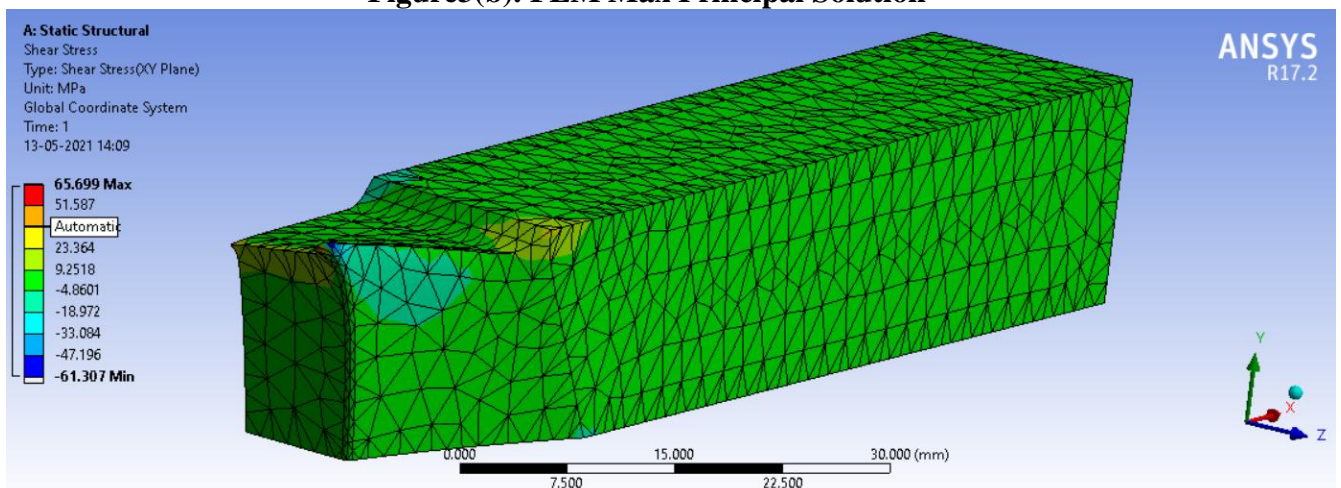


**Figure 3(c). FEM Max Shear Solution**

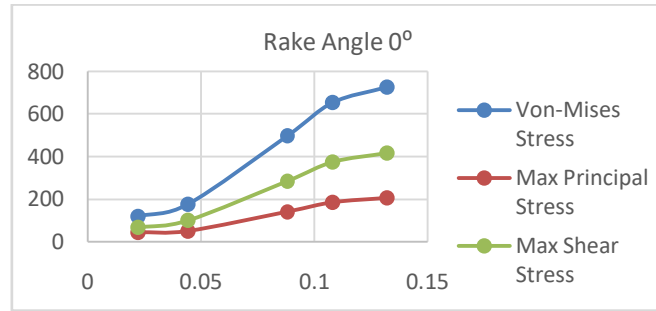


Figure4(a). StressesVariation vsFeed Rate at 0° Rake Angle

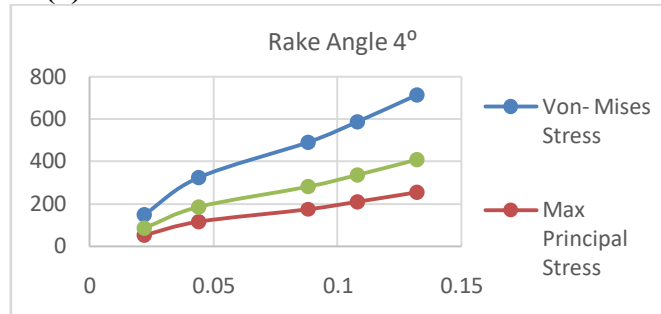


Figure4(b).StressesVariation vsFeed Rate at 4° Rake Angle

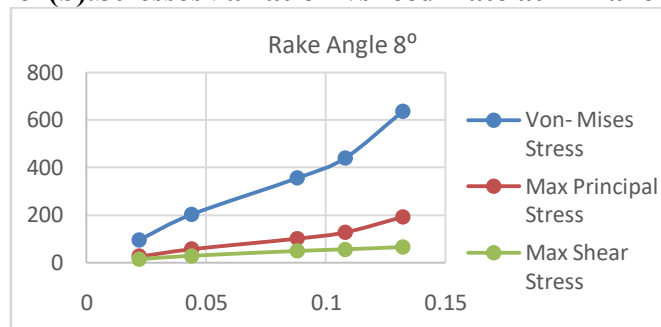


Figure 4(c).StressesVariation vsFeed Rate at 8° Rake Angle

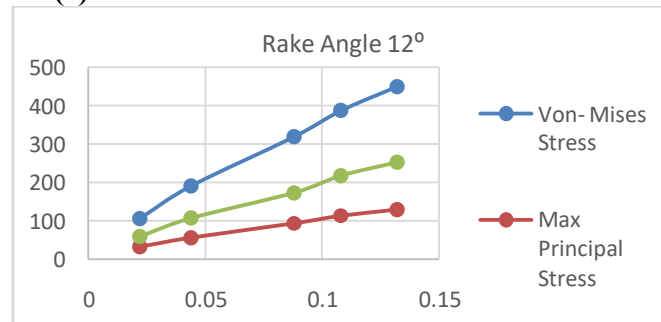


Figure4(d).StressesVariation vsFeed Rate at 12° Rake Angle

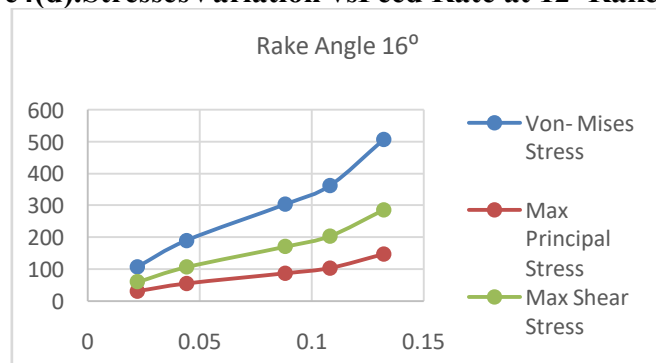


Figure4(e).StressesVariationvsFeed Rate at 16° Rake Angle

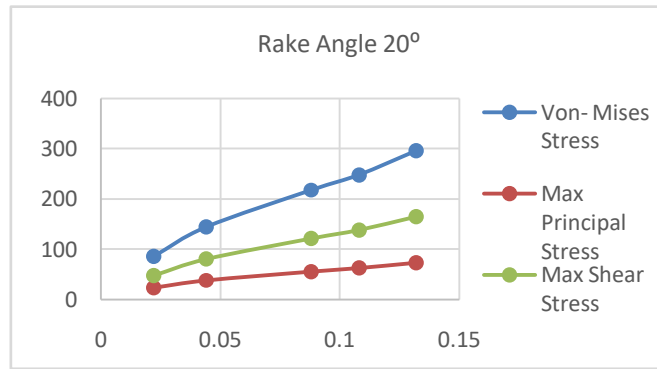


Figure4(f).StressesVariationvsFeed Rate at 20° Rake Angle

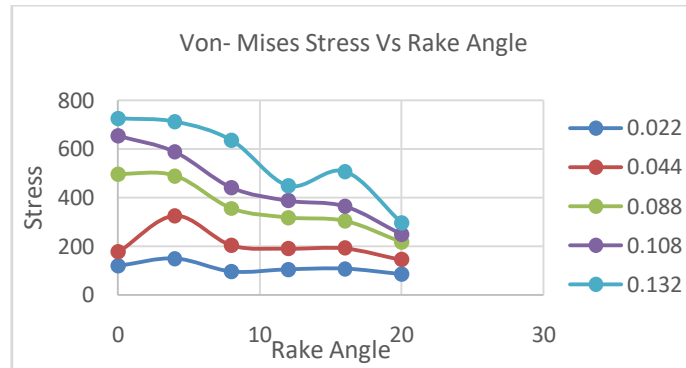


Figure5(a). Von-Mises StressVariation w.r.tRake Angle

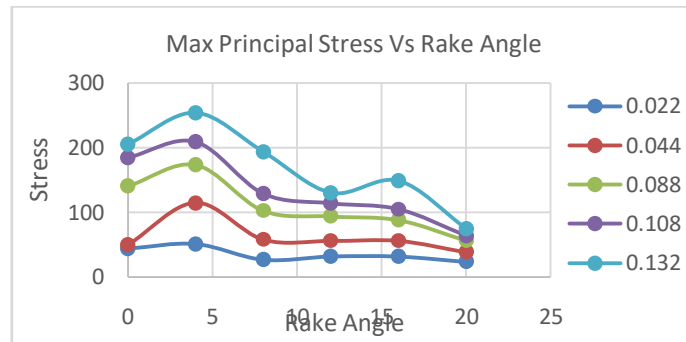


Figure5(b). Max Principal StressVariation w.r.t Rake Angle

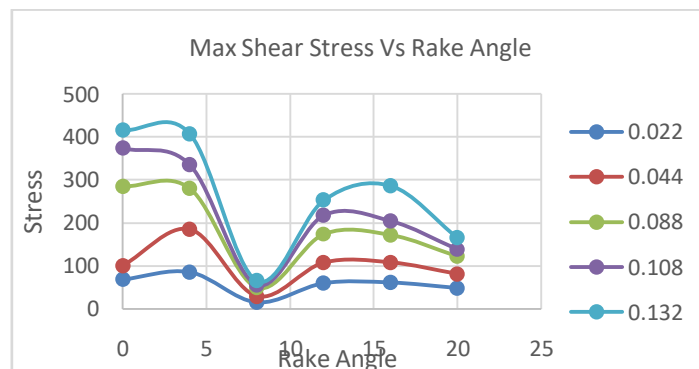
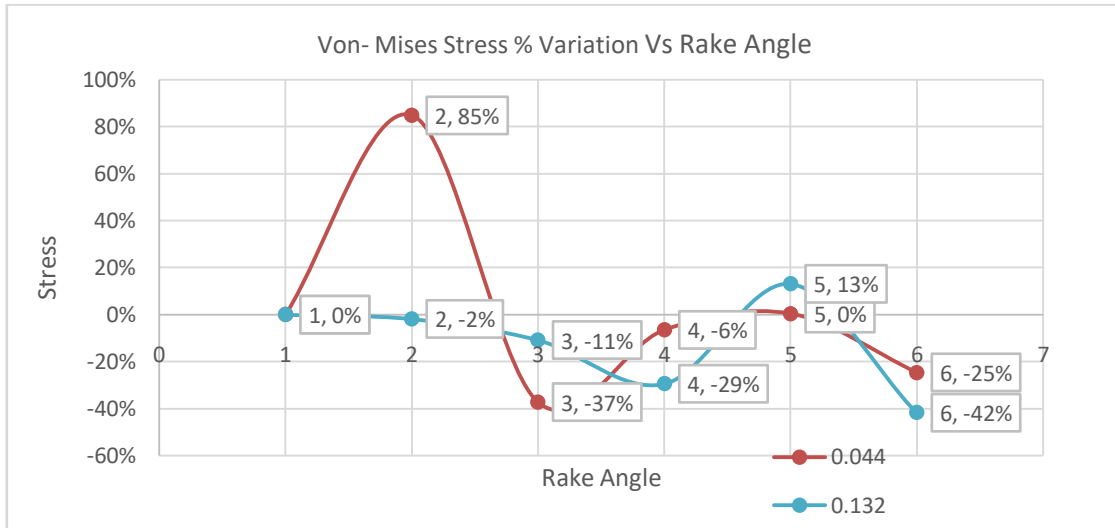
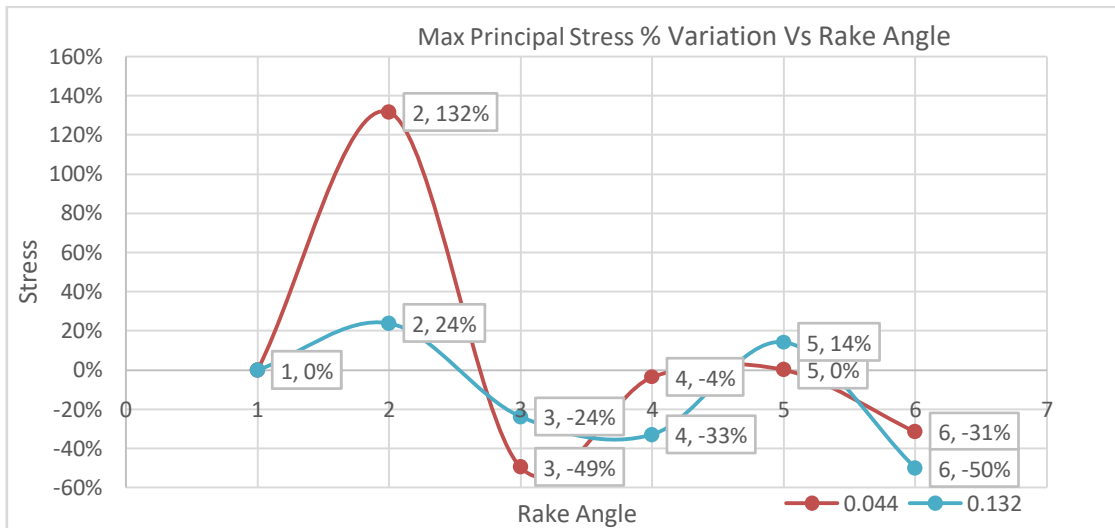


Figure5(c). Max Shear Stress Variation w.r.tRake Angle



**Figure6(a).Percentage Variation of Von-Mises Stress with Rake Angle**



**Figure6(b).Percentage Variation of Max Principal Stress with Rake Angle**

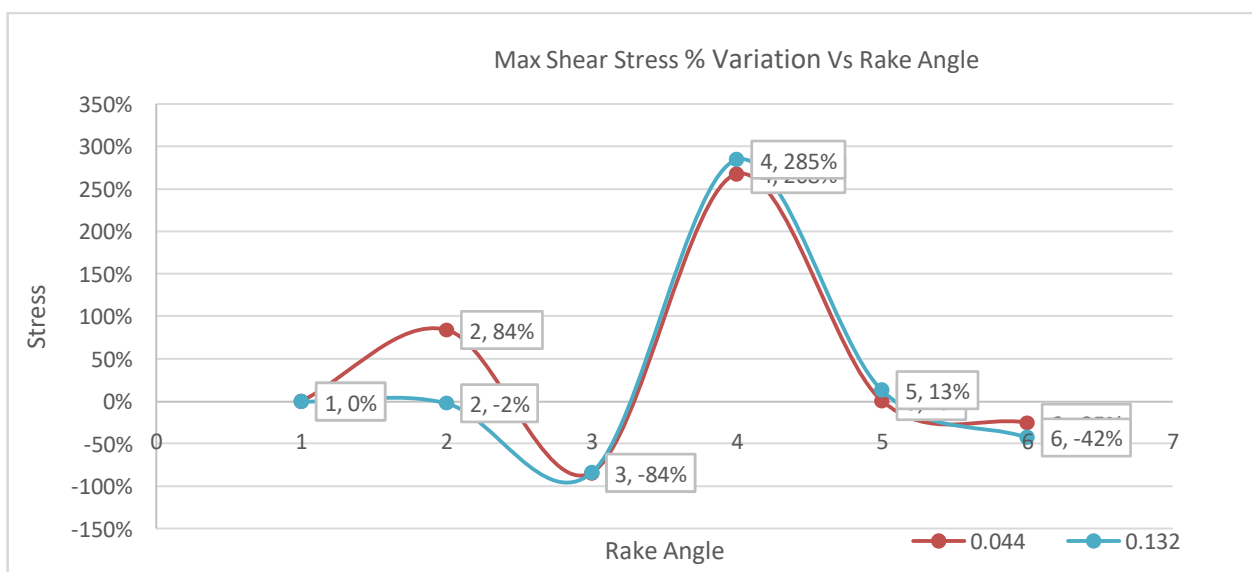


**Figure6(c).Percentage Variation of Max Shear Stress with Rake Angle**

### Conclusions

The FEM simulation of the effect of forces on stress induced by varying the rake angle and feed rate is successfully implemented. The conclusions drawn from the simulation are stated as follows:

- It is studied from the observations that among the three types of stresses, Von-Mises have the highest value of induced stress followed by Max shear and Max principal stresses.
- As the feed rate is increased, the stresses also showed an increasing trend. The feed rate of 0.132 has the highest amount of stress values.
- Max principal stress which is important for brittle nature material like HSS has its highest value for 4° rake angle. Whereas, in

Von-Mises stresses the highest value is observed at 0° and 4°. The Max Shear also has its highest value at 4°.

- The higher stresses at lower rake angles indicate the downside of lower rake angles and its need for higher cutting forces and high-power requirements.
- The lowest value for Von-mises and Max principal stress is at 20° whereas for max shear it occurs at 8°.

The graphical plots indicate that the stresses tend to decrease as the rake angle increases because higher values of the rake angle require lower cutting forces. Hence lower values are observed at 20°.

### References

1. Baldoukas, A., Soukatzidis, F., Demosthenous, G., & Lontos, A. (2008). Experimental Investigation of The Effect of Cutting Depth, Tool Rake Angle and Workpiece Material Type on The Main Cutting Force During a Turning Process. *International Conference on Manufacturing Engineering*, 47-56.
2. Batwara, A. (2016). Finite Element Method Simulation of Turning Process with Single Point Cutting Tool: A Numerical Study. *European Journal of Advances in Engineering and Technology*, 3(9): 12-19.
3. Daniel, I., Terfa, G., & Kingsley, N. (2017). A Study on the Effect of Rake Angle and Feed Rate on Cutting Forces during Orthogonal Cutting. *European Journal of Advances in Engineering and Technology*, 4(4): 268-272.
4. Grzesik, W., Bartoszek, M., & Nieslony, P. (2005). Finite element modelling of temperature distribution in the cutting zone in turning processes with differently coated tools. *Journal of Materials Processing Technology*, 164, 1204-1211.
5. Gunay, M., Aslan, E., Korkut, I., & Seker, U. (2004). Investigation of the rake angle on main cutting force. *Journal of Machine tools & Manufacture*, 44(9): 953-959.
6. Kishawy, H., & Elbestawi, M. (1998). Effect of edge preparation and cutting speed on surface integrity of die materials in hard machining. *Manufacturing Science and Engineering Conference*, 269-276.
7. Kosaraju, S., Anne, V., & Ghanta, V. (2011). Effect of Rake Angle and Feed Rate on Cutting Forces in an Orthogonal Turning Process. *International Conference on Trends in Mechanical and Industrial Engineering*, 150-154.
8. Krishnan, G., Thakur, A., & Garg, S. (2015). Comparative Study of Profile Errors due to Cutting Forces and Tool Geometry of Single Point Cutting Tool. *International Journal of Scientific and Research Publications*, 5(9): 1-13.
9. Kurekar, P., & Khamankar, S. (2017). Finite Element Analysis of Single Point Cutting Tool. *International Journal of Engineering and Technology*, 4(9): 264-268.
10. Lalwani, D., Mehta, N., & Jain, P. (2007). Experimental investigations of cutting parameters influence on cutting forces and surface roughness in finish hard turning of MDN250 steel. *Journal of Materials Processing Technology*, 206(1): 167-179.
11. Mahnama, M., & Movahhedy, M. (2012). Application of FEM simulation of chip formation to stability analysis in orthogonal



- cutting process. *Journal of Manufacturing Processes*, 14(3): 188-194.
12. Özel, T., Hsu, T., & Zeren, E. (2004). Effects of cutting edge geometry, workpiece hardness, feed rate and cutting speed on surface roughness and forces in finish turning of hardened AISI H13 steel. *The International Journal of Advanced Manufacturing Technology*, 25(3): 262-269.
  13. Patil, M., Patil, R., & Kolhe, K. (2015). Finite Element Analysis Study of Cutting Forces of Geometry of Single Point Cutting Tool. *International Journal of Pure and Applied Research in Engineering and Technology*, 3(10): 49-64.
  14. Patil, M., & Sarange, S. (2014). Numerical Analysis to Determine the Distribution of Tool Forces and Temperatures of Single Point Cutting Tool. *International Journal of Science and Research*, 3(4): 765-771.
  15. Rathod, S., & Razik, M. (2014). Finite Element Analysis of Single Point Cutting Tool. *Internal Journal of Modern Engineering Research*, 4(3): 12-13.
  16. Shambharkar, S., Kawale, A., & Choudhari, C. (2016). Analysis of Single Point Cutting Tool Using ANSYS. *Internal Journal on recent and innovation trends and communication*, 4 (5): 331-338.
  17. Shih, A. (1996). Finite Element Analysis of The Rake Angle Effects in Orthogonal Metal Cutting. *International Journal of Mechanical Sciences*, 38(1): 1-17.
  18. Uhlmann, E., Schulenburg, M., & Zettler, R. (2007). Finite Element Modeling and Cutting Simulation of Inconel 718. *Annals of the CIRP*, 56(1): 61-64.

**CUTLERY PRODUCTS FROM SUGARCANE BAGASSE****K. M. Tajne<sup>1</sup>, S. Rinayat<sup>2</sup>, S. Walke<sup>3</sup>, S. Dhanke<sup>4</sup>, V. Chaudhari<sup>5</sup> and V. Puram<sup>6</sup>**

Civil engineering department Government College of engineering Nagpur India

**ABSTRACT**

Rising concerns towards adverse effects associated with the decomposing characteristics of cutlery items manufactured from synthetically derived plastics are expected to force the kitchen utensil manufacturers to deploy disposable materials including wood, bagasse, husk, and coconut coir. Furthermore, these disposable cutlery raw materials, particularly, bagasse can decompose within 90 days as compared to the conventionally used plastics which take more than 500 years. Nowadays the biodegradable cutlery is the best option to use. It is beneficial to nature. Rising awareness regarding the adverse effects of non-biodegradable plastic, including severe consequences on aquatic animals, is one of the major factors for the growth of the market. The rising demand for eco-friendly, safe, and sustainable cutlery owing to an increasing number of restaurants, fast food joints, and cafeterias is fueling the demand for biodegradable plates and cups. Costs associated with biodegradable plates, cups, spoons, and fork are higher as compared to the traditional disposable cutleries, thereby hampering the market growth.

**keywords** -Green, Eco-friendly, Sustainable, Recyclable, Recycled, Renewable, Compostable, Biodegradable.

**General****Introduction**

The main aim of the paper is to analyze the properties of green material and its impact on sustainable design. The bagasse is a by-product of sugarcane so it does not contain any hazardous material. Bagasse is a fibrous material that is obtained from the residual that remains after the juices are removed from the sugarcane stalk. This fibrous portion generally becomes a waste product after the juices are separated from the. However, there is a high risk of food contamination by the use of plastic cutlery. This raises concerns regarding the impact of such plastic cups on the environment, whether in terms of rising production or from dumping waste plastic disposable cups.

Bagasse is remolded to a kind of paper from which the cutlery items plates, cups, and glasses are manufactured. The ability to recycle, its lightweight, and other physical attributes of disposable cups will continue to make them the better most option of packaging food beverages. Disposable cups are designed in a way that they can hold both, hot and cold substances, which further propels their applicability in the global food & beverage industry.

Sugarcane is a material that is quickly renewable and doesn't cause harm to the environment. As bagasse is a by-product of sugarcane obtained at the time of sugar production, it does not require additional cultivation areas and has a great impact on the

ecosystem. on the contrary: Wood paper production wastes more energy and resources than bagasse paper production. It is a biodegradable, sustainable, eco- friendly one. Plates and bowls are made from plant extract i.e., bagasse. It is a 100% natural product. It is more sustainable than any other alternative. The main advantage of the products from sugarcane bagasse is to eliminate waste from landfills and helps to strive better environment.

**Composition of bagasse**

Sugarcane bagasse is a cheap agro- based waste material. These biomass materials have a lot of potentials to be converted into useful products such as carbon. Sugarcane bagasse was extracted by sodium hydroxide.

Several characterizations have been done to analyze the chemical properties of sugarcane bagasse after extraction by sodium hydroxide including XRD, XRF, SEM-EDS, and air permeability. The following is the information of tests which is used to determine the composition of bagasse.

**SEM**

The use of scanning electron microscopy as an analytical technique proved to be of great importance and versatility for studying the biomass structure. Figure 1 shows the morphological characteristics of the steam pre-treated bagasse in the presence of CO<sub>2</sub> or SO<sub>2</sub> as well as of the untreated material, obtained by scanning electron microscopy (SEM). SEM images of untreated sugar cane bagasse (A, B,

and C); (A) General view of the sample showing the fiber's (mainly); (B and C) higher magnification image of fiber surface; SEM images of sugarcane bagasse pretreated with SO<sub>2</sub> (190°C/5 min) (D, E, and F); (D)

General view of the sample showing the fibers (mainly); (E) higher magnification image of fiber surface (arrows in the D image); (F) higher magnification image of fiber surface extremity; SEM images of the bagasse pretreated with CO<sub>2</sub> (205°C/15 min) (G, H and I); (G)

General view of the sample showing the fibers (mainly); (H) and (I) higher magnification images of fiber surface (arrows in the G image). Untreated bagasse sample (Figure 1A, B, C) presents a rigid and compact morphology, while the one submitted to pre-treatment with SO<sub>2</sub> (Figure 1D, E, F) or CO<sub>2</sub> (Figure 1G, H, I) shows a more unorganized morphology and greater exposure of the fibers. After pre-treatment, the most exposed cell wall structure allows for greater accessibility to hydrolytic enzymes, which facilitates the hydrolysis of lignocellulosic biomass.

After pre-treatment, the most exposed cell wall structure allows for greater accessibility to hydrolytic enzymes, which facilitates the hydrolysis of lignocellulosic biomass.

### Characterization of bagasse

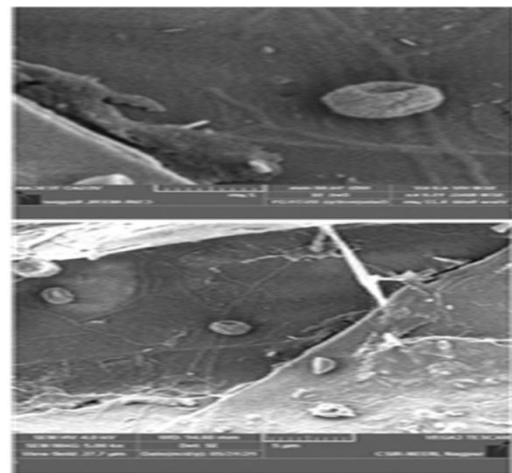
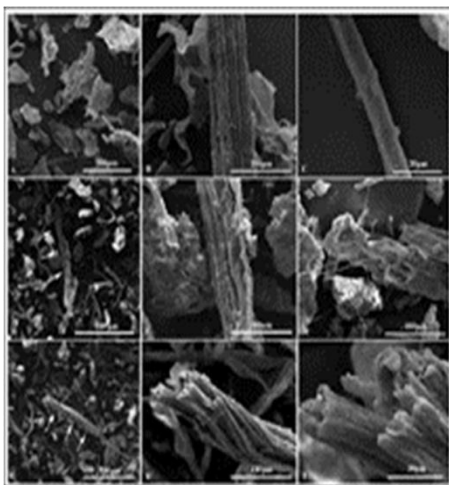
A morphological analysis of the untreated sugarcane bagasse (SB- Ori) and sugarcane bagasse treated with NaOH (SB-NaOH) was performed. For this analysis, a scanning

electronic microscope (SEM) model JSM-5800LV was used. Initially, the bagasse sample was subjected to dry in an oven at 60°C/24 h. This assembly was maintained in a vacuum-desiccator before the analysis. The sample was then placed on metallic cylindrical holders called "stubs", measured at 10 mm in diameter, and secured with double-sided adhesive tape. The sample in the stubs placed in the SEM. The acceleration voltage was set at 1.5kV, 1.8kV, or 2.0kV depended on the types of samples.

The morphology of SB fibers was investigated using SEM to determine the change of fiber surface and morphology during extraction processing, the morphology of untreated and treated SB fibers, respectively. The surface of untreated SB fibers presented the smooth surface due to the

The images obtained by scanning electron microscopy on the surfaces of the untreated sugarcane bagasse showed two morphological features which were pith and fiber structures (labeled as P and F, respectively) The fiber surface was formed by parallel stripes and partially covered with residual material. The pith was a more fragile and fragmented structure containing pits, which were small pores connecting neighboring cells on the surface of the walls.

The electron micrograph of the cross-section of untreated bagasse showed a large void and loose packing of the fibers and the wall of untreated fibers was intact.



The morphology of bagasse is getting damaged by the alkaline action. After being treated with

NaOH, the bagasse bundles were started to dismantle and the fibers were detached from the

others.

Alkaline pre-treatment by adding NaOH solution could cause swelling of the biomass, which would increase the internal surface area of the lignocellulose particles, as well as the weakening of the structural integrity of the lignocellulose and breaking of bond linkages between lignin and the other carbohydrates (cellulose and hemicellulose), causing greater accessibility and digestibility of the cellulose fraction, and thus, it could be depolymerized into fermentable sugars.

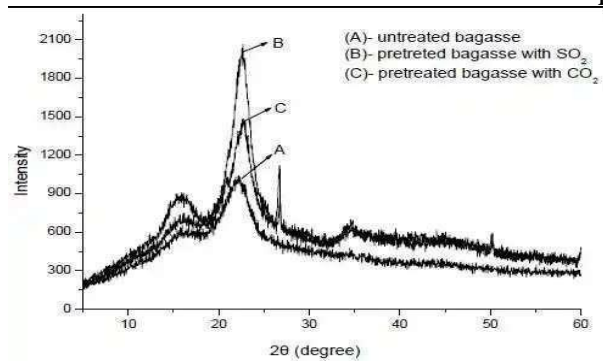
**X-ray diffraction (XRD)**

Diffraction patterns of the sugar cane bagasse samples: (A) untreated bagasse; (B) pre-treated bagasse with SO<sub>2</sub> (190°C/5 min); (C) pre-treated bagasse with CO<sub>2</sub> (205°C/15min)

The figure shows diffraction patterns of untreated bagasse (A) and sugar cane bagasse pretreated with SO<sub>2</sub> (B) or CO<sub>2</sub> (C). As can be observed all samples exhibit typical cellulose diffraction peaks, where the highest peak corresponds to the 002 crystallographic planes. The crystallinity index was calculated according to Equation 1 (Methods session). The untreated sugar cane bagasse showed a lower crystallinity (CI = 48.0%) when compared to samples pre-treated with SO<sub>2</sub> (CI = 65.5%) and CO<sub>2</sub> (CI = 56.4%). Many studies indicate that there is an increase in the value of this index when the biomass is subjected to pre-treatment by the steam explosion [19]. The phenomenon is due mainly to the removal of a certain amount of lignin and hemicellulose (amorphous substances) and not necessarily due to changes in the crystalline

structure of the biomass.

As expected, the crystallinity index for the bagasse pretreated with SO<sub>2</sub> (65.5%) was higher than that of CO<sub>2</sub> pre-treated bagasse (56.4%). Indeed, it was observed a more effective removal of hemicellulose to the liquid fraction (63.8%: 7.0% xylose as oligomers and 56.8% of monomeric xylose) using the SO<sub>2</sub> steam pre-treatment than that using CO<sub>2</sub> that showed 40.5% hemicellulose removal: (21.5%) of xylose in oligomeric form and 19.0% in monomeric form) [10]. In this work, the increase of the crystallinity index in the pre-treated samples is explained by the partial removal of the hemicellulose fraction. The amount of glucose released from cellulose (amorphous region) was not relevant in the pre-treatment step.



The high-pressure steam modifies the plant cell wall structure, yielding a dark brown material from which partially hydrolyzed hemicelluloses are easily recovered by water-washing, leaving a water-insoluble fraction composed of cellulose, residual hemicelluloses, and a chemically modified lignin.

**Table 1 Elements found in the sugarcane bagasse (untreated and treated) as**

**Table 1** Elements found in the sugarcane bagasse (untreated and treated) as indicated in the spectrum in Fig. 5.

Element	Untreated Sugarcane Bagasse		Sugarcane Bagasse Treated with 1.0M NaOH	
	Weight %	Atomic %	Weight %	Atomic %
C	60.59	68.41	52.46	61.94
O	33.53	28.42	33.46	29.66
Na	2.49	1.47	10.10	6.23
Mg	1.55	0.87	2.10	1.23
Si	1.50	0.73	1.88	0.95

3 / 5

### X-ray fluorescence (XRF) analysis

The samples of treated and untreated sugarcane bagasse (liquid) were poured into special cups with supporting films. Diluents were sometimes added to obtain sufficient samples. The samples could not be measured in a vacuum because they would evaporate, causing the measurement in the air as possible. However, the air could absorb much of the radiation, making it impossible to measure light elements. The

spectrometer chamber was therefore filled with He gas.

The samples would not evaporate and hardly any radiation was absorbed.

The product was determined by X-ray fluorescence spectrometer (XRF) and the summarized chemical compositions of sugarcane bagasse sample were shown in Table 2.

**Table 2** List of elements found in the treated and untreated sugarcane bagasse with concentration (%).

Element	Concentration (%)	
	Untreated sugarcane bagasse (SB-Ori)	Sugarcane bagasse treated with NaOH (SB-NaOH)
Ca	0.0359	-
Cl	0.0796	0.0718
H <sub>2</sub> O	98.5	99.9
Na	0.669	-
P	0.0323	0.0199
S	0.638	0.0133
Sb	0.0021	0.002
Sn	0.0019	0.0018

The element with the highest concentration found by using XRF in untreated sugarcane bagasse was water, H<sub>2</sub>O (98.5 %), followed by sodium, Na (0.669 %), and sulfur, S (0.638 %). The concentration of each element was decreased (except H<sub>2</sub>O) after being treated with NaOH. It was well known that the non-cellulosic materials like hemicelluloses and lignin were presented in the form of a network that bound the fiber bundles in a composite-like structure. During the alkali treatment, hemicelluloses that have been removed would weaken this network and some lignin's would become loose and remove due to this damaged network. In this study, the bagasse was chosen as it consisted of approximately 50% cellulose and 25% each of hemicelluloses and lignin.

Chemically bagasse contains about 50%  $\alpha$ -cellulose, 20% pentosans, and 2.4% ash. Because of its low ash content, bagasse offers numerous advantages in comparison to other crop residues such as rice straw and wheat straw, which have 17.5% and 11% of ash content, respectively.

### Air permeability

The term Permeability describes how easy fluids are transported throughout the structure

of a porous solid material. This physical property is extremely important to the development of durable materials since it can be associated with their structural properties and resistance to penetration of environmental degradation.

Permeability strongly depends on the microstructure of materials. Air permeability is a physical property of extreme importance to the development of durable fibrous cellulosic products and it strongly depends on their microstructure.

### Conclusion

Based on the findings of the study, the following conclusions were drawn.

SEM showed an increase in internal surface area of the lignocellulose particles and weakening of the structural, while EDS showed 60.59 % content of carbon. The element with the highest concentration that found by using XRF in untreated sugarcane bagasse was water, H<sub>2</sub>O (98.5 %), followed by sodium, Na (0.669 %) and Sulphur, S (0.638 %).

The crystallinity index values obtained from XRD patterns showed that pre-treated materials have higher values (CI (SO<sub>2</sub>) = 65.5%, CI(CO<sub>2</sub>) = 56.4%) when compared with

untreated material (CI = 42.5%), due to the partial removal from the bagasse of its hemicelluloses content

**Methodology**

Bagasse is a newly developed material for the production of tableware. Compared to other raw materials, bagasse plates and cups have a longer life span and better appearance, compared to polyester, bagasse is more environmentally friendly, which can be easily absorbed or recycled. Bagasse pulp is used as

raw material after the pulp, the molding and drying section will go through the sterilization and edge trimming section before packaging the tableware.

**Manufacturing stages:**

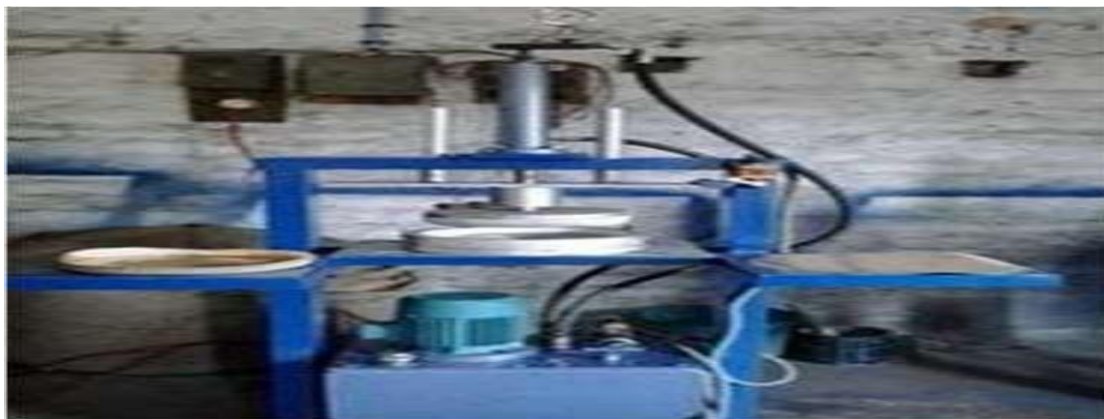
**1) Pulping:** Soak the pulp paper board and put it into the hydraulic pulper. After the pulp, the pulp will go into the mixing tank and add water and oil, then the pulp supply goes to the tub for machine vacuum suckering and forming.



**2) Forming:**

Construction is the key process in a production line. This process is quantitative pulp supply, backflushing power supply, vacuum

dewatering, and forming. With advanced technology to eliminate holes, uneven thickness during production to reduce defective items. The semi-finished product will be transported in a drying mold for acidity.



**3) Shaping and drying:**

In this process, steam is used for heat drying. Compared to electric heating, there will be 70%

energy savings, meeting the hygiene requirements of food packaging, increasing resource utilization. The qualified production rate is up to 99%.



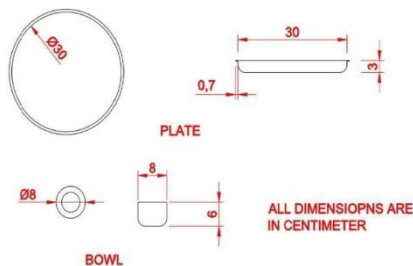
#### 4) Edge cutting and sterilization

Products extracted from the shaper will be transported to the edge cutting machine, where the excess edge will have to be trimmed. UV sterilization is applied to ensure production meets hygiene requirements.

#### 5) Packaging

The final product is packed and stored.

#### 4. Dimension of Plates and Bowl



According to the convenience the nominal size of dish and bowl is as follow:

Diameter of the dish- 30cm Height of the dish- 3cm  
Diameter of the bowl- 8cm Height of the bowl- 6cm

#### 5. Conclusion and Discussion

Disposable cutlery made from biodegradable materials is predicted to meet surplus demand in the coming years. This thing will increase the global demand for eco- friendly beverages. In the global market for biodegradable cutlery

projects by the end of the year 2026, more than the US \$ 21.2 disposable cutlery will be sold globally.

In India, thermocol 1 rs/ piece plastic 2 rs/ piece paper 3 rs/ piece bagasse 6 rs/ piece rice husk 8 rs/ piece

As the price increases, the environmental impact also gets cured.

According to the CAGR, global sales of disposable cups are expected to grow steadily at 5.1%, generating revenue from sales of 850bn units.

Today, the market is growing rapidly. It is necessary to adapt to the change. The use of hazardous plastic as a cutlery medium should be avoided completely. Production Of plates and bowls from sugarcane bagasse can help to heal the environmental crises.

Nowadays the crockery sets which costs 2000 + Rs and are little expensive also not affordable for small street food shops.

And as alternative to this they use plastic plates, cup, spoons which cost 200+ Rs or paper plates 50 to 100 Rs which are economic but not safe for human health, according to the study of IIT Kharagpur which states that the use of plastic and paper cups leads to hazard.

As our product is made from bagasse its price for a set which contains 6 pieces is near about 30 to 40 Rs. Which is economical as well as safe for human life.

#### Reference

- <https://www.thebetterindia.com/63696/biodegradable-tableware-sugarcane-fibre/>
- [www.entrepreneur.com](http://www.entrepreneur.com)
- [https://www.huffingtonpost.in/the-better-india/these-eco-friendly-containers-made-of-sugarcane-are-stronger-ha\\_a\\_21644451/](https://www.huffingtonpost.in/the-better-india/these-eco-friendly-containers-made-of-sugarcane-are-stronger-ha_a_21644451/)
- [https://www.researchgate.net/profile/Mohamed\\_Gadallah2/post/Green\\_packaging\\_for\\_food\\_products\\_does\\_anybody\\_know\\_any\\_companies\\_or\\_research\\_teams\\_exclusively\\_working\\_on\\_this/attachment/59d650f179197b80779a9a3e/AS%3A505479508250624%401497527114553/download/Biodegradable-packaging-for-food-products.pdf](https://www.researchgate.net/profile/Mohamed_Gadallah2/post/Green_packaging_for_food_products_does_anybody_know_any_companies_or_research_teams_exclusively_working_on_this/attachment/59d650f179197b80779a9a3e/AS%3A505479508250624%401497527114553/download/Biodegradable-packaging-for-food-products.pdf)
- <https://transitions2earth.com/blogs/news/from-sugarcane-to-sustainable-serve-ware>
- [https://www.researchgate.net/publication/282718051\\_Effect\\_of\\_Heat\\_Compression\\_on\\_the\\_Tensile\\_Strength\\_of\\_PALFSugarcane\\_Bagasse\\_for\\_Disposable\\_Plate](https://www.researchgate.net/publication/282718051_Effect_of_Heat_Compression_on_the_Tensile_Strength_of_PALFSugarcane_Bagasse_for_Disposable_Plate)
- <https://youtu.be/pxSZiG0Bjcs>
- <https://www.greenweimo.com/how-to-produce-sugarcane-bagasse-food-container>
- <https://youtu.be/ydO84ilqu2s>
- <https://youtu.be/MH-tBhbCPWA>
- <https://youtu.be/B3aq2KMH2z8>
- [https://www.researchgate.net/profile/Priscilla\\_Sales2/publication/319655245\\_Perspectives\\_on\\_the\\_production\\_structural\\_characteristics\\_and\\_potential\\_applications\\_of\\_bioplastics\\_derived\\_from\\_polyhydroxyalkanoates/links/5b02e4ff0f7e9b9e94bdaa634/Perspectives-on-the-production-structural-](https://www.researchgate.net/profile/Priscilla_Sales2/publication/319655245_Perspectives_on_the_production_structural_characteristics_and_potential_applications_of_bioplastics_derived_from_polyhydroxyalkanoates/links/5b02e4ff0f7e9b9e94bdaa634/Perspectives-on-the-production-structural-)

- characteristics-and-potential-applications-of-bioplastics-derived-from-polyhydroxyalkanoates.pdf
13. <https://www.sciencedirect.com/science/article/pii/S1359836813005866>
  14. <https://youtu.be/pxSZiG0Bjcs>
  15. <https://www.greenweimo.com/how-to-produce-sugarcane-bagasse-food-container>
  16. <https://youtu.be/ydO84ilqu2s>
  17. <https://youtu.be/MH-tBhbCPWA>
  18. <https://youtu.be/B3aq2KMH2z8>
  19. [https://www.researchgate.net/profile/Priscilla\\_Sales2/publication/319655245\\_Perspectives\\_on\\_the\\_production\\_structural\\_characteristics\\_and\\_potential\\_applications\\_of\\_bioplastics\\_derived\\_from\\_polyhydroxyalkanoates/links/5b02e4ff0f7e9be94bdaa634/Perspectives-on-the-production-structural-characteristics-and-potential-applications-of-bioplastics-derived-from-polyhydroxyalkanoates.pdf](https://www.researchgate.net/profile/Priscilla_Sales2/publication/319655245_Perspectives_on_the_production_structural_characteristics_and_potential_applications_of_bioplastics_derived_from_polyhydroxyalkanoates/links/5b02e4ff0f7e9be94bdaa634/Perspectives-on-the-production-structural-characteristics-and-potential-applications-of-bioplastics-derived-from-polyhydroxyalkanoates.pdf)
  20. [\\_on\\_the\\_production\\_structural\\_characteristics\\_and\\_potential\\_applications\\_of\\_bioplastics\\_derived\\_from\\_polyhydroxyalkanoates/links/5b02e4ff0f7e9be94bdaa634/Perspectives-on-the-production-structural-characteristics-and-potential-applications-of-bioplastics-derived-from-polyhydroxyalkanoates.pdf](https://www.researchgate.net/profile/Priscilla_Sales2/publication/319655245_Perspectives_on_the_production_structural_characteristics_and_potential_applications_of_bioplastics_derived_from_polyhydroxyalkanoates/links/5b02e4ff0f7e9be94bdaa634/Perspectives-on-the-production-structural-characteristics-and-potential-applications-of-bioplastics-derived-from-polyhydroxyalkanoates.pdf)



## EFFECT OF NA-GLASS DISPERSION ON IONIC AND ELECTRONIC TRANSFERENCE IN $\text{Ag}_2\text{SO}_4$

J.B.Randhawa<sup>1</sup> and P.W.Ambekar<sup>2</sup>

<sup>1</sup>Government College of Engineering, Nagpur (India) 441108.

<sup>2</sup>Dharampeth M P Deo Memorial Science College, Nagpur (India)  
pacific0701@gmail.com

### ABSTRACT

*In the present study composite electrolytes of  $\text{Ag}_2\text{SO}_4$  were prepared by dispersing high  $T_g$  Na-glass in different compositions. Formation of glass and composite was confirmed by powder X-ray diffraction study. Ionic and electronic conductivity measurements were carried out using Complex Impedance Spectroscopy and Wagner's dc polarization technique respectively. Nyquist plot reveals two different conduction mechanisms in the composite  $\text{Ag}_2\text{SO}_4$ +glass for all composition. Two orders of enhancement in ionic conductivity were observed at lower temperatures. The phase transition temperature of  $\text{Ag}_2\text{SO}_4$  is found shifting to lower temperature side on increasing dispersoid concentration. DC conductivity study revealed that for pure  $\text{Ag}_2\text{SO}_4$ ,  $\sigma_{ion} > \sigma_{ele}$  and the electronic conduction is via both electrons and electron-holes, in agreement with earlier reported data. Electron-hole transference number is found more than the electron transference number indicating domination of p-type conductivity in pure phase. On the contrary  $\text{Ag}_2\text{SO}_4$ +glass composite showed n-type electronic conductivity. For a  $\text{SO}_2$  gas sensor with cell configuration: Ar,  $\text{O}_2$ ,  $\text{SO}_2$ , Pt/ $\text{Ag}_2\text{SO}_4$ /Ag(sealed); at high silver potential, silver ions are incorporated into the lattice of electrolyte and for neutrality reasons, the concentration of excess of electrons ( $e'$ ) in solid is increased. Performance of a typical  $\text{SO}_2$  gas sensor is discussed in light of above conductivity results.*

**Keywords:** Composite, Electrochemical Gas Sensor, Electronic Conductivity, Solid Electrolyte, Wagner's DC polarization technique

### 1. Introduction

With the advancement of nanotechnology major thrust is being given on development of solid-state gas sensors (semiconductor type) for their fast response and miniaturized dimensions. Yet a reliable  $\text{SO}_2$  gas sensor with high selectivity is to be developed (Beatty et al, 2014; Hunter et al, 2020). Electrochemical gas sensors overcome the major disadvantages associated with solid state sensors, as they are highly selective and follows a theoretical relation which obviates the need of calibration. In the present study effect of electronic conductivity of the electrolyte on performance of an electrochemical  $\text{SO}_2$  gas sensor is studied.

The electrochemical devices viz., batteries, fuel cells, sensors, super-capacitors etc. use solid electrolyte as a prime component. The electrolyte should possess fast ionic transference with negligibly small electronic conductivity. Enhancement in ionic conductivity of solid electrolyte is obtained either by iso/aliovalent doping, making solid solution or composites. The first crystal-crystal composite solid electrolyte has been obtained with sub-micron size alumina particles dispersed in Lithium Iodide matrix, exhibiting

50 times higher Li-ion conductivity at room temperature in relation to the host (Liang, 1973). Since then, a large number of composite solid electrolyte have been reported by dispersion of insulating phase e.g.  $\alpha, \beta, \gamma$ - $\text{Al}_2\text{O}_3$ ,  $\text{SiO}_2$ ,  $\alpha$ - $\text{Fe}_2\text{O}_3$ ,  $\text{MgO}$ , Fly-ash,  $\text{ZrO}_2$  into pure solid ionic conductor viz.  $\text{LiBr}$ ,  $\text{LiCl}$ ,  $\text{CuCl}$ ,  $\text{AgI}$ ,  $\text{HgI}_2$ ,  $\text{CaF}_2$ ,  $\text{AgCl}$ ,  $\text{Li}_2\text{SO}_4$ ,  $\text{Ag}_2\text{SO}_4$ ,  $\text{Na}_2\text{CO}_3$ , glasses etc. Composites are preferred for device applications due to their inherently advantageous characteristic properties such as high ionic conductivity at relatively low temperatures, homogeneity in electrical and mechanical properties, better interface with electrode/s, enhanced electrode kinetics and stable thermal properties.

$\text{Ag}_2\text{SO}_4$  is an apt candidate for electrolyte/test electrode application in an electrochemical  $\text{SO}_2$  gas sensor due to various advantages viz. high ionic conductivity with low activation enthalpy, non-hygroscopic nature, coexistence of Ag- $\text{Ag}_2\text{SO}_4$  as an equilibrium phase, better sinter ability etc. (Singh and Bhoga, 1999). The major disadvantage associated with pure phase sulfate-based electrolyte system is its very poor mechanical strength, porosity and instability over thermal cycling. The  $\text{SO}_2$  sensors have Ag+ $\text{Ag}_2\text{SO}_4$  as reference electrode. This reference electrode needs

sealing from the test gas. Pure  $\text{Ag}_2\text{SO}_4$  or its heterogeneous composite electrolyte failed to give proper sealing because of large difference in thermal expansion coefficient of reference electrode and that of the electrolytes. In order to overcome these limitations glass bonded  $\text{Ag}_2\text{SO}_4$  electrolytes with different compositions were prepared.

In the present study glass dispersed composite electrolytes was prepared by dispersing high  $t_g$  Na-glass ( $\text{Na}_2\text{O}+2\text{B}_2\text{O}_3+7\text{SiO}_2$ ) into  $\text{Ag}_2\text{SO}_4$  in different compositions. Looking at the necessity of high operating temperature of  $\text{SO}_2$  gas sensor, a non-conducting glass with high glass transition temperature ( $>550^\circ\text{C}$ ) was selected for dispersion. Formation of glass as well as composite was confirmed by powder x-ray diffraction study. Electrical characterization i.e. ionic and electronic conductivity measurements were carried out using complex impedance spectroscopy and Wagner's DC polarization technique respectively.

## 2. Experimental

### 2.1 Preparation of Glass

$\text{Na}^+$ -glass of composition  $10\text{Na}_2\text{O}:20\text{B}_2\text{O}_3:70\text{SiO}_2$  were prepared by rapid melt quenching. Well-dried initial ingredients  $\text{Na}_2\text{CO}_3$ ,  $\text{H}_2\text{BO}_3$  and  $\text{SiO}_2$  having purity  $> 99.98\%$  were taken in an appropriate mole ratio. Mixed under acetone for an hour and then subjected to calcification in a porcelain crucible above the decomposition temperature of  $\text{Na}_2\text{CO}_3$  ( $900^\circ\text{C}$ ) for converting into  $\text{Na}_2\text{O}$  and  $\text{CO}_2$  gas (evolved). The temperature of the mixture was then raised to its melting, and the melt was soaked for an hour at the melting temperature ( $1100^\circ\text{C}$ ) for homogenization. The melt was quenched to room temperature between two flat surfaced Aluminum blocks. The quenching rate offered by the Aluminum blocks was  $100^\circ\text{C}/\text{s}$  (Singh and Ratnam, 1988). The glass formed was found to be transparent. These glass flakes were crushed and sieved to get fine powder ( $<40\mu\text{m}$ ) for dispersion into  $\text{Ag}_2\text{SO}_4$ .

### 2.2 Glass Dispersed Composite

Fine powder of  $\text{Na}^+$  glass was mixed with well-dried  $\text{Ag}_2\text{SO}_4$  in the composition  $(100-x)\text{Ag}_2\text{SO}_4:(x)\text{glass}$ , (where  $x = 0, 5, 10, 15$  & 20

weight %). The compositions were mixed manually under acetone for an hour. The dried materials were then palletized ( $D = 9\text{mm}$  and  $t = 1-2\text{mm}$ ) and kept in a programmable furnace. The temperature of the furnace was raised to  $550^\circ\text{C}$  and kept at this temperature for 2 hr followed by slow cooling (furnace cooling) to room temperature. Very sturdy and compact pellets of the composite were obtained without change in the color or form. This compactness was expected to result because of lowering of glass softening temperature due to palletization. The melted/soften glass helps in filling the pores between the grains of pure sulfate phase as well as tries to glue them together.

### 2.3 Impedance measurement

Glass dispersed composites was palletized in the form of circular discs of dimensions approximately 9 mm in diameter and 1-2 mm in thickness by pressing uniaxially at pressure  $4\text{ tons}/\text{cm}^2$  using stainless steel die-punch and hydraulic press (Specac UK). Later, the pellets were sintered at 773K for 6 hours. A thin film of Silver was painted on both the flat surfaces of pellet to ensure good ohmic contacts. Six samples were loaded simultaneously between silver electrodes of specially designed sample holder. The computer-automated system was used for multi-channel complex impedance measurement using Impedance analyzer (HP 4192A).

### 2.4 Electronic and ionic transport measurement

Transport number measurement of  $\text{Ag}_2\text{SO}_4$  and  $\text{Ag}_2\text{SO}_4+\text{glass}$  was carried out at 723K. This temperature was selected because it is well above the transition temperature (690K) of  $\text{Ag}_2\text{SO}_4$  from  $\beta$  to  $\alpha$  phase. The  $\text{SO}_2$  gas sensors are operated at temperature above 773K.

The sample was placed between the two pressurized gold lids sample holder. The cell configuration for transport number measurement in ambient gas atmosphere is given as

$\text{Ag}, \text{O}_2, \text{Ar} (-)/ \text{Ag}_2\text{SO}_4 / (+) \text{Ar}, \text{O}_2, \text{Pt}$

The schematic of experimental set-up used for measurement is shown in figure (1). The sample while mounted in a sample holder was

heated up to 725K and maintained at this temperature for entire measurement of transport number using Eurotherm temperature controller ( $\pm 1^\circ\text{C}$ ). After attaining thermal equilibrium, a d.c. potential was applied with the help of source and measure instrument (Keithley SMU236) and recorded

simultaneously the current through sample as a parametric function of time. The data was stored by interfacing the instrument to IBM PC through indigenously developed software. The sample was allowed to get polarize by maintaining the identical temperature and potential in ambient atmosphere.

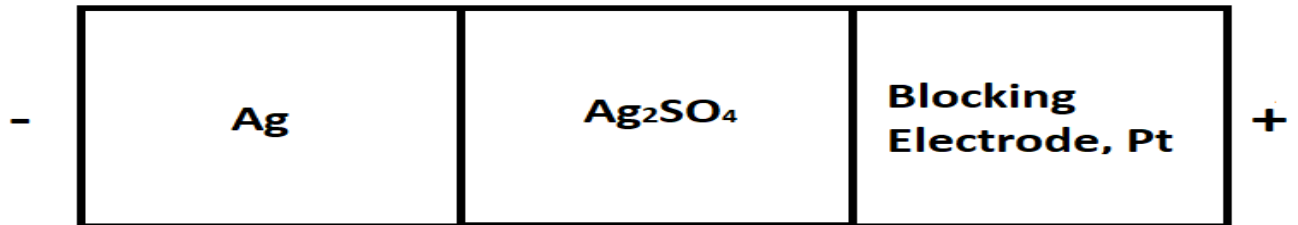


**Fig. 1: Schematic representation of DC. polarization cell. The reversible electrode Ag exchanges both cations  $\text{Ag}^+$  and electrons.**

### 3. Results and Discussion

The x-ray powder diffraction pattern for  $10\text{Na}_2\text{O}+20\text{B}_2\text{O}_3+70\text{SiO}_2$  glass is shown in figure (2). A broad diffused scattering over several degrees suggests lack of regular crystalline structure hereby confirming its amorphous nature. The x-ray powder

diffraction pattern of  $\text{Ag}_2\text{SO}_4$  dispersed with glass of above composition is shown in figure (3). All the major peaks correspond to  $\text{Ag}_2\text{SO}_4$ . No other major crystalline phase was observed that would have resulted on reaction of  $\text{Ag}_2\text{SO}_4$  with glass

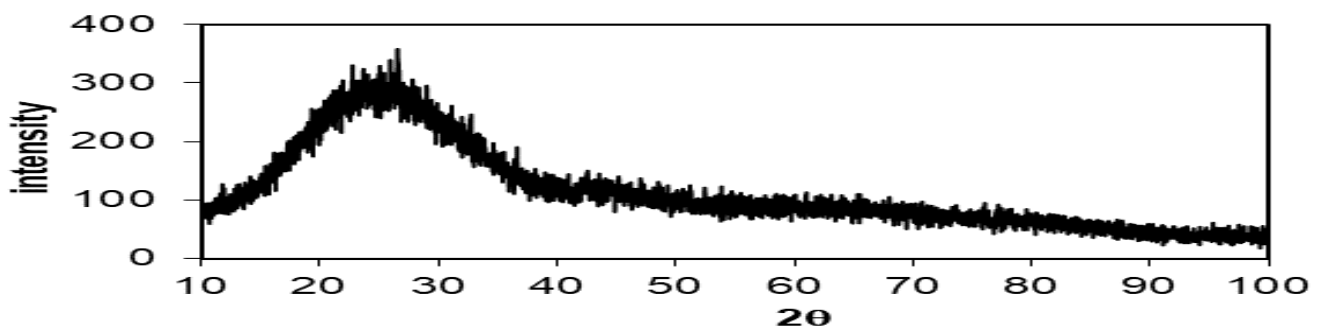


**Fig. (2): Powder XRD pattern for  $\text{Na}_2\text{O}+2\text{B}_2\text{O}_3+7\text{SiO}_2$  glass.**

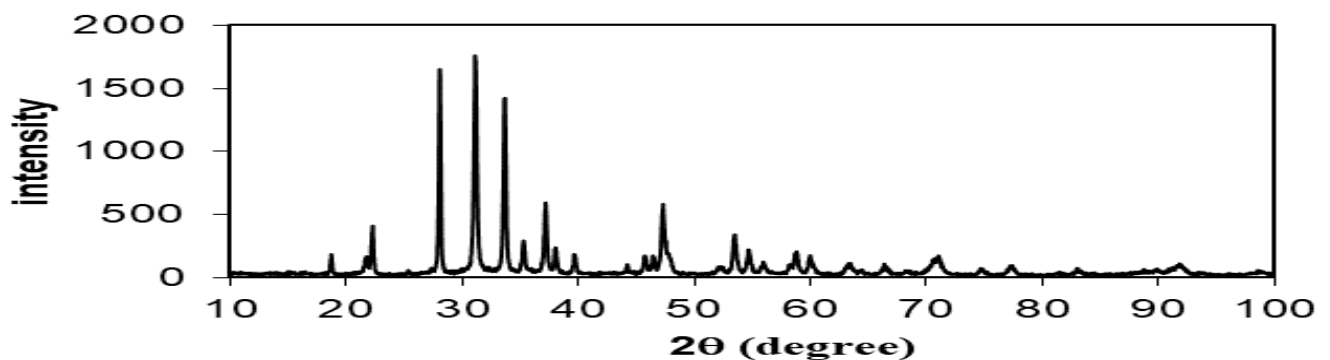


**Fig. (3): Powder XRD pattern for  $\text{Na}_2\text{O}+2\text{B}_2\text{O}_3+7\text{SiO}_2$  glass dispersed  $\text{Ag}_2\text{SO}_4$ .**

Typical impedance curves for the composite  $0.8\text{Ag}_2\text{SO}_4+0.2(10\text{Na}_2\text{O}+20\text{B}_2\text{O}_3+70\text{SiO}_2)$  of composition at two different temperatures is shown in figure (4), revealing the presence of two overlapping depressed semicircular arcs suggesting two different conduction regimes within the material. Two major pathways taking part in the conduction are  $\text{Ag}_2\text{SO}_4/\text{glass}$  interface and the bulk of  $\text{Ag}_2\text{SO}_4$  grains (Singh,

1993). The surface interaction at  $\text{Ag}_2\text{SO}_4/\text{glass}$ -heterojunction is described analogous to one at the moderately ion conductor/insulator interface giving rise to a space charge layer (Maier, 1985). The type of interface interaction could not be revealed here because of limited frequency range of measurement, which restricted formation of high frequency semicircle at higher temperatures

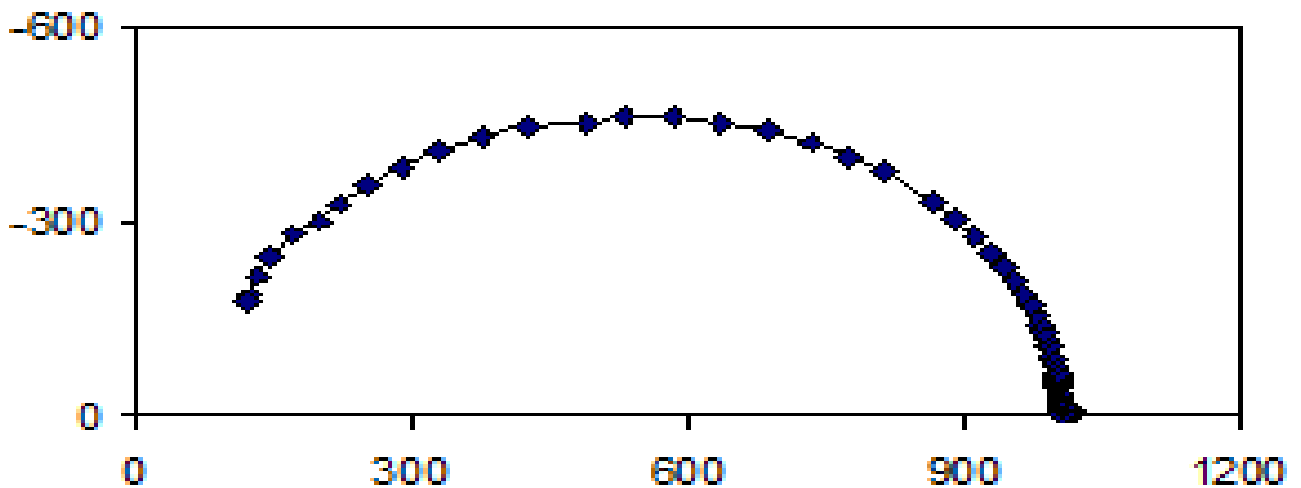
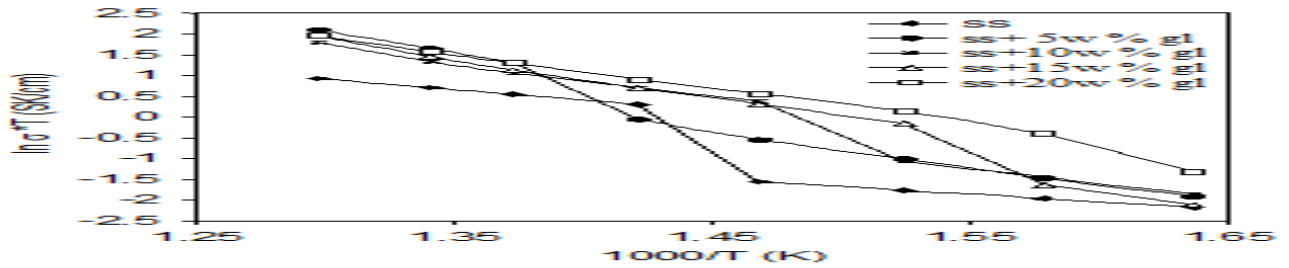


Fig. 4 (a & b): Complex impedance plots for  $0.8\text{Ag}_2\text{SO}_4+0.2\text{glass}$  at 660 and 610K.

The total resultant conductivity was determined from the real axis intercept of the complex impedance plot. Figure (5) shows that conductivity of  $\text{Ag}_2\text{SO}_4$  and its glass-dispersed composite obey the Arrhenius law over the entire temperature range of investigation. Large conductivity enhancement is observed due to glass dispersion over complete range of temperature with more predominance at lower temperature. The magnitude of conductivity at higher temperatures is same as that of the pure  $\text{Ag}_2\text{SO}_4$ . The phase transition temperature of  $\text{Ag}_2\text{SO}_4$  from orthorhombic  $\beta$ -phase to hexagonal  $\alpha$ -phase is affected by the dispersoids addition. This is a typical of heterogeneous composite electrolytes (Chowdhari, Tare and Wagner, 1985). For most of the composites it has been observed that a hysteresis in Arrhenius plot is seen on taking the conductivity measurement while heating and cooling the sample (Shahi and

Wagner Jr., 1981; Chowdhari, Tare and Wagner Jr., 1985). The transition temperature has been found unaffected while conductivity is measured on heating but found decreasing while cooling the sample. The decrease in transition temperature was found proportional to the dispersoids content. This decrease in  $\alpha$  to  $\beta$  transition temperature has been explained on suggestion that the interaction of cation interstitials with the strain field associated with the volume charge is the principal factor responsible for the phase transition (Rice, Strassler and Toombs., 1974). This significant result is observed while cooling because of existence of large no of thermally generated defects. The decrease in transition temperature  $\Delta T$  has been reported to be linearly proportional to content of second phase. Similar results were obtained in the present study.



**Fig. 5:** Arrhenius plots for  $Ag_2SO_4$  +glass composite electrolyte of the compositions mentioned. ss:  $Ag_2SO_4$ , gl: glass

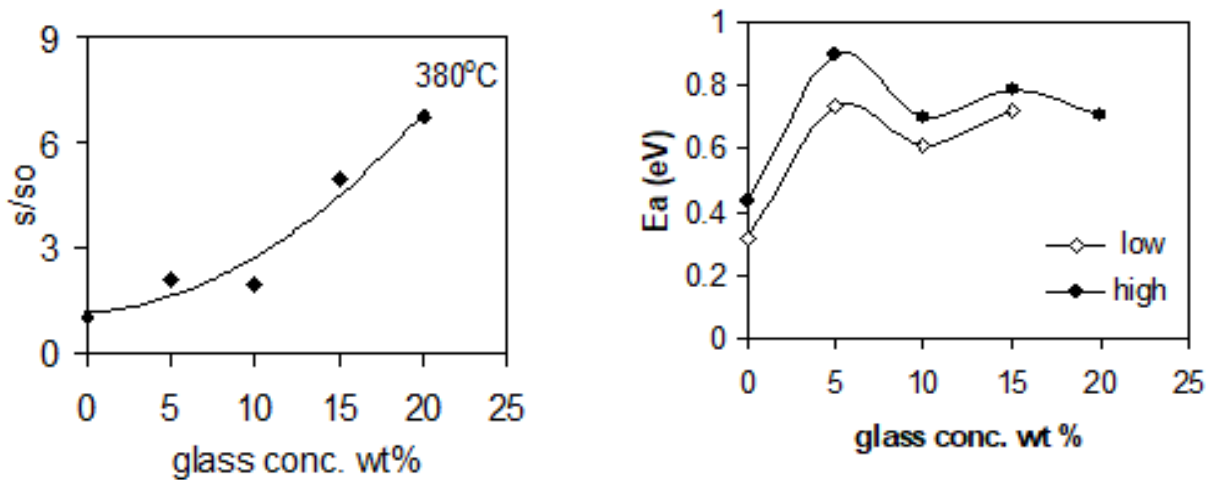


**Fig. (6a):** Conductivity enhancement as a function of glass concentration (6b): Variation in activation energy  $E_a$  with glass concentration.

The variation of conductivity enhancement  $\sigma/\sigma_0$  at  $380^\circ C$  and activation enthalpy before and after the phase transition with weight fraction of dispersoid glass is depicted in figs. (6a and b) respectively. Fig. (6a) reveals that the conductivity continuously increases with glass content instead of a sharp one as predicted from percolation theory for composite solid electrolyte (Jiang and Wagner Jr., 1995). Such conductivity behavior may be due to relatively larger surface area of interaction of dispersed phase with the host

grains, whereas, percolation threshold is obtained for fine particle (sub-micron) dispersion. Higher concentrations of glass dispersion were not tested because the electrolyte to be developed was required to be necessarily of  $Ag_2SO_4$  in  $SO_x$  gas sensors. As  $Ag+Ag_2SO_4$  reference electrode gives thermodynamic stability as well as complete reversibility with  $Ag_2SO_4$  electrolyte. Increased glass content in the electrolyte is likely to disturb this equilibrium.

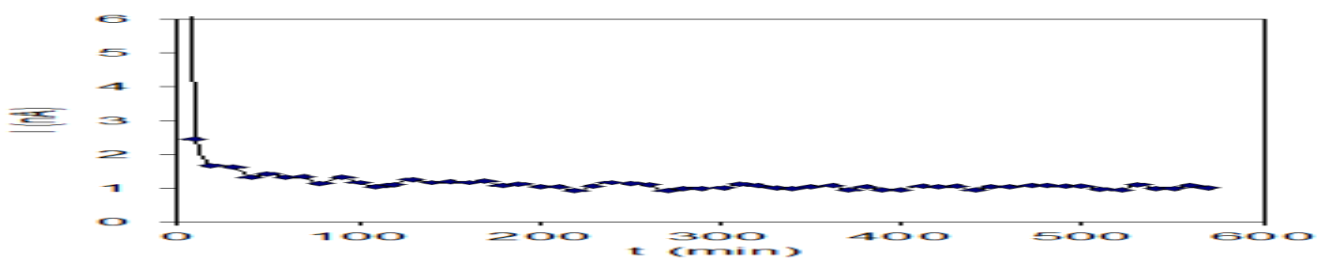


**Fig.7:** Polarization curve for  $Ag_2SO_4$  at polarizing potential of 0.22V at 723K.

Typical time variation of polarizing current on application of a small DC potential is shown in figure (7). The initial large current is due to motion of ions as well as electrons while a constant current was observed after polarization of ions, and this conductivity is due to electronic charge carriers alone. The equilibrium value of this steady current was obtained by taking average of last steady state observations as shown in the inset. In order to get the preliminary ideal of the potentials required for polarization the voltage was applied in larger steps and general trend of the voltage-current characteristic for pure  $Ag_2SO_4$  was obtained as shown in figure (8a). Later the same set of observations was repeated for another  $Ag_2SO_4$  pellet with smaller variation in polarizing potential. The so obtained V-I characteristic is shown in figure (8b). This typical nature of the  $\log I$  vs polarizing potential  $E$  curve shows that  $\sigma_{ion} > \sigma_{ele}$  and both electron  $\sigma_e$  as well as hole  $\sigma_h$  conductivity is dominating in the sample (Wagner, 1956). The magnitude of  $\sigma_e$  was obtained from the constant current plateau at

the potential ( $E = 0.32V$ ) where sudden increase in current starts for the second set observations (Kopp et al, 1993; Poulsen et al, 1983). Also, the magnitude of hole conductivity  $\sigma_h$  was calculated from the slope of the curve wherein current increases exponentially with applied potential. The values of electron and hole conductivities were found to be  $\sigma_e = 1.0059 \times 10^{-7}$  S/cm and  $\sigma_h = 8.38998 \times 10^{-9}$  S/cm respectively. From these conductivities as well as taking total conductivity from ac measurements the hole and electronic transport numbers were calculated as  $t_h = 1.95 \times 10^{-4}$  and  $t_e = 5.54 \times 10^{-6}$ . The current voltage behavior for the composite electrolyte with following cell configuration: (+)Ar, O<sub>2</sub>, Pt/Ag<sub>2</sub>SO<sub>4</sub>+glass/Ag, O<sub>2</sub>, Ar (-) at 723K is shown in fig (9). The magnitude of electronic conductivity was calculated from the plateau current as  $\sigma_e = 1.10797 \times 10^{-6}$  S/cm and the corresponding transport number  $t_e = 7.3128 \times 10^{-4}$ . Thus, the preliminary observation shows that the Ag<sub>2</sub>SO<sub>4</sub>+glass composite has very small n-type electronic conductivity.

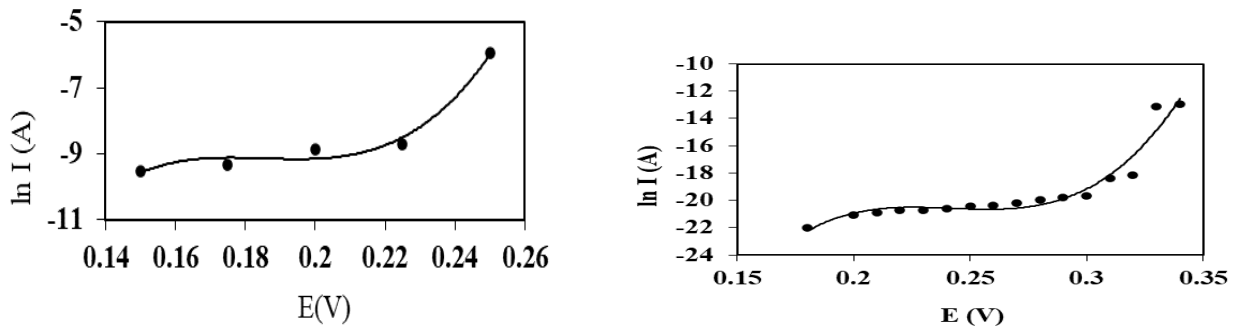


Fig. 8: Current voltage curve of pure  $Ag_2SO_4$  for different sample thickness at 723K

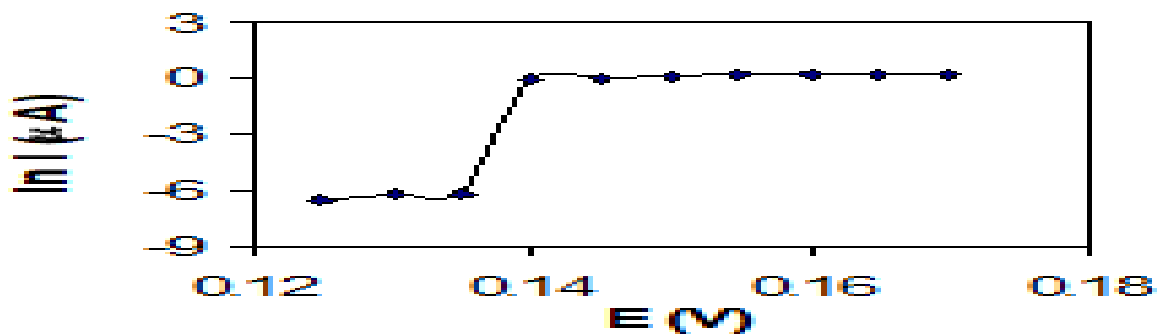


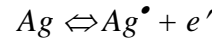
Fig.9: Current voltage behavior of  $Ag_2SO_4$  +glass composite at 723K in ambient atmosphere.

The earlier reported measurement of transport number for pure  $Ag_2SO_4$  (prepared by chemical reaction of  $AgNO_3$  with  $H_2SO_4$ ) at 719K where smaller polarizing emfs (0.04 to 0.14V) have been applied across the pellet of thickness 3mm and dia. 8mm with Ag and Pt as reversible and blocking electrodes respectively (Hauffe and Hoeffgen, 1966). The magnitude of hole transport number calculated using slope of the graph in the linear portion has been reported to be  $t_{\oplus} = 1 \times 10^{-4}$  showing predominance of hole conductivity which is in agreement with our observations.

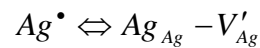
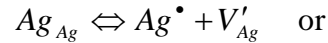
Both p and n-type electronic conductivity was found present in pure  $Ag_2SO_4$  with domination p-type conduction which is in agreement with the earlier reports. The type of electronic conductivity was found changing from p-type to n-type on dispersion of glass. This result for  $Ag_2SO_4$ +glass composite is in contrast with other reported composites. Wagner-Hebb polarization of  $LiI:Al_2O_3$  (Liang, Joshi and Hamilton, 1978; Poulsen et al, 1983),  $AgI:Al_2O_3$  (Shahi and Wagner Jr., 1981),  $AgCl:Al_2O_3$  (Maier, 1995) indicate an increase in the p-type conduction with respect to pure material. The effect is very weak in  $CuCl:Al_2O_3$  but the tendency is analogous (Jow and Wagner Jr, 1979).

In electrochemical devices, the electronic charge carriers (electrons/holes) in the electrolyte affect the device performance significantly when operated under open circuit conditions, e.g. an electrochemical sensor in potentiometric mode. The variation in electronic charge carriers under different operating conditions has been explained on the basis of charge neutrality (Nafe, 1994). At high silver potential, silver is incorporated into the lattice of the electrolyte, and hence the concentration of excess of electrons ( $e'$ ) in the solid is increased. This charge balance is totally independent of the exact nature of the defects involved in the incorporation process.

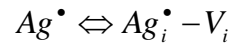
Detailed information about the defects can be abstracted by simply regarding the building unit  $Ag^{\bullet}$ , which characterizes a silver ion dissolved in the solid:



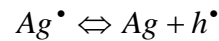
$Ag^{\bullet}$  can be a combination of the structure elements  $Ag_{Ag}$  (regular silver site) and  $V'_{Ag}$  (silver vacancy)



or a combination of  $Ag_i^{\bullet}$  (silver interstitial) and  $V_i$  (interstitial vacancy)



Similarly at low silver activity, silver is released from the solid. As a result, electron holes ( $h^{\bullet}$ ) are formed whatever the involved atomic defects are:



The motivation behind taking up the above transference number studies of the  $Ag_2SO_4$  and  $Ag_2SO_4$ +glass electrolyte is to investigate reason behind the significant deviation observed in sensor emf from Nernst's law in the  $SO_2$  gas concentration range from 600 ppm to 13%, despite showing sensitivity close to the theoretical value. Variation in sensor emf for the cell

*Ar, O<sub>2</sub>, SO<sub>2</sub>, Pt / Ag<sub>2</sub>SO<sub>4</sub> / Ag sealed*

with different test gas concentration at 773K is shown in figure (10). The cell emf of this sensor is governed by the relation

$$E = \frac{-\Delta G^{\circ}(T)}{2F} + \frac{RT}{2F} \ln \frac{P_{SO_2} P_{O_2}^{1/2}}{a_{Ag_2SO_4}}$$

(1)The magnitude of sensitivity was obtained from the slope of the straight line as 0.028V which is close to the theoretical sensitivity value 0.033V at 773K in the lower test gas partial pressure region (250ppm to 7.8%)

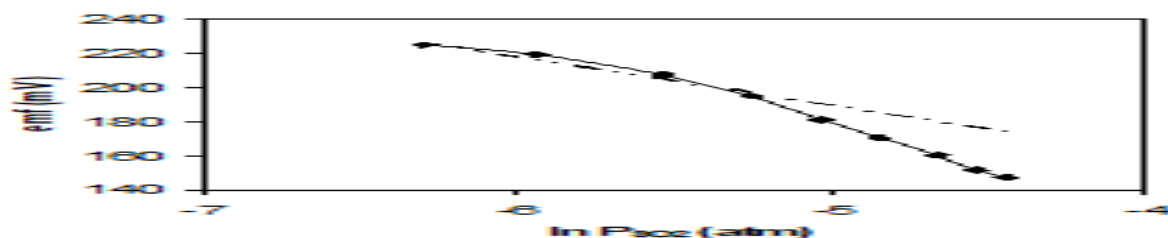
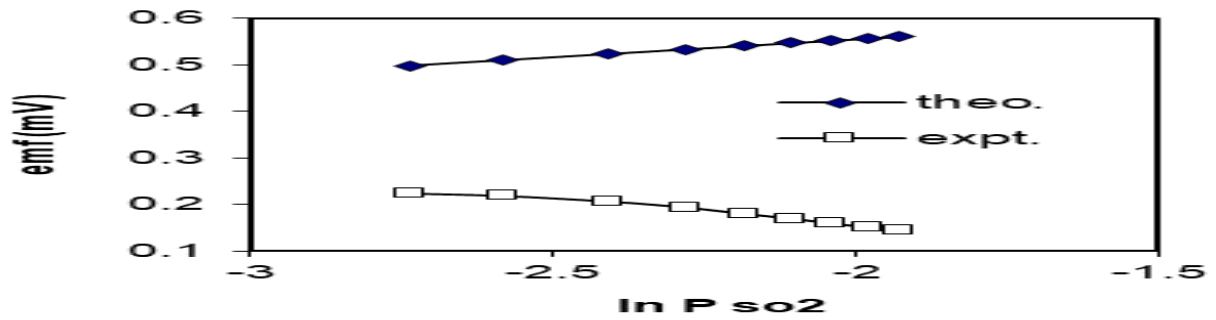


Fig. 10: Variation in sensor emf of cell with  $SO_2$  partial pressure at 773K



**Fig.11: Comparison of sensor emf with theoretically calculated value for the cell at 773K**

The theoretical value of sensor emf for above cell configurations calculated using theoretical data (Barin, 1993) for Gibb's free energy of  $\text{Ag}_2\text{SO}_4$  at 773K and taking  $a_{\text{Ag}_2\text{SO}_4}$  equal to unity in the  $\text{Ag}+\text{Ag}_2\text{SO}_4$ . This emf is shown against the experimentally obtained response in figure (11), depicting significant deviation from Nernst law.

#### 4. Conclusion

Two orders of magnitude enhancement in conductivity of  $\text{Ag}_2\text{SO}_4$  is obtained when a composite is formed by dispersion of Na glass into it. The type and magnitudes of electronic transference number of pure  $\text{Ag}_2\text{SO}_4$  was found in close agreement with the previous reported values. In the composite,  $\text{Ag}_2\text{SO}_4 + \text{glass}$ , n-

type conduction is found dominant for the applied voltages up to 0.17V. Wagner's dc polarization study supports mechanism of defects creation at grain boundary interface. The large deviation in the magnitude of sensor emf could not be due to electronic conductivity of the electrolyte as the electronic transport number  $t_e$  for  $\text{Ag}_2\text{SO}_4+\text{glass}$  electrolyte was obtained of the order of  $10^{-4}$  as seen from Wagner's polarization results for this electrolyte.

#### 5. Acknowledgements

Authors are thankful to Department of Physics, RTM Nagpur University for providing experimental facilities.

#### References

1. Barin Ihsan, (1993). Thermodynamical Data of Pure Substances, VCH, Stuttgart.
2. Beatty B., Braus G., Durbin L., Eickhoff J., Fiehweg B., Ray M., Ryon T., Schlomberg K. and Schmitz E. (2014). Environmental Performance Report, <https://www.nrel.gov/docs/fy15osti/64208.pdf>
3. Chowdhari P., Tare V.B. and Wagner J. B. Jr, (1985). Electrical Conduction in  $\text{AgI} - \text{Al}_2\text{O}_3$  Composites, J. Electrochem. Soc. Vol.132(1), pp. 123-124.
4. Hauffe K. and Hoeffgen D., (1966). Z. Physik Chemie, 49 94-111.
5. Hunter Gary W., Akbar Sheikh, Bhansali Shekhar, Daniele Michael, Erb Patrick D., Johnson Kevin, Liu Chung-Chiun, Miller Derek, Oralkan Omer, Hesketh Peter J., (2020). A Critical Review of Solid State Gas Sensors, J. Electrochem. Soc. Vol.167, pp. 037570.
6. Jiang S. and Wagner J. B. Jr., (1995). A theoretical model for composite electrolytes—II. Percolation model for ionic conductivity enhancement, J. Phys. Chem. Solids, vol. 56(8), pp. 1113-1124.
7. Jow T. and Wagner J. B. Jr., (1979) The effect of dispersed alumina particle on the electrical conductivity of cuprous chloride, J. Electrochem. Soc. Vol. 126, pp. 1963.
8. Kopp A., Nafe H., Weppner W., Kountouros P. and Schubert H., (1993). Science and Technology of Zirconia V, (eds.) S P S Badwal, M.J. Bannister and R.H.J. Hannink, Technomic Publishing Co. Inc. Lancaster.
9. Liang C. C., (1973). U. S. Pat. 3,713, 897.
10. Liang C.C., (1973). Conduction Characteristics of the Lithium



- Iodide-Aluminum Oxide Solid Electrolytes, J. Electrochem. Soc. vol.120, pp.1289.
11. Liang C.C., Joshi A. V. and Hamilton N. E., (1978). Solid-state storage batteries, J. Applied Electrochem. Vol. 8, pp. 445.
  12. Maier J., (1985). Space charge regions in solid two-phase systems and their conduction contribution—I. Conductance enhancement in the system ionic conductor-‘inert’ phase and application on AgCl:Al<sub>2</sub>O<sub>3</sub> and AgCl:SiO<sub>2</sub>, J. Phys. Chem. Solids vol. 46. Pp. 309.
  13. Maier J., (1995). Ionic conduction in space charge regions, Prog. Solid St. Chem., vol. 23, pp. 171-263.
  14. Nafe H., electroceramics IV, (Vol.II), R. Waser, S. Hoffmann, D. Bonnenberg and Ch. Hoffmann, (eds.), (1994). IWE, RWTH Aachen, University of Technology, Germany, 745-748.
  15. Poulsen F. W., Andersen N.H., Kindl B. and Schoonman J., (1983). Properties of LiI-Alumina composite electrolyte, Solid State Ionics, vol. 9&10, 119-122.
  16. Rice M. J., Strassler S. and Toombs G. A., (1974). Superionic Conductors: Theory of the Phase Transition to the Cation Disordered State, Phys. Rev. Lett., vol. 32, pp.596.
  17. Shahi K. and Wagner J. B. Jr., (1981). Ionic Conductivity and Thermoelectric Power of Pure and Al<sub>2</sub>O<sub>3</sub>-Dispersed AgI, J. Electrochem. Soc. Vol. 128(1), pp. 6-13.
  18. Singh K. and Bhoga S. S., (1999). SO<sub>x</sub> Solid State Gas Sensors: A review, Bulletin of Material Science, Vol. 22, pp. 71.
  19. Singh K. and Ratnam J. S., (1988). Electrical conductivity of the Li<sub>2</sub>O:B<sub>2</sub>O<sub>3</sub> system with V<sub>2</sub>O<sub>5</sub>, Solid State Ionics vol.31, pp.221.
  20. Singh K., (1993). Conductivity mechanism in Li<sub>2</sub>SO<sub>4</sub>-Ag<sub>2</sub>SO<sub>4</sub> binary system, Solid State Ionics vol.66, pp. 5.
  21. Wagner Von C, (1956). Zeitschrift Fur Elektrochemie, vol. 60, pp. 4.



**MODIFIED ROYER OSCILLATOR CIRCUIT FOR WIRELESS POWER TRANSMISSION****K. Nikhar<sup>1</sup> and S. P. Jolhe<sup>2</sup>**Government College of Engineering, Nagpur  
<sup>1</sup>nikharkiran@gmail.com, <sup>2</sup>gcoen.spj@gmail.com**ABSTRACT**

Wireless power transmission is the transfer of electrical energy from a source to an electrical device without wires. This kind of charging lowers the risk of electrical shock as the circuit would be galvanically isolated. The power transmission is achieved using inductive coupling, resonant induction, or electromagnetic wave transmission depending on the type of transmission, that is short-range, mid-range, or high range transmission. This paper discusses the wireless power transfer for the mobile charger and focuses mainly on the modified Royer oscillator used in the transmitter circuit.

**Keywords:** Coupling, Magnetic, Modified Royer Oscillator Circuit, Transmission, Wireless Power Transfer (WPT)

**1. Introduction**

In a wireless power transmission system, power is supplied to a transmitter device, which generates a time-varying electromagnetic field, and transmits power across space to a receiver device, and supplies it to load for charging purposes. Wireless power uses the same technology as wireless communication devices like radio, which involves electrical energy transmitted without connecting wires by electromagnetic fields, used in mobiles, radio and television broadcasting, and WiFi. In radio communication the aim is to transfer information, so the amount of power reaching the receiver is not an important factor, as long as the information can be received legibly. In wireless communication technologies, small-scale power reaches the receiver. On the contrary, with wireless power transfer, the amount of energy received is the important thing, so efficiency is the more dominant parameter. On these grounds, wireless power transmission is more likely to be limited by distance than wireless communication technologies.

**2. Wireless Power Techniques**

Wireless power transmission techniques are categorized as, near field and far-field. In the near field or non-radiative techniques, power is transferred over short distances by using magnetic fields between two coils, that is inductive coupling, or by electric fields between metal electrodes, that is capacitive coupling. Inductive coupling is the most

conventional method for wireless technology. In far-field or radiative techniques, power is transferred by beams of electromagnetic radiation, such as microwaves or laser beams. This one can transport energy over long distances. The technology finds its application in solar power satellites and wireless powered drone aircraft.

**Inductive Coupling**

Inductive coupling is coupling between two LC circuits where resonant frequency is the same. It works by using magnetic field induction, that is the alternating current flowing in the transmitter coil produces a varying magnetic field, which induces a voltage across the terminals of the receiver coil. The primary coil (transmitter) and secondary coil (receiver) are two separate coils without any physical links. The wireless power transmission done through inductive coupling is based on fundamental theories of Ampere's circuital law and Faraday's law of induction. The efficiency of WPT based on inductive coupling depends upon the coupling coefficient, which again depends upon the separation between the two coils. So, this is the most significant drawback of wireless energy, that it cannot be transmitted up to a distance of more than a few millimeters with reasonable efficiency. Consequently, the frequency range of transmission is limited to some dozen MHz.

The inductive coupling based WPT is a quite popular technology despite its drawback, given its simple design and safety features, and therefore is been widely used in applications

such as charging of electric toothbrushes, wireless charging of EVs, charging pad for cell phones or laptops, Splashpower recharging mat and medical implants.

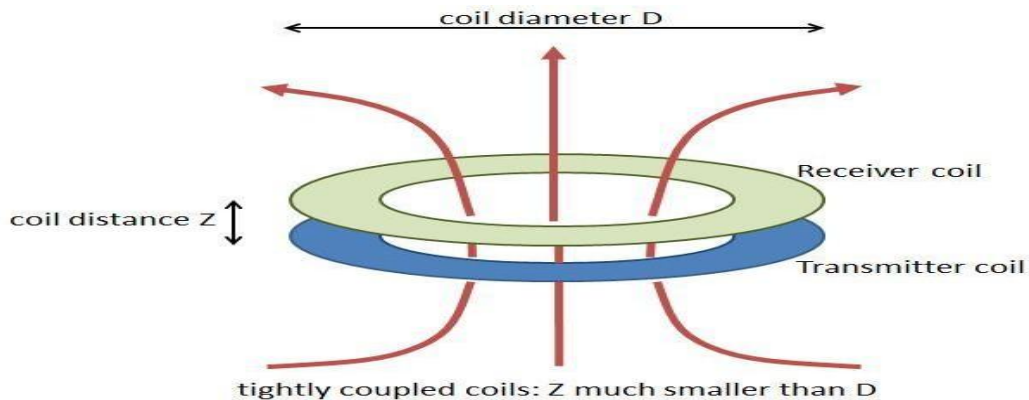


**Figure 1. Inductive Coupling Between Two Coils**

In inductive coupling, as the distance between the coils increases, power transfer gradually decreases. Maximum power transfer takes when the charging node and the power receiving node are in close contact. Proper alignment of a coil is desired for best results

### 3. Implementation

Here, Wireless Power Transmission is done through inductive coupling.

The transmitter circuit of the mobile charger using wireless power transfer consists of a dc power source, a modified Royer oscillator circuit, and a transmitter coil.

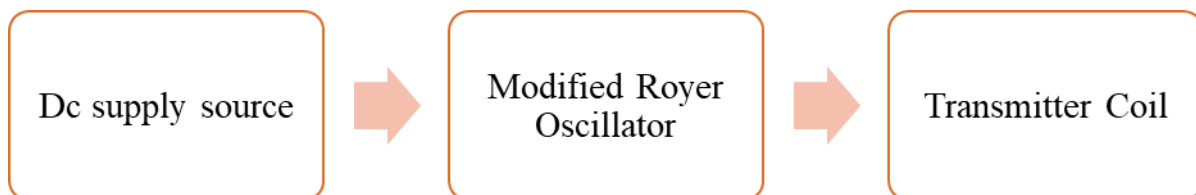


**Figure 2. Block diagram of the transmitter circuit**

#### DC Power Supply Source

The Dc power source required to be supplied to the oscillator circuit can be obtained by using a dc voltage source such as 12V or 15V batteries. Another method could be using an AC voltage source and stepping the voltage down by a 12-0-12 center tap transformer and converting the resultant ac voltage to dc by using a rectifier.

#### Oscillator Circuit

An oscillator is an electronic circuit that produces repetitive output signal waveforms, often a sine wave or a square wave. The oscillator circuit used here is that of a modified Royer oscillator, modified in the sense, change of shape of an output waveform of Royer oscillator, from square to sinusoidal waveform, by adding a capacitor.

The oscillator is used to increase the frequency

of the current supplied to the transmitter coil for reducing transmission losses. A very high value of oscillating current can be obtained depending on the values or ratings of semiconductors used in a circuit. Flux is directly proportional to the current, hence very high currents are desired for a strong magnetic field.

#### 4. Working of Modified Royer Oscillator Circuit

The circuit contains two chokes L1 and L2, two n-channel power enhancement MOSFETS Q1 and Q2, a resonating capacitor C2 (modified version), and an inductor L3, which is the transmitter coil. Diodes D1 and D2 are providing cross-coupled feedbacks. Biasing network of MOSFETS is formed by the resistors R1, R2, R3, and R4.

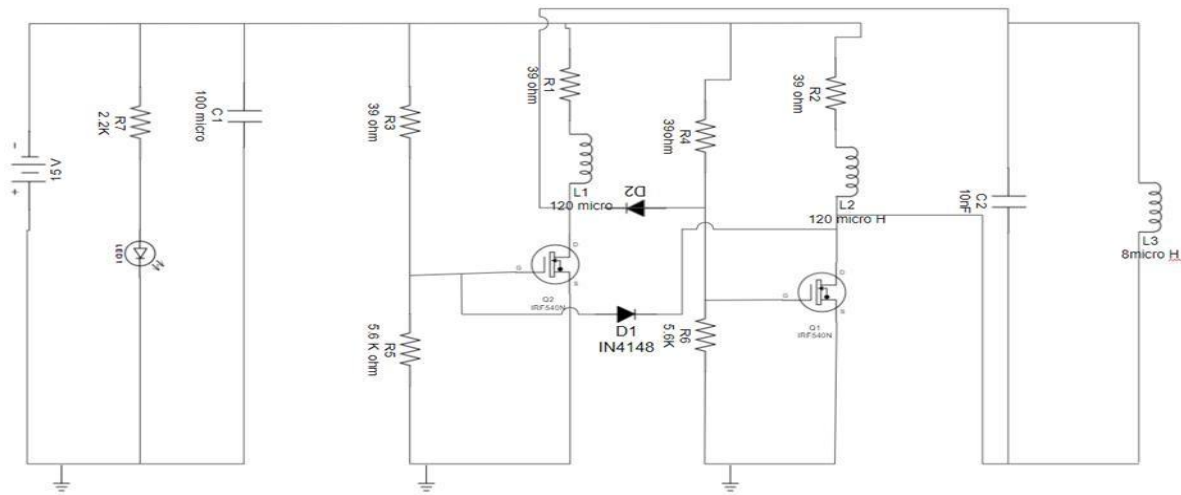


**Figure 3. Diagram of transmitter circuit**

When DC power is applied on the circuit, DC starts flowing in the choke coils and to the MOSFET's drain. As the voltage is being applied to the gate of MOSFETS, they are turned ON as soon as the gate to source voltage rises above the threshold voltage. The current keeps increasing until the coil i.e. transformer

saturates and due to the capacitor at the output, the rising and falling current pattern will form a sinusoidal output signal. The output frequency is dependent upon the inductance of coil L, capacitor C, and has a very little dependence on load on the source coil (secondary coil).

$$F = \frac{1}{2\pi\sqrt{LC}}$$

**Calculation of Oscillator Frequency**

For transmitter coil, following dimensions were used: 17swg copper wire  
 Diameter = 92mm  
 Turns = 7

Using the formula of inductance for single-layer coil,  $L = \frac{d^2 n^2}{1+0.45d}$

$L = 8.1\mu\text{H}.$   
 $F = \frac{1}{2\pi\sqrt{8.1 \times 10^{-6} \times 10 \times 10^{-9}}} = 0.56\text{MHz}.$

**5. Results**

The implemented model of wireless charger is shown below

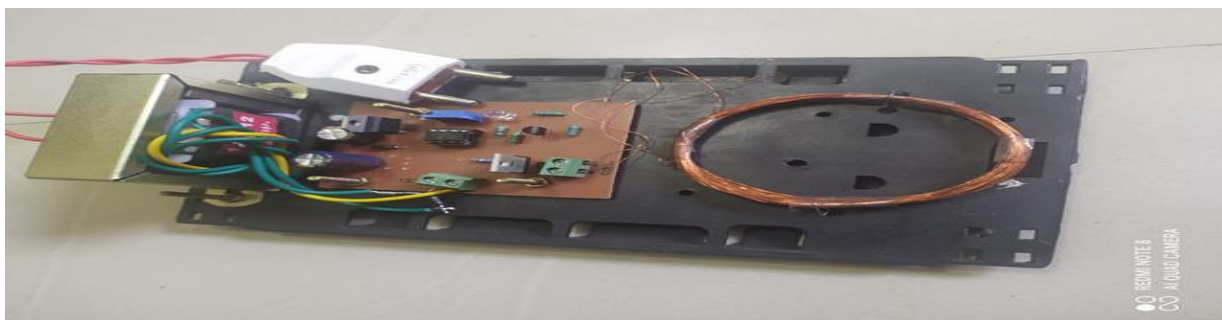


**Figure 4. Transmitter circuit**

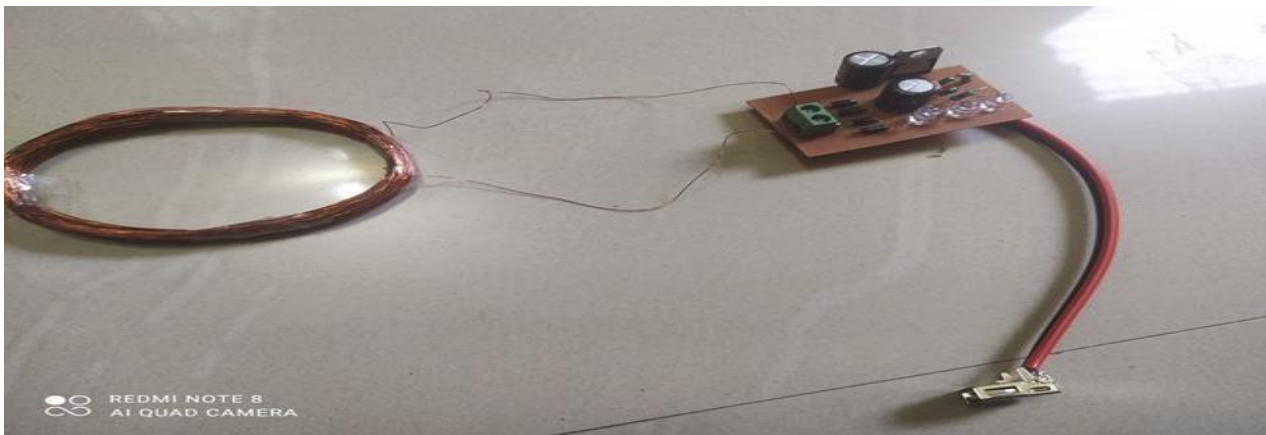


**Figure 5. Receiver circuit**

- The distance between the transmitter coil and receiver coil through which the power is transmitted wirelessly was up to 1.2 cm.
- This model is capable of charging low-power devices such as smartphones, smartwatches, and tablets.

### 6. Applications

- Wireless Power Transmission Circuits can be used to charge camera batteries, mobile phones, wireless mouse, Bluetooth headsets, etc.
- Future development in this Wireless Power Transmission technology will allow charging of car batteries, household equipment, medical devices.
- WPT is used in moving targets like fuel-free electric vehicles, fuel-free

airplanes, fuel-free rockets, and moving robots.

### Advantages

- We can charge our mobile phone anywhere with this wireless mobile charger circuit. The power could be transmitted to places to which the wired transmission is not possible.
- The cost of the distribution and transmission becomes less.
- Easy to operate and it is environmentally friendly.

### Acknowledgment

This work was supported by Assistant Professor S. P. Jolhe, Pratiksha Dhale, Santoshi Shendge, Laxmi Ulhe and is gratefully acknowledged.

### References

1. Choudhary, V., Singh, S. P., Kumar, V., & Prashar, D. (2011). Wireless power transmission: an innovative idea. *International Journal of Educational Planning & Administration*, 1(3), 203-210.
2. Ajanovic, A., & Haas, R. (2019). On the long-term prospects of power-to-gas technologies. *Wiley Interdisciplinary Reviews: Energy and Environment*, 8(1), e318.
3. Mou, X., & Sun, H. (2015, May). Wireless power transfer: Survey and roadmap. In *2015 IEEE 81st Vehicular Technology Conference (VTC Spring)* (pp. 1-5). IEEE.
4. Shidujaman, M., Samani, H., & Arif, M. (2014, May). Wireless power transmission trends. In *2014 International Conference on Informatics, Electronics & Vision (ICIEV)* (pp. 1-6). IEEE.
5. Sumi, F. H., Dutta, L., & Sarker, F. (2018). Future with wireless power transfer technology. *J Electr Electron Syst*, 7(279), 2332-0796.
6. Al-Harrasi, Z. S., AL-Rahbi, K. M., & Abdul-Halem, R. A. design and construction of wireless charging system (wcs) using inductive coupling.
7. Navapara, G. (2015). *Wireless Power Transfer*. Research Gate.
8. [http://ieeeprojectsmadurai.com/ieee%202019%20iot%20basepapers/8\\_wireless%20power%20transfer.pdf](http://ieeeprojectsmadurai.com/ieee%202019%20iot%20basepapers/8_wireless%20power%20transfer.pdf)

## EVALUATION OF WATER QUALITY PARAMETERS OF TAP WATER SAMPLES FROM JALGAON DISTRICT: A CASE STUDY

V.Agrawal,<sup>1,\*</sup> L.Ramteke<sup>2</sup> and D.D.Sarode<sup>3</sup>

Department of General Engineering, Institute of Chemical Technology, Mumbai-400019, India  
vibhagrwl071@gmail.com

### ABSTRACT

Water is very important for our health and access to safe drinking water is our basic right. Jalgaon district is one of the 35 districts of Khandesh region situated in the north western part of the Maharashtra state. Majority of towns and villages of this district suffer from potable water shortage particularly in the summer season. The physicochemical analysis of the tap water samples was carried out to determine its quality. The guidelines and acceptable limit of various parameters for the drinking water are described by the World Health Organisation and IS code 10500:2012. In the present study, several physical and chemical water quality parameters such as physical appearance, colour, odour, pH, turbidity, temperature, Total Dissolved Solids, hardness, alkalinity, calcium, magnesium, iron, chloride, sulphate and fluoride are evaluated using standard methods. In sample of some locations, the parameters such as pH, turbidity, TDS, chloride are found in permissible limits whereas in some of the samples it exceeded acceptable limit as well as permissible limit. Moreover, hardness, total alkalinity, calcium and magnesium were found above acceptable and permissible limits in most of the samples. Basically, tap water associates with a high level of hardness developed by calcium, magnesium, and other metal ions. Suitable corrective measures in the form of proper treatment will help to lead healthy life and extend the life span by avoiding the water borne diseases.

**Keywords:** Acceptable limit, Hardness, Permissible limit, Physicochemical parameters, Water quality

### 1. Introduction

Jalgaon district is one of the 35 districts located in the north western region of the Maharashtra state between 20° and 21° North latitudes and 74°55' to 76° East longitudes. It receives an average annual rainfall of 690 mm and temperature varies from 10° to 48°C (Golekar et al., 2013; Jalgaon River Linking Project-A Demand Based Project through Citizens Participation, Government of Maharashtra, 2010). The population of the district according to 2011 census is 42,24,422. Deccan trap basalt is the major rock formation covering majority of central and southern parts of the district (Vijesh, 2013). This district has total geographical area of 11765 sq.km which includes 15 talukas and 1519 villages. The 15 talukas are namely Jalgaon, Bhusawal, Yaval, Raver, Edilabad, Amalner, Chopda, Erandol, Parola, Chalisgaon, Jamner, Pachora, Bhadgaon, Dharangaon and Bodwad. In various parts of the district water levels are declining at the rate of 20 cm/ year. This district is majorly drained by river Tapi with its tributaries Bhokar, Sudki, Hadkai, Ratnawati, Aner on the left bank and Girna, Waghur, Bori, Ajani and Panzara on the right bank (Jalgaon River Linking Project-A Demand Based Project through Citizens Participation, Government of Maharashtra, 2010).

Water is a prime natural resource and basic human need. Majority of the towns and villages of Jalgaon district suffer from potable water shortage particularly in the summer season. In majority of the villages, water from borewell is supplied with minimum or practically no water treatment. Drinking water plays an important role in keep the body hydrated in all seasons. This is particularly important in regions of hot climate where people suffer due to water borne diseases. The quality of the water is vital for human consumption by any means. Thus, Bureau of Indian Standards IS 10500:2012 gives standards for drinking water, which by definition includes water supplied by any means for human consumption.

In this study, we have carried out the field investigation, to determine the physical and chemical quality of the tap water samples from different talukas and villages of the Jalgaon district to ascertain basic drinking water quality standards as per IS 10500:2012.

### 2. Methodology

According to the IS code 10500:2012, some important terminologies are:

- Drinking water: Water intended for human consumption for drinking, and cooking purpose. It includes water supplied by any

means (treated or untreated) for human consumption.

- Acceptable limit: Allowed limit which is to be implemented. The value in excess of the allowable limit indicates water is not suitable but still may be tolerated in the absence of alternate source only allowed till permissible limit.
- Permissible limit: Maximum allowable limit

Water quality parameters can be classified as physical, chemical and biological water quality

parameters. Physical water quality parameters can be sensed by us by means of eye, nose, ear, tongue and skin. Chemical and biological parameters are determined by performing some experimental tests and indicates chemical and bacteriological quality of water. The presence of virus, bacteria, protozoa, algae are used to check biological quality of water.

The standard limits of the physicochemical water quality parameters are as mentioned below

**Table 1: Standard limits of physicochemical water quality parameters from IS 10500:2012**

Sr.No.	Parameter	Acceptable Limit	Permissible Limit
1	Odour	Agreeable	Agreeable
2	pH	6.5-8.5	No relaxation
3	Turbidity	1 NTU	5 NTU
4	Total Dissolved Solids (TDS) (mg/l)	500	2000
5	Total Hardness as CaCO <sub>3</sub> (mg/l)	200	600
6	Total Alkalinity as CaCO <sub>3</sub> (mg/l)	200	600
8	Ca <sup>+2</sup> (mg/l)	75	200
9	Mg <sup>+2</sup> (mg/l)	30	100
11	Chloride (mg/l)	250	1000
12	Fluoride (mg/l)	1.0	1.5
13	Iron as Fe (mg/l)	0.3	No relaxation
14	Sulphate as SO <sub>4</sub> (mg/l)	200	400

The analysis of the water samples was carried out by the standard techniques mentioned in IS 3025 and American Public Health Association (APHA) manual (Mote & Patil, 2016).

All the samples were collected in the month of January and analysed in the laboratory of Department of General Engineering, Institute of Chemical Technology (ICT), Mumbai. Various physicochemical analysis like water pH, Temperature, total dissolved solids (TDS) and conductivity are conducted by digital pH meter, conductivity meter and TDS meter (procured from Hanna Instrument). Turbidity was analysed using Digital turbidity meter (SYSTRONICS TYPE:135). Chlorides, total

hardness, total alkalinity, calcium, magnesium, fluoride and sulphate and iron were analysed using the standard methods (Kisan et al., 2002)

### 3. Analysis of Results and Discussion

All the samples had clear physical appearance, no colour and no smell. Table 2 gives results of analysis of water samples for parameters such as pH, temperature, conductivity, turbidity, TDS, total hardness and total alkalinity whereas, Table 3 gives results of presence of chloride, fluoride, iron, sulphate, calcium and magnesium.



**Table 2: Results of parameters of tap water sample**

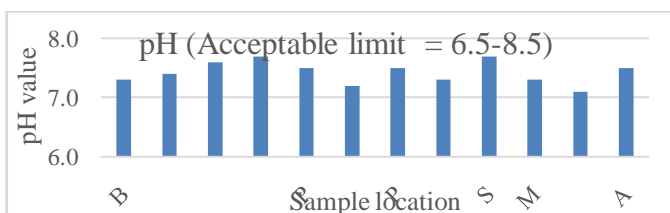
Sr.No.	Sample location (Village)	Sample location (Taluka)	pH	Temp (°C)	Conductivity (ms/cm)	Turbidity (NTU)	TDS (mg/l)	Total Hardness as CaCO <sub>3</sub> (mg/l)	Total Alkalinity as CaCO <sub>3</sub> (mg/l)
1	Bhusawal	Bhusawal	7.3	27.1	0.53	0	383	800	200
2	Shindi	Bhusawal	7.4	25.2	1.19	1	850	980	300
3	Aklud	Yawal	7.6	25	0.68	1	470	600	200
4	Kasva	Yawal	7.7	25	0.67	1	480	640	100
5	Pimprud	Yawal	7.5	27.3	0.62	0	444	200	400
6	Faizpur	Yawal	7.2	27.9	0.44	0	315	320	400
7	Padalsa	Yawal	7.5	28	1.42	4	1033	660	300
8	Bamnod	Yawal	7.3	28	1.17	1	843	500	500
9	Savda	Raver	7.7	28.2	0.42	0	304	380	300
10	Maskawad	Raver	7.3	27.3	1.25	3	910	720	200
11	Chinaval	Raver	7.1	26.9	0.78	0	550	400	200
12	Asoda	Jalgaon	7.5	28.1	0.69	0	498	260	700

**Table 3: Results of chemical parameters of water sample**

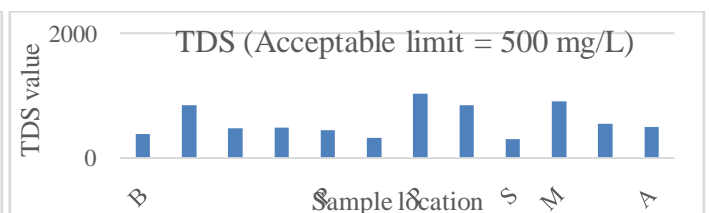
Sr.No.	Sample location (Village)	Sample location (Taluka)	Ca <sup>2+</sup> (mg/l)	Ca <sup>2+</sup> as CaCO <sub>3</sub>	Mg <sup>2+</sup> (mg/l)	Mg <sup>2+</sup> as CaCO <sub>3</sub>	Chloride (mg/l)	Fluoride (mg/l)	Iron (mg/l)	Sulphate (mg/l)
1	Bhusawal	Bhusawal	56.12	200	160.81	146.4	227	0.167	0.10	25.65
2	Shindi	Bhusawal	208	340	112	156.2	184.6	0.147	0.15	78.95
3	Aklud	Yawal	48.1	170	116.95	112.4	198.8	0.19	0.18	43.84
4	Kasva	Yawal	96.19	300	97.45	82.9	184.6	0.24	0.12	44.85
5	Pimprud	Yawal	56.12	120	14.62	19.52	113.6	0.264	0.16	19.69
6	Faizpur	Yawal	72.14	140	34.11	43.92	142	0.156	0.11	12.74
7	Padalsa	Yawal	184.36	400	48.73	63.4	340.8	0.132	0.12	49.48
8	Bamnod	Yawal	224.5	300	9.75	48.8	298.2	0.097	0.08	38.23
9	Savda	Raver	88.16	180	38.98	48.8	184.6	0.305	0.09	12.58
10	Maskawad	Raver	160.32	240	77.96	117	284	0.069	0.25	24.66
11	Chinaval	Raver	152.3	200	4.87	48.8	174	0.122	0.28	23.83
12	Asoda	Jalgaon	184.16	140	14.62	29.3	213	0.088	0.10	18.03

Many processes such as occurrence of odour, viscosity, chlorination etc. are based on temperature. Conductivity tells us about the ionic strength of the water and its ability to carry electric current. Turbidity in the water is aesthetically unacceptable and increases the

cost of water treatment. Turbidity is not observed in more than 50% of villages whereas in Maskawad and Padalsa village water turbidity is more than acceptable limit and less than permissible limit



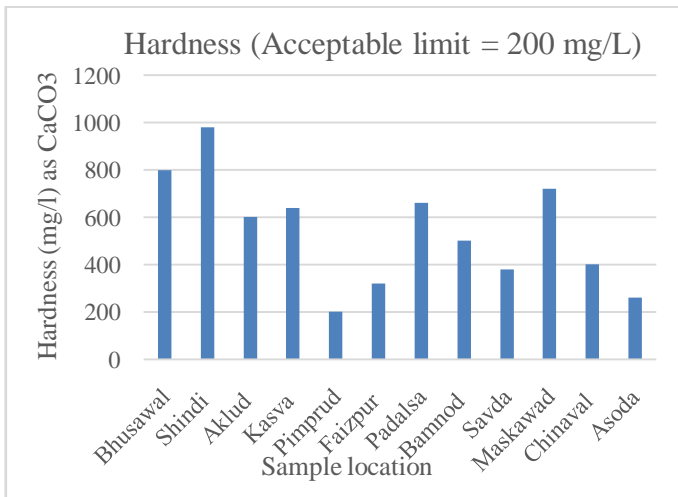
**Fig. 1: Results of pH of tap water sample**



**Fig. 2: Results of TDS of tap water sample**

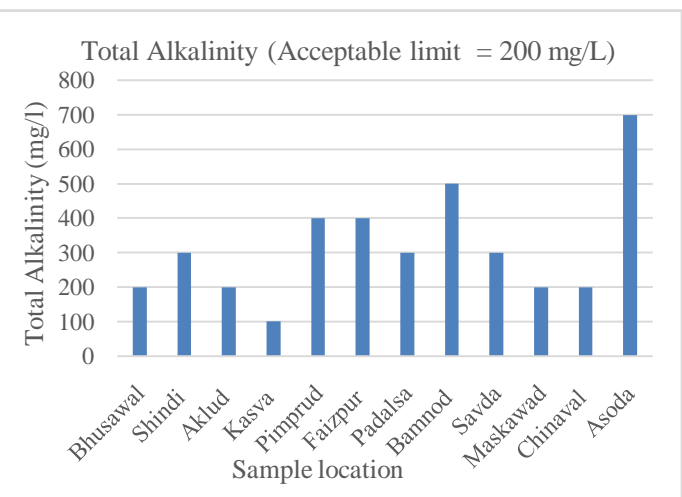
Figure 1 shows the results of pH at different sample locations. The pH values of all tap water samples are between 6.5-8.5, which satisfies the range of pH according to IS 10500:2012. If we consume water which has pH low than 6.5 it is likely to be contaminated by the pollutants making it unfit for drinking. Water having pH greater than 8.5 imparts bitter taste to water and can make our skin dry, itchy, and irritated.

Figure 2 represents the Total dissolved solids (TDS) of the water sample. The acceptable limit of TDS is 500mg/l while permissible limit is 2000 mg/l. In tap water samples of Shindi, Maskawad, Chinaval, Padalsa and Bamnod the TDS is above the acceptable limit of 500mg/l. Low TDS water doesn't affect our health but give flat taste to water as it has no minerals. High TDS imparts bitter taste and unpleasant smell to water.



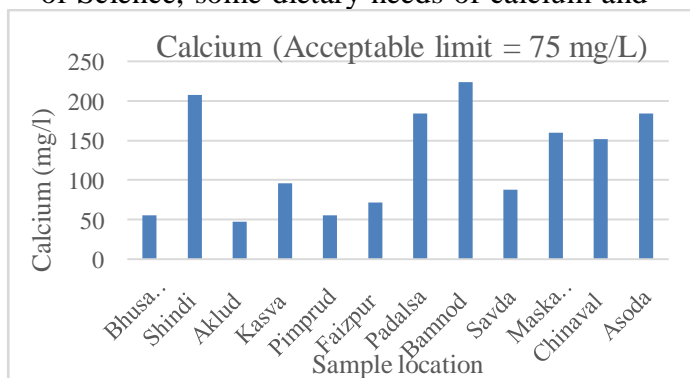
**Fig. 3: Results of Hardness test of sample**

Figure 3 represents data of the hardness of water sample. The acceptable limit for hardness is 200 mg/l while permissible limit is 600 mg/l. In all the above results, it can be seen that the hardness has exceeded the acceptable limit as well as the permissible limit value. It leads to poor lather formation with the soap, deterioration of the quality of clothes, formation of scales, irritation of skin as well as affect the quality of the food. Hard water is not a health hazard, thus its acceptable limit is not kept to zero. According to National Academy of Science, some dietary needs of calcium and



**Fig. 4: Results of total alkalinity test of sample**

magnesium are fulfilled by hard water. Some lower cardiovascular diseases are connected with hardness of water. Hence there is need to bring the hardness within the permissible limit. Figure 4 represents the total alkalinity of water sample. Alkalinity can be majorly caustic, carbonate or bicarbonate. The location such as Shindi, Pimprud, Faizpur, Savda, Padalsa, Bamnod, Amoda showed higher levels of total alkalinity than acceptable limit of 200 mg/l. Amoda showed results even higher than permissible limit of 600 mg/l.



**Fig. 5: Results of calcium test of sample**

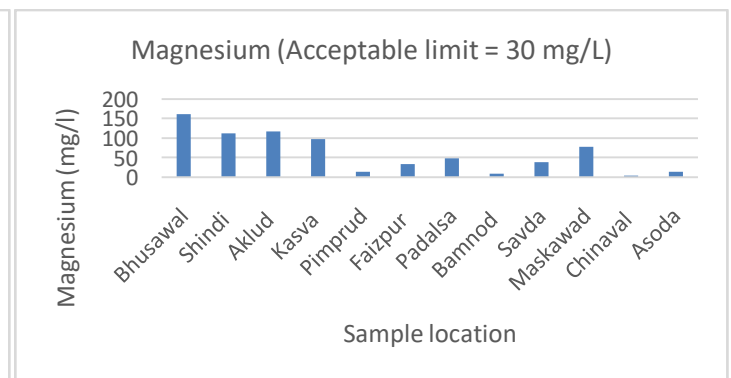


**Fig. 6: Results of magnesium test of sample**

Figure 5 shows the result of calcium test on sample of various locations. Many places indicate the exceedance in the acceptable limit of 75mg/l of Ca<sup>+2</sup>. Bamnod and Amoda shows calcium content even higher than acceptable limit of 200 mg/l. High calcium contributes to the high hardness. Hardness causes clogging of pipes, raises cost of heating of water, reduces the efficiency of water heater.

Figure 6 shows many water samples have higher magnesium content. The villages such as Bhusawal, Shindi and Aklud has magnesium levels even higher than the permissible limit of 100mg/l. High magnesium content contributes to the higher hardness of water. Magnesium hardness is even related with the kidney stoneformation.

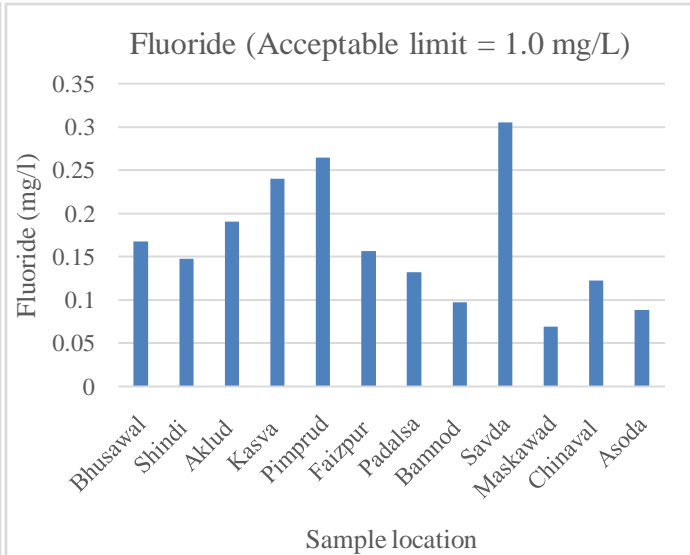
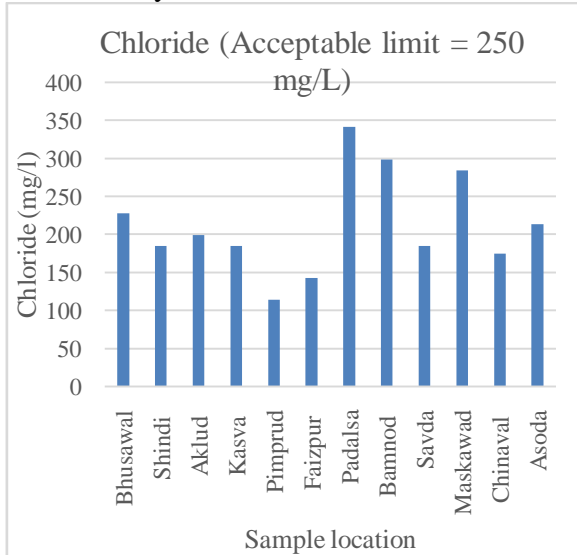


Fig. 7: Results of chloride test of sample

Fig. 8: Results of fluoride test of sample

Figure 7 indicates the result of testing of chloride in the water sample. Water samples from Padalsa and Bamnod shows the higher chloride content with respect to the acceptable limit of 250 mg/l. No sample showed the chloride concentration more than 1000mg/l. High chloride in water causes unpleasant salty taste for most people.

Figure 8 shows the fluoride test results. All the sample contain fluoride well below 1mg/l-1.5 mg/l. Small amount of fluoride is necessary for the formation of teeth and to prevent tooth decay whereas excessive amount can cause dental fluorosis.

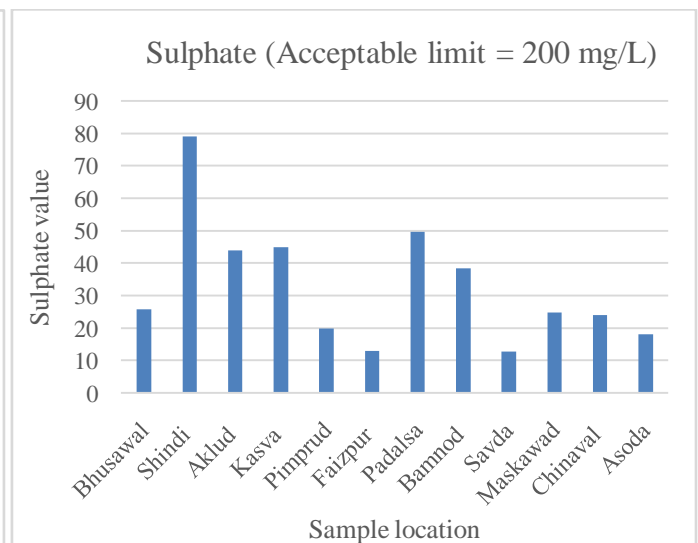
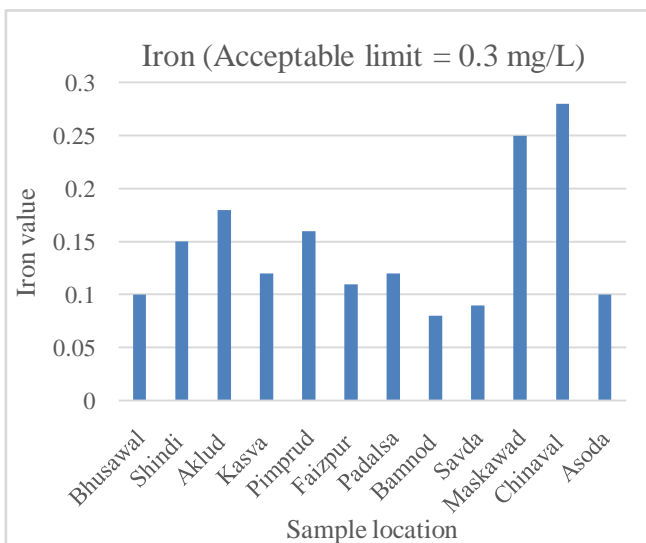


Fig. 9: Results of Iron test of sample

Fig. 10: Results of Sulphate test of sample

Figure 9 shows the iron content of the samples. All the places have iron less than acceptable limit of 0.3 mg/l. If iron levels are high, it imparts bitter taste, add turbidity and cause stains on the laundry.

Figure 10 represents the sulphate content of the sample. All the locations have sulphate content below the range of 200-400 mg/l. If sulphate content is found to be high in drinking water, there can be unwanted laxative effects and objectionable tastes.

#### 4. Conclusion

According to IS code-10500:2012, the hardness of water doesnot meet the required standards in samples of many areas. High quantity of calcium and magnesium salts are

found in samples which contributes to the higher hardness of water. Boiling, addition of lime and washing soda, use of distilled white vinegar as the softener to remove hard water stains is suggested to tackle tap water hardness. Even the alkalinity results shows the presence of highly alkaline water in some areas. Continuous consumption of higher alkalinity water leads to formation of gastric juices and digestive enzymes. The other parameters pH, turbidity, TDS, chloride, iron, fluoride, sulphate, temperature were within the acceptable limits for the majority of samples. Necessary measures need to be taken at the district and village level to treat and supply the desired quality drinking water to the people of Jalgaon district.

#### 5. References

1. Golekar, Rushikesh, Mukund Baride, and Sanjaykumar Narayan Patil. 2013. "Assessment of Surface and Waste Water Quality for Irrigation Suitability: A Case Study of Jalgaon Urban Area, Maharashtra (India)." *Der Chemica Sinica, Pelagia Research Library* 4 (2): 177–81.
2. Mote, Sudhakar Pralhad, and Madhuri Satish Patil. 2016. "Seasonal Variation in Physico-Chemical Parameter of Tapti River Drinking Water in Varangaon Dist .Jalgaon , Maharashtra." *Journal of Chemical and Pharmaceutical Research* 8 (6): 237–39.
3. "Drinking Water Parameters- Microbiological, Chemical and Indicator Parameters in the 2014 Drinking Water Regulations 2014." 2014. Environmental Protection Agency.
4. APHA. 2002. "Standard Methods for the Examination of Water and Wastewater." American Public Health Association; American Water Works Association; Water Environment Federation.
5. "Indian Standard Drinking Water — Specification( Second Revision) IS 10500 (2012): Drinking Water." 2012. Bureau Of Indian Standards.
6. Kisan, Mazdoor, Shakti Sangathan, Jawaharlal Nehru, and SatyanarayanGangaram Pitroda. 2002. "IS 3025-11 (1983): Methods of Sampling and Test (Physical and Chemical) for Water and Wastewater, Part 11."
7. Baird, Rodger B., Andrew D. Eaton, and Rice Eugene W. 2017. "Standard Methods for the Examination of Water and Wastewater." American Public Health Association; American Water Works Association; Water Environment Federation. <https://doi.org/10.1016/B978-0-12-382165-2.00237-3>.
8. "Indian Standard Water and Wastewater – Methods of Sampling and Test (Physical and Chemical) Part 40 Calcium." 2008.
9. Vijesh, V.K. 2013. "Ground Water Information Jalgaon District Maharashtra." Government of India, Ministry of Water Resources, Central Ground Water Board.
10. "Jalgaon River Linking Project-A Demand Based Project through Citizens Participation, Government of Maharashtra." 2010.

**STEEL SUPPLIER SELECTION USING ENTROPY AND COPRAS METHOD****S. D. Alone<sup>1</sup>, P.Naik<sup>2</sup> and D. N. Raut<sup>3</sup>**

Department of Production Engineering, VJTI, Mumbai

<sup>1</sup>sanketaloney127@gmail.com**ABSTRACT**

The objective of this research paper is to select the supplier for steel bars, which is an important material for industrial and construction purposes. The process of selection of supplier for various materials can decide the success of any engineering project. Complex Professional Assessment (COPRAS) is an important method for evaluation of alternatives in multi-criteria decision-making (MCDM) problems with respect to different criterions. In this paper, COPRAS method is used for ranking among the various available suppliers. The weightage for different criteria's is determined by ENTROPY method. Six criteria's, 3 beneficial and 3 non-beneficial criteria along with 5 suppliers are considered. Data related to these criteria and alternatives was collected with help of field experts and from the test results that were available. A real time example is illustrated to demonstrate the capability and pertinence of the adopted method.

**Keywords:** Complex Proportional Assessment (COPRAS), Entropy, Multiple criteria Decision Making (MCDM), Supplier Selection.

**1. Introduction**

For any manufacturing concern, deciding the perfect supplier is an arduous task. The weak and strong points of the supplier vary and make the procurement of material whether raw or finished strenuous for the purchasing firm and it becomes important to analyse the suppliers before choosing between them. Number of criteria and sub-criteria are involved in the evaluation of the supplier before procuring it. Supplier evaluation is a problem that involves multiple criteria which include both tangible and intangible factors. Quality, cost, and on time delivery are directly affected by appropriate supplier selection. Selection of right suppliers helps industries to achieve higher customer satisfaction thus acquiring greater market share. Supplier selection can be done using MCDM methodology in which various criteria related to quantity and quality are used to decide the rank of various supplier and select them accordingly. The supplier selection problem requires a sustainable approach to choose wisely between various parameters. The process of supplier selection directly affects the performance of the organisation as a whole. As a result of the improved supply chain for procuring of material whether raw or finished helps to bring about optimisation in the overall working of the organisation and thus to ensure the better performance, the evaluation and selection of supplier is very important.

**2. Review of Literatures**

For the selection of supplier various decision-making methods have been suggested in the literature. The process of supplier selection should be integrated with the working style of the organisation as the cutting edge obtained through use of quality material helps to gain customer trust in the long term. Bindu Madhuri et.al (2010) has mentioned a different approach that ensures that quality and quantity are both taken into consideration for evaluation of supplier (1). Sen Ouyang(et.al) 2013, puts forward an upgraded entropy method, which solves the matter of generally used entropy method. For ranking entropy method and correlation analysis for obtaining weights, helps to avoid the one sidedness (2). Shpend Imeri (2013) identified the crucial factors for supplier selection which helps to cut back the value of manufacturing and increase the profit margins (3). K Priyesh (2013) compared Thermo Mechanically Treated steel (TMT) performance with cold twisted steel. The factors such as chemical composition and physical properties are very crucial for understanding the true behaviour of structural members (4). Abhishek Mohite et.al (2014) examined various decision-making methods for solving supplier selection problems. (5). Giridhar Kamath et.al (2016) has proposed a particular method for choosing between various vendors for a steel pipe manufacturing firm in India. AHP method was used for

obtaining weightage of different criterions (6). Esra Aytac Adali et.al (2016) employed COPRAS and ARAS method for the choosing between best HVAC system for offices (7). Arzu Organ et.al (2016) used COPRAS method and came to conclusion that it is a good and useful method for selecting among various choices (8). A.E. Cengiz et.al (2017) has proposed a special approach for supplier selection of roofing materials and cladding. Criteria for supplier selection has been developed based on the expert opinion and research available (9) Naveen Jain and A. R. Singh (2018) proposed a hybrid methodology for supplier evaluation in Iron and Steel industry. Average value of weighted sum product has been applied for determination of suppliers and for weight determination Analytical Hierarchy Process has been applied (10). B. Vijaya Prakash and S. Sundarapandian (2016) conducted experiment and readings were taken from the plant. The data was analysed by Taguchi Method to search out the optimum combination of criteria's (11). Jagannath Roy et.al (2019) proposed a new model by combining COPRAS and WIRN method in order to decide the most suitable hotel for particular customer (12). Gholamreza Dehdasht et.al (2020) applied entropy weights and TOPSIS method for ranking to validate the soundness and exactness of the obtained results.(13). Bin Wang et.al (2020) has used entropy weight method for evaluation of groundwater susceptibility under influence of human activities. (14). Yuxin Zhu et.al (2020), came to the conclusion that among various weight determination method, Entropy weight method (EWM) is frequently used weighting method that measures value dispersion in decision-making (15).

### 2.1. Methodology for steel supplier selection using COPRAS method

COPRAS is one of the most used technique for decision making in multi-disciplinary environment and in the field of science and technology. This method is based on step-based ranking and forecasting cycle of given alternatives in the context of utility degree and its significance (27). It has been applied previously in the field of constructions,

building designs, road structure designs, education sector etc. COPRAS method includes several steps which are as follows.

Step 1. Formation of decision matrix, X.

Step 2. Normalization of matrix is done by using the equation given below:

$$r_{ij} = x_{ij} / \sum_{i=1}^m x_{ij}$$

(1)

Step 3: Determination of Weighted normalized decision matrix i.e.  $\check{X}$  by using below equation.

$$\check{X} = r_{ij} \times w$$

(2)

Step 4. Sum of weighted beneficial and cost criteria.

$$S_{+i} = \sum_{j=1}^n y_{+ij}, S_{-i} = \sum_{j=1}^n y_{-ij}$$

(3)

Where  $S_{+i}$  and  $S_{-i}$  are the weighted normalized values for the beneficial and non-beneficial criteria, respectively.

Step 5: Determination the relative significances of the alternatives  $Q_i$ , by using equation.

$$Q_i = S_{+i} + \frac{S_{-min} \cdot \sum_{i=1}^m S_{-i}}{S_{-i} \cdot \sum_{i=1}^m (S_{-min} / S_{-i})}, i = 1..m$$

(4)

Where  $S_{-min}$  is the minimum value of  $S_{-i}$ .

Step 6: Utility,  $U_i$  for  $i$ th alternative calculated by using equation.

$$U_i = \frac{Q_i}{Q_{max}} \times 100$$

(5)

Where,  $Q_{max}$  is the maximum value for relative significance,

The qualitative utility value of the alternatives ranges from 0% to 100%. The higher the value of  $U_i$ , then higher is the priority of the alternative. The utility values of the different supplier provide a complete ranking of the alternatives used.

### 2.2. Example for steel supplier selection

A real time supplier selection problem considered is deals with the selection of the most appropriate supplier for supplying the steel bar. Performance of steel bar is often specified using different attributes. The yield stress ( $N/mm^2$ ), % elongation, % carbon content, % Sulphur and Phosphorous content, tensile strength ( $N/mm^2$ ), cost/metric ton (Rs) are observed to be the most critical attributes affecting the steel bar selection. In this research paper, five different suppliers along with 6

criteria are considered. Among these 6 criteria, Yield stress, % elongation and tensile strength are beneficial criteria and remaining are the non-beneficial one. Table 1 shown the decision matrix used for selecting best supplier. The criteria weights are obtained using Entropy method and used for subsequent analysis. These obtained criteria weights are as  $w_c^* = 0.1492$ ,  $w_{ys}^* = 0.2588$ ,  $w_e^* = 0.1404$ ,  $w_{cc}^* = 0.1488$ .  $w_{ts}^* = 0.1504$  and  $w_{sp}^* = 0.1524$ . The normalised matrix and weighted normalized matrix are shown in Table 2 and Table 3 respectively.

Table 4 shows all the values of sum of weighted benefit criteria and Cost criteria. Then, the relative significances of the alternatives  $Q_i$ , and quantitative utility  $U_i$  are determined and result are presented in Table 5. Also, this table shows the ranking of alternative supplier obtained from utility values. The alternative S5 came out to be best alternative and S2 is the worst by using weights obtained from ENTROPY method. S5-S4-S1-S3-S2 is the final ranking results.

**2.3.Calculations for COPRAS method**

Criteria/ Alternative	Cost per metric ton (₹)	Yield Stress (N/mm <sup>2</sup> )	Elongation (%)	Carbon Content (%)	Tensile Strength (N/mm <sup>2</sup> )	Sulphur and Phosphorous content (%)
S1	54000	525	18	0.23	600	0.075
S2	70750	650	16	0.22	750	0.065
S3	51000	550	18	0.24	630	0.075
S4	39000	545	19.5	0.21	650	0.07
S5	54500	550	22	0.23	650	0.006

**Table 1. Decision matrix for steel supplier selection**

**Table 2. Normalization decision matrix.**

Criteria/ Alternative	Cost/ metric ton (₹)	Yield Stress (N/mm <sup>2</sup> )	Elongation (%)	Carbon Content (%)	Tensile Strength (N/mm <sup>2</sup> )	Sulphur and Phosphorous max content (%)
S1	0.2006	0.1862	0.1925	0.2035	0.1829	0.2577
S2	0.2628	0.2305	0.1711	0.1947	0.2287	0.2234
S3	0.1894	0.1950	0.1925	0.2124	0.1921	0.2577
S4	0.1448	0.1933	0.2086	0.1858	0.1982	0.2405
S5	0.2024	0.1950	0.2353	0.2035	0.1982	0.0206

**Table 3. Weighted normalized matrix**

Criteria/ Alternative	Cost/ metric ton (₹)	Yield Stress (N/mm <sup>2</sup> )	Elongation (%)	Carbon Content (%)	Tensile Strength (N/mm <sup>2</sup> )	Sulphur and Phosphorous max content (%)
S1	0.0299	0.0482	0.0270	0.0528	0.0275	0.0393
S2	0.0392	0.0597	0.0240	0.0504	0.0344	0.0340
S3	0.0283	0.0505	0.0270	0.0549	0.0288	0.0392
S4	0.0216	0.0500	0.0293	0.0481	0.0298	0.0367
S5	0.0302	0.0505	0.0330	0.0527	0.0298	0.0031

**Table 4. Weighted benefit and cost criteria**

Supplier	SUM(S+i)	SUM(S-i)
S1	0.1027	0.1219
S2	0.1181	0.1236
S3	0.1064	0.1225
S4	0.1091	0.1064
S5	0.1133	0.086

**Table 5. Values of  $Q_I$  and  $U_I$  with ranking**

Supplier	$Q_I$	$U_I$	Rank
S1	14.7442	70.6791	3
S2	14.5523	69.7592	5
S3	14.6728	70.3367	4
S4	16.8854	80.9432	2
S5	20.8608	100	1

### 3. Conclusion

From the selection of steel supplier by using COPRAS method we have obtained the best supplier from among the choice of five alternatives. In this research work entropy method is used for determining the weights of the different criteria. The final result ranking performance was obtained as S5-S4-S1-S3-S2 for the supplier selection for steel. The use of

MCDM methods such as COPRAS proves to be useful in the scenario where there are few numbers of supplier. In manufacturing industry, the application of Entropy along with COPRAS method can turn out to be very productive as the supplier selection helps to optimize the project in terms of cost and quality.

### References

1. Bindu Madhuri, Anand Chandulal, Padmaja. M. (2010). Selection of Best Web Site by Applying COPRAS-G method. *International Journal of Computer Science and Information Technologies*, Vol. 1 (2).
2. Sen Ouyang<sup>a</sup>, Ziwen Liu<sup>b</sup>, Qing Li<sup>c</sup> and Yili Shi. (2013). A new improved entropy method and its application in Power Quality Evaluation. *Advanced Materials research*, ISSN1662-8985.
3. Shpend Imeri. (2013). Key Performance Criteria for Vendor Selection – A Literature Review. *Management research and practice*, Vol. 5 Issue 2.
4. K Priyesh. (2013). Studies on Properties of TMT Steels for Structural Applications. *International Journal of Engineering Research & Technology (IJERT)*, Vol. 2 Issue 8.
5. Abhishek P. Mohitea, Tushar R. Mohiteb, Ketan M. Mathakarc, Sachin B. Khotd. (2014). A Review Paper on “Multicriteria Decision Making Approaches and Criterion” Used in Supplier Selection and Evaluation. *International Journal of Engineering Research & Technology*.
6. Giridhar Kamath Rakesh Naik Shiva Prasad H C. (2016). A Vendor’s evaluation—using AHP an Indian Steel Pipe Manufacturing Company. *International Journal of the Analytic Hierarchy Process*, Vol. 8 Issue 3.
7. Dr. Esra Aytac Adali and Dr. Ayğegül Tuğ İğik. (2016). Air Conditioner Selection Problem with COPRAS And ARAS Methods. *Manas Journal of Social Studies*.
8. Arzu Organ, Assoc. Prof. Engin Yalçın. (2016). Performance Evaluation of Research Assistants by Copras Method. *European Scientific Journal*.
9. A.E. Cengiz, O. Aytekinb, I. Ozdemir, H. Kusan, A. Cabuk, Croatia. (2017). A Multi-Criteria Decision Model for Construction Material Supplier Selection. *Creative construction conference*.
10. Naveen Jain, A. R. Singh. (2018). Supplier Selection in Indian Iron and Steel Industry: An Integrated MCDM Approach. *International Journal of Pure and Applied Mathematics*, Volume 118.
11. B. Vijaya Prakash, S. Sundarapandian. (2019). Selection of Effective Control factors for TMT Bars using Taguchi.



- International Journal of Engineering and Advanced Technology(IJEAT), ISSN: 2249 – 8958, Volume-8, Issue-6S3.
12. Jagannath Roy, Hareesh Kumar Sharma, Samarjit Kar, Edmundas Kazimieras Zavadskas & Jonas Saporauskas. (2019). An extended COPRAS model for multi-criteria decision-making problems and its application in web-based hotel evaluation and selection. Economic Research-Ekonomiska Istrazivanja, Volume 32.
  13. Gholamreza Dehdasht, M. Salim Ferwati , Rosli Mohamad Zin , Nazirah Zainul Abidin. (2020). A hybrid approach using entropy and TOPSIS to select key drivers for successful and sustainable lean construction implementation. <http://doi.org/10.1371/journal.pone.0228746>.
  14. Bin Wang, Yanguo Teng, Huiqun Wang, Rui Zuo, Yuanzheng Zhai, Weifeng Yue and Jie Yang. (2020). Entropy weight method coupled with an improved DRASTIC model to evaluate the special vulnerability of groundwater in Songnen Plain. <http://creativecommons.org/licenses/by/4.0>.
  15. Yuxin Zhu, Dazuo Tian, and Feng Yan. (2020). Effectiveness of Entropy Weight Method in Decision-Making. Mathematical Problems in Engineering.

**COMPARISON OF BRICKS MADE UP OF DESERT SAND AND METAKAOLINE WITH FLY ASH BRICK****S. R. Jangid<sup>1</sup> and R.P Borkar<sup>2</sup>**<sup>1</sup>Government College of Engineering, Jalgaon, Maharashtra India.<sup>2</sup>Government College of Engineering, Amravati, Maharashtra India<sup>1</sup>shivnathjangid@gmail.com, <sup>2</sup>rporkar@rediffmail.com**ABSTRACT**

*This paper performed comparative experimental investigation of brick made up of desert sand and metakaoline with brick made up of fly ash and Portland cement. Desert sand and metakaoline is added in various proportions to prepare the brick, the weight of desert sand and metakaoline is in percentage of weight of brick. Both desert sand brick and fly ash brick are made by applying compressive force on raw material by hydraulic compression machine. To examine physical properties of desert sand, sieve analysis and Pycnometer test, for properties of cement and metakaoline, Fineness, Standard consistency, Initial and final setting time, Soundness, Compressive strength, for Crushed Stone are performed. Moreover, physical properties of desert sand brick are examining by under dimension tolerance, density, compressive strength and water absorption of desert sand brick. The result showed sustainable improvement in the hardness of desert sand brick over fly ash brick. The rise in the strength of desert sand brick is phenomenally varies as percentage of material such as crushed stone increases. The present study shows improvement in the characteristics of brick made up of desert sand and metakaoline when compare with fly ash brick*

**Keywords:** Desert Sand Brick, Metakaoline, Compressive Strength, Fly Ash Brick.

**1. Introduction**

The Great Indian Desert known as Thar Desert in the west of Rajasthan covers 2,00,000 sq km area (Roy, 1978). This is 61.3% of Rajasthan state area and 6.3% of country area (Ameta, 2013). This soil is non-cohesive in nature and hence soil is susceptible to easy erosion by rain and wind (Al- Khanbashi et al., 2000). also, desert sand is loose and susceptible to collapse upon wetting due to rainwater (Elsharief et al., 1999). Desert sand is not appropriate to use in constructions without addition of binders. Hence, desert sand is mixed with binders such as cement, natural clays, bentonite, cement- by-pass dust, and incinerator ash, to construct roads, water barrier structures (Mohamedzein et al., 2003). and metakaoline (raw material for Alkali activated cements (Palomo, et al., 1999; Zhang et al., 2010a, 2010b).

Alkali activated cements (AAC) are inorganic polymers (IP) which are produced from activation of solid alumino-silicate material. This result in a new class of three-dimensionally network of alkali alumino-silicates (Ingles, 1970; Patfoort and Wastiels, 1989; Abdullah, 2012; Jaarsveld et al., 2002; Rowels and O'Connor, 2003; Duxson, et al., 2007; Slaty et al., 2013; Lemougna et al.,

2014). These are alternative materials to Portland cement as they have a comparable hardness, chemical stability, and compressive strength, but they required less energy for manufacturing. and meanwhile alternative binders emits less greenhouse gases during production (Patfoort and Wastiels, 1989; Steveson and Sagoe-Crentsil, 2005, Xu and Deventer, 2000). Earlier journals observed the durability characteristics was more for geopolymer and other AAC obtained from different raw materials like metakaoline (Palomo, et al., 1999; Zhang et al., 2010a, 2010b). Metakaoline is alternate binding material to cement used for various mixtures in different proportions (Peigang, et al. 2016). This means Metakaoline can bring positive effect not only on early strength of 28-days, but also on durability especially frost resistance of structure (Bilek et al. 2013). The results indicated that these materials have a good resistance against erosion and durability.

Till date, it is observed that there is a grey area to work on desert sand for making bricks with the help of desert sand and metakaoline as binder. The purpose of this research is to investigate the strength of desert sand brick in comparison with fly ash brick.

**2.0 Research Objectives**

This study proposes the following objectives:

1. Assessment of engineering properties of desert sand.
2. Preparation of bricks made of desert sand and mixed with different proportion of filler (Crushed Stone) and binders (Metakaoline).
3. To test performance of brick based on different parameters such as Dimension tolerance, Density of brick, compressive strength, water absorption.
4. Finding optimum mix proportion of brick for best result when tested under above parameters.

**Material for Manufacturing**

**Desert Sand**

Desert sand is easily available at Thar Desert in west Rajsthan which cover nearly 61.3% of area of Rajsthan state (Ameta, 2013 Roy, 1978). Desert Sand is light yellowish brown colour cohesionless soil with loose soil structure and the clay content in sub soil region varies from 4 to 8% and pH ranges from 8.0 to 8.5 (Roy, 1978). The chemical composition of Desert sand is shown in Table 1 and has large proportion of silicon dioxide ( $SiO_2 \approx 78\%$ ) and negligible proportion of gypsum which proves that the desert sand is cohesion less soil (O. Benjeddou et.al. 2020).

**Table 1:** Composition of desert sand

Component	Al <sub>2</sub> O <sub>3</sub>	CaO	Fe <sub>2</sub> O <sub>3</sub>	K <sub>2</sub> O	MgO	SO <sub>3</sub>	TiO <sub>2</sub>	PAF	SiO <sub>2</sub>
Percentage	1.15	5.69	0.47	0.81	0.10	9.29	0.18	4.58	78.15

The test carried out on the desert sand is the particle size distribution according to IS :2720 (Part III & C-1) -1930. On the basis of Gradation curve, which shows that desert sand, is very fine

soil. From the curve, the value of coefficient of curvature (Cc), and coefficient of uniformity (Cu) is determining which shows  $Cc < 1$  and  $Cu < 1.5$  which are well within the limits mentioned in Indian Standard code.



**Figure 1** Sieve analyses test on desert sand

From particle size analysis fineness modulus is also being calculated as per IS:2720 (Part III/& C-1)-1930 which is 0.24 and indicate that the soil is too fine and all particles are of equal size. To determine the specific gravity of desert

sand by Pycnometer test mentioned in IS:2720 (Part III & C-1)-1930 is as follows and the average specific gravity of desert sand varies from 2.53 and water absorption 0.71%.



**Figure 2** Pycnometer test on desert sand.

### Crushed Stone

This is fine crushed stone which obtained in crusher after crushing large size stones into small. These are typically of various sizes but this context used is 6 mm in size. This fine stone is mixed with desert sand which function is same way as that of aggregate in concrete mixture. Specific gravity and water absorption of aggregate test is conducted to find out the feasibility of aggregate used in manufacturing of the desert sand brick. The procedure of testing aggregate for water absorption is followed as per IS: 2386 PART 3-1963 and that of specific

gravity is per IS: 2386 PART 4-1963. The value of above test is well within the mentioned range, water absorption is 2.64% and specific gravity is 2.67.

### Cement

The cement utilizes in manufacturing of desert sand brick is of 53 grades, each bag of 50kg by weight. All the properties which standardize Cement as per the IS code are carried out on them. The test result of cement as per IS code are as follows.

**Table 2: Properties of Cement**

Sr. no.	Test performed	IS code	Result
1	Fineness of cement	IS: 4031 PART 1-1996	3.5 %
2	Standard consistency	IS: 4031 PART 4-1988	28 %
3	Initial and final setting time	IS: 4031 PART 5-1988	27 min and 585 min
4	Soundness of cement	IS: 4031 PART 3-1988	9.5 mm
5	Compressive strength of cement	IS: 4031 PART 6-1988	52.3N/mm <sup>2</sup>

The cement used in this experimental study is a locally available. The results of the tests showed that the fineness and consistency of cement is 3.5% and 28% respectively. When cement is tested for initial and final setting time, it observes to be 27 minute and 585 minutes respectively. The most important parameter which tested is compressive strength and average of all result is found out to be 52.3 N/mm<sup>2</sup>.

### Fly Ash

Coal of Indian origin belongs to sub-bituminous, bituminous or lignite quality. It has following values: moisture content up to (Gupta M, et. al. 2000; Chandra A, et. al. 2004) 1.9-8.3 and the proportion of various elements are C, 39.3-60.2; H, 2.8-4.2; S, 0.3-0.5; N, 0.9-1.9; and O, 4.9-%. Usually, the particle of Fly Ash particles light weight (density 1.97-2.89 g/cc), spherical (specific surface area,

4000-10,000 cm<sup>2</sup>/g; diameter, 1-150 m), very fine, refractory and have binding ability (Ganesh Babu, et. al., 2001). The colour of the Fly ash is grey to blackish grey which depends on combustion process and type of coal.

The Chemical component (Singh D V, et.al., 1996; Prasad A, et.al., 1999; Kumar P, et. al., 2005) of FA is as follows: SO<sub>3</sub>, 0.76; MgO, 0.97; alkalies, 1.41; CaO, 1.94; Fe<sub>2</sub>O<sub>3</sub>, 6.11; Al<sub>2</sub>O<sub>3</sub>, 23.59; SiO<sub>2</sub>, 59.38; and unburnt S & moisture, 3.74%. The binding property of fly ash is depending on Oxides of silicon, calcium, aluminum and iron, which is decreases by loss of ignition (Jain A K, et.al., 2001).

### 3.5 Metakaoline

Metakaoline is white colour product made from kaolinite clay stone which is calcined in a rotary kiln at 750<sup>0</sup>C with together grind in fine powder (Pavlina Hajkova, 2018).

**Table 3: Properties of Metakaoline**

Sr. no.	Test performed	IS code	Result
1	Fineness	IS: 4031 PART 1-1996	1.5 %
2	Standard consistency	IS: 4031 PART 4-1988	37 %
3	Initial and final setting time	IS: 4031 PART 5-1988	36 min and 790 min
4	Soundness	IS: 4031 PART 3-1988	7.0 mm
5	Compressive strength	IS: 4031 PART 6-1988	49.10N/mm <sup>2</sup>

The Metakaoline used in this context will be available in building material shops. Various tests are performed on metakaoline and the test result show that the fineness and consistency of metakaoline is 15% and 37% respectively. When it tested under initial setting time the result observes to be 36 minute and when tested under final setting time the result observes to be 790 minutes. The most important parameter which tested is compressive strength and average of all result is found out to be 49.10 N/mm<sup>2</sup>.

### Plan of Project

#### Collection of Material

The ingredients of brick such as desert sand, cement, metakaoline, and crushed stone. Desert sand was transported from Great Indian Desert, Jaisalmer, Rajasthan, cement of 53 grade and metakaoline is obtained from local dealer, and crushed stone is obtained from crusher plant near city. After collection of all ingredients, they were transported to Government College of Engineering, Jalgaon at which the testing being conducted and bricks are casted.

#### Material Testing

This part of experiment will show various test to be performed on collected material. The test

conducted on Desert sand were Pycnometer, sieve analysis, water absorption and procedure are followed according to Indian Standard Code. These tests are useful to examine the properties of Desert sand. Specific gravity and water absorption of aggregate are conducted on crushed sand. Some physical and chemical properties of Fly ash are also examined. Fineness, Standard consistency, Initial and final setting time, Soundness, Compressive strength these tests are performed on cement and metakaoline which are binder.

### Batching

Batching was most important step because it was to decide the various percentages of ingredients to be mixed for making bricks. The percentages of ingredients in bricks varied from 5 to 20% for cement and metakaoline and 5 to 20% of crushed stone. The entire ingredients were packed in set of desert sand-crushed stone-metakaoline for manufacturing of desert sand brick and fly ash – crushed stone – cement for manufacturing the fly ash brick as shown in table below. At the time of manufacturing this were used to make brick of each category.

#### Fly ash, Crushed Stone and Cement [A]

**Table 4:** Batching of Type-A Brick

Sample number	Fly Ash (%)	Crushed Stone (%)	Cement (%)
A1	90	5	5
A2	80	10	10
A3	70	15	15
A4	60	20	20

#### Desert Sand, Crushed Stone and Metakaoline (B)

**Table 5:** Batching Of Type-B Brick

Sample number	Desert Sand (%)	Crushed Stone (%)	Metakaoline (%)
B1	90	5	5
B2	80	10	10
B3	70	15	15
B4	60	20	20

#### Preparation of Specimens

This part of the present experimental investigation consists of preparing various

specimens of desert sand – Metakaoline and fly ash – Cement along with Crushed Stone. The composition of different mixtures is presented

in Table 4 and 5. It is noted that cuboid specimen shapes were prepared and tested in this work. Cuboid specimens were used to determine the compressive strength and water absorption for final product at age of 7 days as

1. Dry mixing of Desert Sand, metakaoline and Crushed stone (Fig. 3a).
2. Pouring of water in the mixture.
3. Wet mixing, first, for 30 seconds with slow speed and then for 1 minute with high speed



Fig. 3 a) Dry Mixing of all ingredients

shown in Table 10 and 11. The dimensions of the cuboid specimen are 190 mm × 90 × 90mm. The steps of the used mixing procedure are the following,

4. (Fig. 3b);
4. Pouring of the mixture in the cubic moulds.
5. Applying hydraulic compressive force (fig. no, 4)
6. finally, removing of cuboid specimens.



b) Wet mixing of all ingredients

### Manufacturing of Brick

In this process, the wet material was then moved in mould where it was compressed with

sufficient amount of pressure to get brick. After the compression, bricks were taken out for drying to acquire strength.



Fig. 4 Applying pressure on material by Hydraulic Compression Machine

### Drying and Curing of Brick

The process of drying is followed by process of casting of bricks under hydraulic compression machine. The drying must be in shade because it causes loss of water due to evaporation which may causes the brick to crack. The specimens were kept, until the testing time, for shade drying under normal temperature such as 23 °C and a relative humidity between 55 and 65%. After getting initial strength to brick curing is done by sprinkling water on surface which prevent the evaporation loss from brick. The process of curing will be continued for 7 days. In drying process brick gets sufficient strength, so this step is necessary in the manufacturing of bricks.

### Testing

Dried and cured desert sand or fly ash bricks were brought to laboratory for testing of compressive strength and water absorption after 7 days. Each set of batches had six numbers of bricks such that three were going to be used for compression testing and remaining three for water absorption test.

### Geometrical Properties

Here are some of the geometrical properties such as length, width and height of bricks are considered and compared with Fly Ash brick. The size of brick used in construction varies from country to country and from place to place. In India, the recommended standard

size of an ideal brick is 190 x 90 x 90 mm which with mortar joint gives net dimensions of 200 x 100 x 100 mm.

### Density Of Brick

In this process, every specimen whose density has to be measure is weighted. The dimension of each manufactured specimen is found to be 190x90x90mm. The density of each specimen is measured after 7 days curing when its mass is stabilized. The results obtained under this test are presented in Table number 9 which gives densities of the specimen of each mixture.

### Compressive Strength

The compressive strength tests, at the age 7 days, were carried out on Cuboidal specimens for each mixture, and this is in accordance with the requirements of the IS code for brick testing as per IS 1325-1992 Part I. The above specimen is place under Compressive Testing Machine and procedure is followed according to IS code. The Specimens were tested in Compression Testing Machine (CTM) under a constant applied load speed until rupture of specimen (Fig. No. 6). The compressive strength graph at the age of 7 days of all tested specimens is presented in Graph number 2. In addition, Table number 10, gives the compressive strength data of all tested specimens at the age of 7 days.

**Table 6:** Length of fly ash brick and desert sand brick

Types of Brick	Length in mm	Width in mm	Height in mm
Fly ash brick	193	91	92
Desert sand brick	192	90	91

From above result, it is observed that dimension of Desert sand brick is same as that of burnt bricks which is approximately 190x90x90 mm. This is beneficial in actual practice such as it easy to handle and transport. Sometime hollow brick can also be manufactured.

### Water Absorption

The water absorption of bricks was measured according to the requirements of the IS 1325-1992 Part II. Apart from compressive strength, water absorption is an important property in of any brick used in construction industry. This property can affect the quality of the brick itself and the bond strength between the brick and mortar in masonry structures. Hence this test is one of the important tests for brick.

### Results and Discussion

In the technically terminology, brick is the standard size, shape and weight of building unit. The standard size of brick includes its length, width and height. These geometrical properties are considered for brick which has some different dimensions. This is important due to efficient and easy handling and lying of brick. According to Indian Standards, the brick must have twice width for proper bond and stability of structure. Selection of any material for construction depends on its colour, surface texture, and weight.

### Geometrical Properties

As per IS 1725-1982, the standard dimension of brick is 190x90x90mm and the maximum tolerances are  $\pm 5$  mm for length,  $\pm 0.5$  mm for width, and  $\pm 2$  mm for height. According to the results presented in table number 6 the all values of bricks are well withing the range and allowable.

### Density of Brick

As per IS code 1725-1982 weight of the burnt convectional bricks should be nearly 3200 gm. The following table shows the average weight of desert sand bricks.

**Table 7:** Weight and density of fly ash brick and desert sand brick

Types of Brick	Type of brick	Weight in gm	Density gm/cc
Fly Ash + crushed Stone + cement	A1	2089	2.30
	A2	2141	2.48
	A3	2185	2.52
	A4	2322	2.63
Desert sand + crushed Stone + metakaoline	B1	2963	2.34
	B2	3266	2.58
	B3	3291	2.60
	B4	3359	2.66

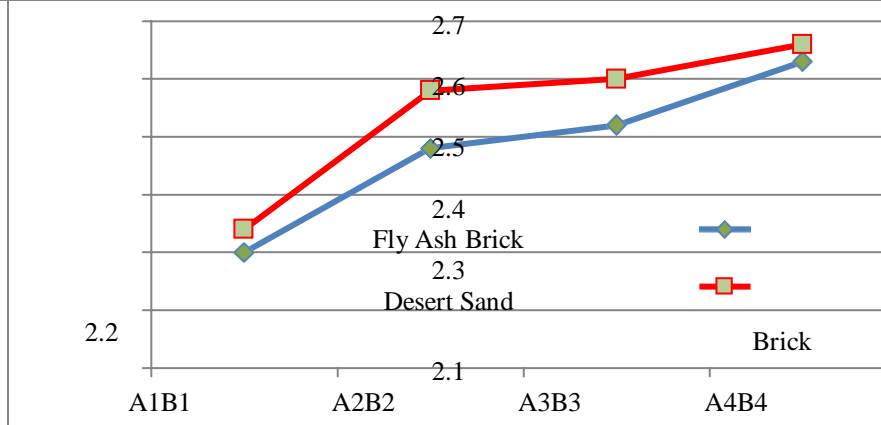


**Fig. 5** Density of fly ash brick and desert sand brick

From the above data it is observe that the weight of Desert Sand bricks (B) are more than that of Fly Ash bricks (A). As the percentage of crushed stone increase the weight of brick which also increases from brick A1 to A4 and B1 to B4. From above the brick which gives optimum strength will be consider as best brick among the tested bricks.

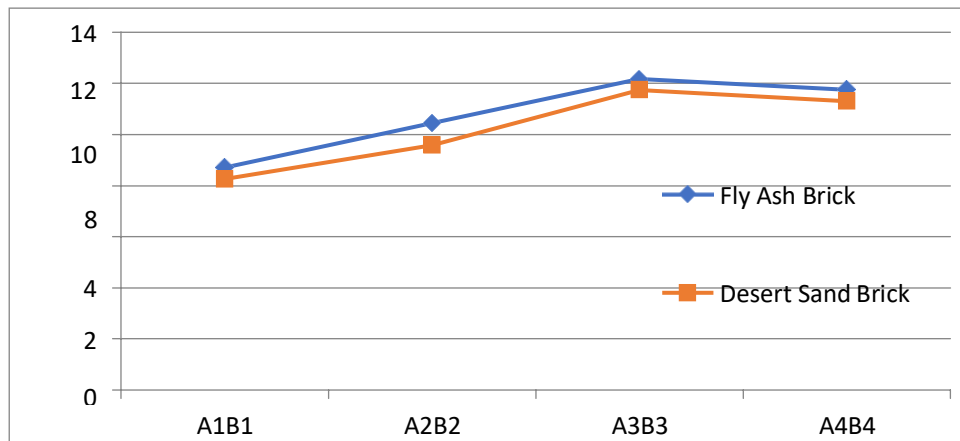
**Compressive Strength**

As per 1325–1992-page no. 2 specify that the compressive strength is 10.5 N/mm<sup>2</sup> for first class burnt brick. The following table shows various types of brick and their respective compressive strength.

Types of Brick	Type of brick	Compressive strength (N/mm <sup>2</sup> )
	A1	8.70
Fly ash brick + crushed Stone +cement	A2	10.43
	A3	12.17
	A4	11.74
Desert sand + crushed Stone +metakaoline	B1	8.26
	B2	9.57
	B3	11.74
	B4	11.30



**Table number 10:** Compressive strength of Fly ash brick and desert sand brick



**Graph no. 2.** Compressive strength of fly ash brick and desert sand brick

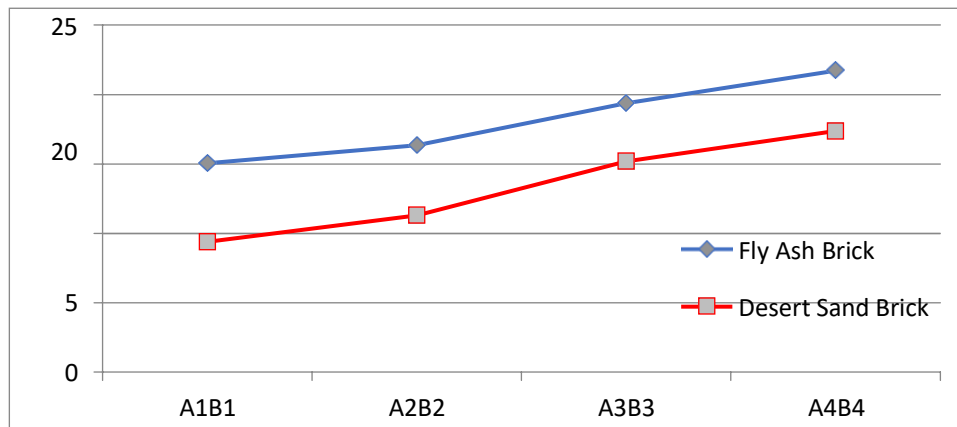
Compressive strength and water absorption are the two most important tests to select the best brick among the above. From the above result, it is found that the brick with 70% of Fly Ash, 15% of Crushed stone and 15% of cement will show maximum compressive strength of 12.17 N/mm<sup>2</sup> in type of brick A that of in type of brick B, 70% Desert sand, 15% crushed stone and 15% metakaoline will show optimum strength of 11.74 N/mm<sup>2</sup>. The bonding

property of cement is more than that of metakaoline hence the strength of cement brick is more than that of metakaoline brick.

**Water Absorption**

As per 1325-1992 part II, specifies that the water absorption test and its value is 15% for first class brick. The following table shows the various percentages of water absorption for various types of bricks.

Types of Brick	Type of brick	Water absorption (%)
Fly Ash + crushed Stone + cement	A1	15.03
	A2	16.33
	A3	19.34
Desert sand + crushed Stone + metakaoline	A4	21.70
	B1	9.38
	B2	11.27
	B3	15.19
	B4	17.36

**Table number 11:** Water absorption of brick A, B & Fly Ash brick**Graph no. 3** Water absorption of fly ash brick and desert sand brick

The water absorption test was conducted after the curing of seven days for cement and metakaoline bricks. It is found that when the percentage of cement increases the water absorption of brick going to increase. This is due to increase in heat of hydration of cement in brick. This will be same in metakaoline bricks.

### 6.0 Conclusion

The present context was conducted to verify the potential of desert sand. The following conclusion is drawn based on the current investigation:

1. From the experimental work, it observes that, there is no change in shape, size and structure of the bricks after curing period which shows these bricks are versatile for the construction works.
2. Brick made with help of metakaoline as binder shows sufficient increase in density of brick in comparison with brick made up of cement as binder, which improve compressive strength and durability of material.
3. The rise in the density of desert sand brick is phenomenally increase by 3.17% in

comparison with fly ash brick. Rise in density indicates the increase in the hardness of the brick.

4. The water absorption percentage of IS recommended brick is up to 15% such criteria is fulfilling by desert sand brick when it manufactures with 15% of metakaoline by weight of brick. At the same time fly ash brick exceed the IS limit of water absorption.
5. Brick manufacture with the desert sand and metakaoline fulfil the requirement of first-class brick (10.5N/mm<sup>2</sup>) which is 11.74N/mm<sup>2</sup> for B3 brick.
6. From the above research work it is concluded that the most appropriate percentage of metakaoline in combination of desert sand is 15%.

Finally, the use of desert sand in building material satisfies primary criteria of Indian Standard and will gives better compressive strength when compared with burnt brick. The materials used for making desert sand block as eco-friendly hence the obtained product may be classified as green building material.

## References

1. Abdullah, M. M. A. B., Jamaludin, L., Hussin, K., Bnhussain, M., Ghazali, C. M. R., & Ahmad, M. I. (2012). Fly ash porous material using geopolymerization process for high temperature exposure. *International journal of molecular sciences*, 13(4), 4388-4395.
2. Al-Khanbashi, A., MOHAMED, A. O., Moet, A., & Hadi, B. (2000). Stabilization of desert sand using water-born polymers. In *Geoengineering in arid lands* (pp. 143-148).
3. Al-Aghbari, M. Y., Mohamedzein, Y. A., & Taha, R. (2009). Stabilisation of desert sands using cement and cement dust. *Proceedings of the Institution of Civil Engineers-Ground Improvement*, 162(3), 145-151.
4. Ameta, N. K., Wayal, A. S., & Hiranandani, P. (2013). Stabilization of dune sand with ceramic tile waste as admixture. *American Journal of Engineering Research*, 2(9), 133-139.
5. Bilek, V. (2013). Development and properties of concretes with ternary binders. *Cement, Wapno, Beton*, 79, 343-352.
6. Duxson, P., Provis, J. L., Lukey, G. C., & Van Deventer, J. S. (2007). The role of inorganic polymer technology in the development of 'green concrete'. *cement and concrete research*, 37(12), 1590-1597.
7. El Sharief, A. M., Mohamedzein, Y. E., & Hussien, Y. A. (1999). Geotechnical properties of Qoz soils. In *Geotechnics for Developing Africa* (pp. 317-320). CRC Press.
8. Ingles, O. G. (1970). Mechanisms of clay stabilization with inorganic acids and alkalis. *Soil Research*, 8(1), 81-85.
9. Lemougna, P. N., Melo, U. C., Delplancke, M. P., & Rahier, H. (2014). Influence of the chemical and mineralogical composition on the reactivity of volcanic ashes during alkali activation. *Ceramics international*, 40(1), 811-820.
10. Palomo, A., Blanco-Varela, M. T., Granizo, M. L., Puertas, F., Vazquez, T., & Grutzeck, M. W. (1999). Chemical stability of cementitious materials based on metakaolin. *Cement and Concrete research*, 29(7), 997-1004.
11. Alshaer, M., Cuypers, H., & Wastiels, J. (2002, October). Stabilisation of kaolinitic soil for construction purposes by using mineral polymerisation technique. In *Proceedings of the 6th International Conference Technology for Developing Countries* (Vol. 3, pp. 1085-1092).
12. He, P., Wang, M., Fu, S., Jia, D., Yan, S., Yuan, J., ... & Zhou, Y. (2016). Effects of Si/Al ratio on the structure and properties of metakaolin based geopolymer. *Ceramics international*, 42(13), 14416-14422.
13. Rowles, M., & O'connor, B. (2003). Chemical optimisation of the compressive strength of aluminosilicate geopolymers synthesised by sodium silicate activation of metakaolinite. *Journal of materials chemistry*, 13(5), 1161-1165.
14. Slaty, F., Khoury, H., Wastiels, J., & Rahier, H. (2013). Characterization of alkali activated kaolinitic clay. *Applied Clay Science*, 75, 120-125.
15. Van Jaarsveld, J. G. S., Van Deventer, J. S., & Lukey, G. C. (2002). The effect of composition and temperature on the properties of fly ash-and kaolinite-based geopolymers. *Chemical Engineering Journal*, 89(1-3), 63-73.
16. Xu, H., & Van Deventer, J. S. J. (2000). The geopolymerisation of alumino-silicate minerals. *International journal of mineral processing*, 59(3), 247-266.
17. Zhang, Z., Yao, X., & Zhu, H. (2010). Potential application of geopolymers as protection coatings for marine concrete: II. Microstructure and anticorrosion mechanism. *Applied clayscience*, 49(1-2), 7-12.
18. Zhang, Z., Yao, X., & Zhu, H. (2010). Potential application of geopolymers as protection coatings for marine concrete: II. Microstructure and anticorrosion mechanism. *Applied clay science*, 49(1-2), 7-12.

## TRANSMISSION NETWORK EXPANSION PLANNING UNDER DEMAND RESPONSE PROGRAM

P.B. Thote<sup>1</sup>, C. Rathore<sup>2</sup> and M.B. Daigavane<sup>4</sup>

<sup>1,2</sup>S.B. Jain Institute of Technology Management & Research Nagpur, Maharashtra

<sup>3</sup>Technical Education, Regional Office, Nagpur

<sup>1</sup>hodelectrical@sbjit.edu.in, <sup>2</sup>chandrakantrathore@sbjit.edu.in, <sup>3</sup>mdai@rediffmail.com

### ABSTRACT

Several numbers of optimization techniques and new technologies have been implemented on Transmission Network Expansion Planning (TNEP). Due to restructured electricity market different forms of energy saving techniques have been integrated in the system such as demand response (DR), electric vehicles and others. In the presented paper TNEP problem has been analyzed under various DR programs. The objective of this work is to minimize the overall cost of the system. The IEEE 24-bus transmission network has been modified and examined under different cases. The results indicate a significant contribution in the field of proposed study.

**Keywords:** Restructure, Demand response, Cost, Transmission network planning.

### 1. Introduction

From the past few eras, more focus is towards the use or integration of renewable energy sources into the structure of the power system. This is because of the electricity act 2003 and generation of electricity from renewable energy. This results in more tedious job for the transmission network planner. Hence, different optimization techniques have been adopted by the system planner. Also, in order to reduce the overall cost of the system emerging methods have been incorporated in the system. DR is defined as changes in point-user electricity intake templates in line with changes in electricity prices over time compared to their ordinary routine templates (Albadi & El-Saadany, 2008). The execution of DR programs may be configured as a replacement for the generation and transmission extension (Gbadamosi & Nwulu2020). Considering deregulated electricity market adaptation of DR has many advantages. Some forms of DR methods have been explained in (Aalami, Moghaddam, & Yousefi, 2010). A review about different optimization algorithms applied to TNEP problem has been reported in (Ude, Yskandar, & Graham, 2019). Work done so far with regards DR and TNEP has been presented in (Kazerooni & Mutale, 2010, Saxena, & Bhakar, 2019, and Rathore & Roy, 2016). The effectiveness of gbest-guided artificial bee colony (GABC) method has been presented by the authors in (Rathore & Roy, 2016). Therefore, it is considered here.

### 2. Formulation of the Problem

In this work, minimization of multi-objective function is considered. The target is to minimize, the sum of the transmission line investment cost (CTL), the running cost (RC) of generating units and the price of demand response participation (DRC). It is expressed as below:

$$\text{Objective function} = (\text{CTL} + \alpha \times (\text{RC} + \text{DRC})) \quad (1)$$

Terminologies used in (1) are illustrated below: The CTL in (1) represents the amount paid for constructing new transmission line (Romero, Rocha, Mantovani, & Sanchez, 2005) and is expressed as

$$\text{CTL} = \sum_{i,k \in \Omega} \text{CL}_{ik} (nn_{ik}) \quad (2)$$

The RC is the fuel cost of the generating units and expressed as (Rathore & Roy, 2016):

$$\text{RC} = \sum_j^{L_d} \sum_i^{N_g} a_i + b_i P_{gi}^j + c_i (P_{gi}^j)^2 \quad (3)$$

where  $\text{CL}_{ik}$ ,  $a$ ,  $b$  and  $c$  indicates the price of transmission lines, cost coefficients of the generator.

The DRC indicates the cost for  $j^{\text{th}}$  load level of DR contribution (Aalami, Moghaddam, & Yousefi, 2010, Rathore & Roy, 2016) and it is calculated using (4)

$$\text{DRC} = \sum_j^{L_d} \sum_i^{N_b} \text{Ainc}_i^j \times (d_{oi}^j - d_i^j) \quad (4)$$

where  $\alpha$  in eqn. (1) is the weighting factor.

Subjected to the constraints as expressed in (5)-(8).

$$\sum_{v \in N_{lk}} f_i^j - \sum_{v \in N_g} P_{gi}^j = P_{dk}^j \quad k = 1, \dots, N_b \quad (5)$$

$$\sum_{v \in N_{lk}} |f_i^j| \leq (n_i^o + nn_i^j) f_i^{\text{max}} \quad (6)$$

$$P_{gi}^{min} \leq P_{gi}^j \leq P_{gi}^{max} \quad (7)$$

$$0 \leq nn_{ik}^j \leq nn_{ik}^{max} \quad (8)$$

where  $P_g$ ,  $P_d$ ,  $f$ ,  $nn$ , and  $n^o$  represents the power generated, load demand, power flow, new lines and initial number of new lines for the particular bus at defined load level.

New load demand is calculated (Rathore& Roy, 2016) as:

$$d_i^j = d_o^j \times \left\{ 1 + \frac{Elast_i^j \times [Ainc_i^j]}{Spot_i^j} \right\} \quad (9)$$

where  $Ainc$ ,  $d_o$ ,  $d$ ,  $Elast$  and  $Spot$  indicates the incentives offered, initial demand, final demand, elasticity price and spot price for the particular bus at defined load level.

The Independent System Operator is required to pay this amount (DRC) to consumers as a motivation when they are sharing in DR programs. The more details about DR

modeling may be obtained in (Rathore& Roy, 2016).

### 3. GABC Optimization Algorithm

GABC is a well know meta-heuristic optimization technique, it is stimulated by the mutual imaginative action of honey bees when trapping for food. It was invented by Basturk B and Karaboga D (Karaboga& Basturk, 2007). It comprises of 3 non-natural bees groups, i.e. employed bees, onlooker bees and scout bees (Karaboga& Basturk, 2007). The location of every food source indicates a likely & probable solution of the stated optimization problem. The nectar volume of the food source indicates the quality or fitness of the result (Rathore& Roy, 2016). The step-by-step procedure for solving the stated problem is displayed in Figure 1.

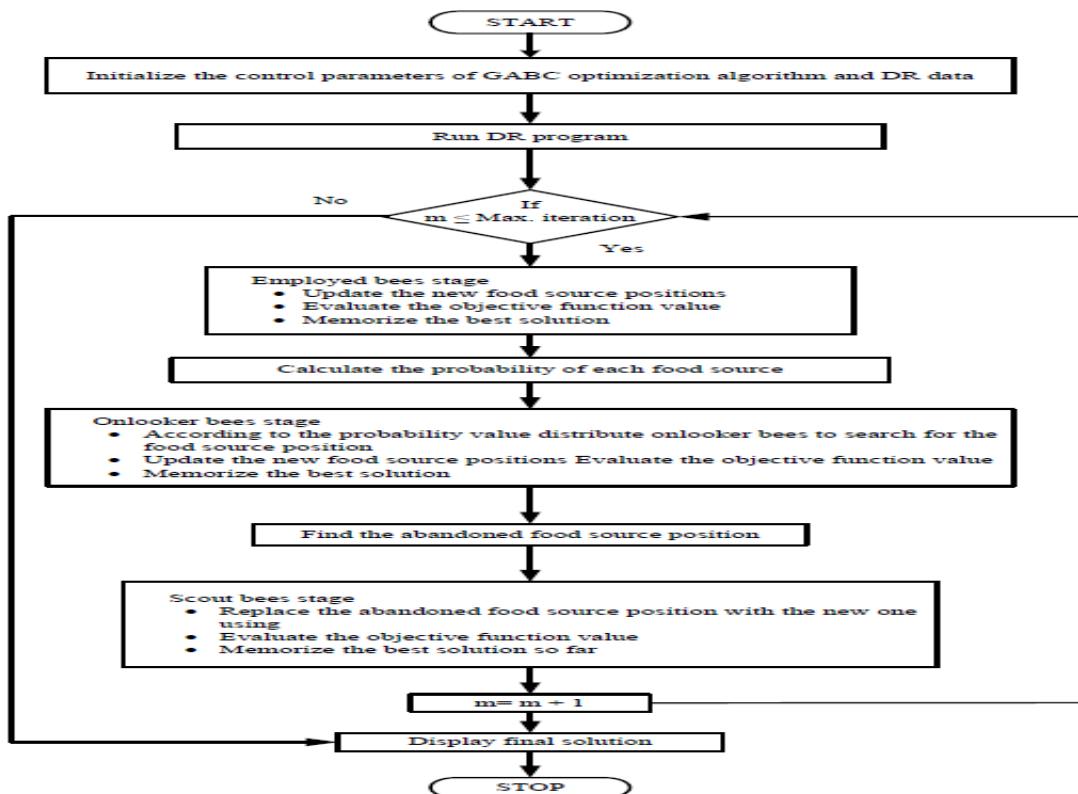


Figure1.Flowchart for the solution proposed problem using GABC technique

### 4. The system considered and results

The proposed problem has been solved in MATLAB platform by implementing the GABC method. The line data and bus data of IEEE 24-bus network are extracted from (Romero, Asada, Carreno, & Rocha, 2007). The generator cost characteristic and the DR program data are extracted from (Ude, & Graham, 2019) and (Albadi & El-Saadany,

2008). The maximum number of new parallel lines is limited to 3. The transmission line parameters are displayed in Table 1.

Five different test cases are examined:

1. In this case the stated example is solved with fixed generation plan.
2. Here, the stated example is solved under generation resizing.

3. The fuel price of the generating entities is considered. demand response program (EDRP) is examined.
- 4 & 5 the impact of the incentive-based Time-of-use (TOU) DR program and Emergency

**Table 1.Line data for IEEE 24-bus system**

Line No	Prob able lines	From bus	To bus	r (resistance) (p.u)	x (reactance) (p.u)	Initial line connected	Max. line flow (MW)	Cost of line (million US \$)
1	L <sub>1-2</sub>	1	2	0.0026	0.0139	1	175	3
2	L <sub>1-3</sub>	1	3	0.0546	0.2112	1	175	55
3	L <sub>1-5</sub>	1	5	0.0218	0.0845	1	175	22
4	L <sub>2-4</sub>	2	4	0.0328	0.1267	1	175	33
5	L <sub>2-6</sub>	2	6	0.0497	0.192	1	175	50
6	L <sub>3-9</sub>	3	9	0.0308	0.119	1	175	31
7	L <sub>3-24</sub>	3	24	0.0023	0.0839	1	400	50
8	L <sub>4-9</sub>	4	9	0.0268	0.1037	1	175	27
9	L <sub>5-10</sub>	5	10	0.0228	0.0883	1	175	23
10	L <sub>6-10</sub>	6	10	0.0139	0.0605	1	175	16
11	L <sub>7-8</sub>	7	8	0.0159	0.0614	1	175	16
12	L <sub>8-9</sub>	8	9	0.0427	0.1651	1	175	43
13	L <sub>8-10</sub>	8	10	0.0427	0.1651	1	175	43
14	L <sub>9-11</sub>	9	11	0.0023	0.0839	1	400	50
15	L <sub>9-12</sub>	9	12	0.0023	0.0839	1	400	50
16	L <sub>10-11</sub>	10	11	0.0023	0.0839	1	400	50
17	L <sub>10-12</sub>	10	12	0.0023	0.0839	1	400	50
18	L <sub>11-13</sub>	11	13	0.0061	0.0476	1	500	66
19	L <sub>11-14</sub>	11	14	0.0054	0.0418	1	500	58
20	L <sub>12-13</sub>	12	13	0.0061	0.0476	1	500	66
21	L <sub>12-23</sub>	12	23	0.0124	0.0966	1	500	134
22	L <sub>13-23</sub>	13	23	0.0111	0.0865	1	500	120
23	L <sub>14-16</sub>	14	16	0.005	0.0389	1	500	54
24	L <sub>15-16</sub>	15	16	0.0022	0.0173	1	500	24
25	L <sub>15-21</sub>	15	21	0.0063	0.049	2	500	68
26	L <sub>15-24</sub>	15	24	0.0067	0.0519	1	500	72
27	L <sub>16-17</sub>	16	17	0.0033	0.0259	1	500	36
28	L <sub>16-19</sub>	16	19	0.003	0.0231	1	500	32
29	L <sub>17-18</sub>	17	18	0.0018	0.0144	1	500	20
30	L <sub>17-22</sub>	17	22	0.0135	0.1053	1	500	146
31	L <sub>18-21</sub>	18	21	0.0033	0.0259	2	500	36
32	L <sub>19-20</sub>	19	20	0.0051	0.0396	2	500	55
33	L <sub>20-23</sub>	20	23	0.0028	0.0216	2	500	30
34	L <sub>21-22</sub>	21	22	0.0087	0.0678	1	500	94
35	L <sub>1-8</sub>	1	8	0.0348	0.1344	0	175	35
36	L <sub>2-8</sub>	2	8	0.0328	0.1267	0	175	33
37	L <sub>6-7</sub>	6	7	0.0497	0.192	0	175	50
38	L <sub>13-14</sub>	13	14	0.0057	0.0447	0	500	62
39	L <sub>14-23</sub>	14	23	0.008	0.062	0	500	86
40	L <sub>16-23</sub>	16	23	0.0105	0.0822	0	500	114
41	L <sub>19-23</sub>	19	23	0.0078	0.0606	0	500	84

The simulation results for all the five cases are tabulated in Table 2. A detailed result for each case is interpreted below:

**Case-1 and Case-2:**

It is noted from the results that the CTL is less in case-2 in comparison with case-1. Case-2 saves  $238 \times 10^6$  US \$. These indicate as the generation values are varied between its lower

to upper range the reach for yielding the optimal solution also increases.

The fitness characteristic for both the cases is displayed in Figure. 2. It is noted that the algorithm attained the optimal solution in less number iterations. These represent the effectiveness of the algorithm.

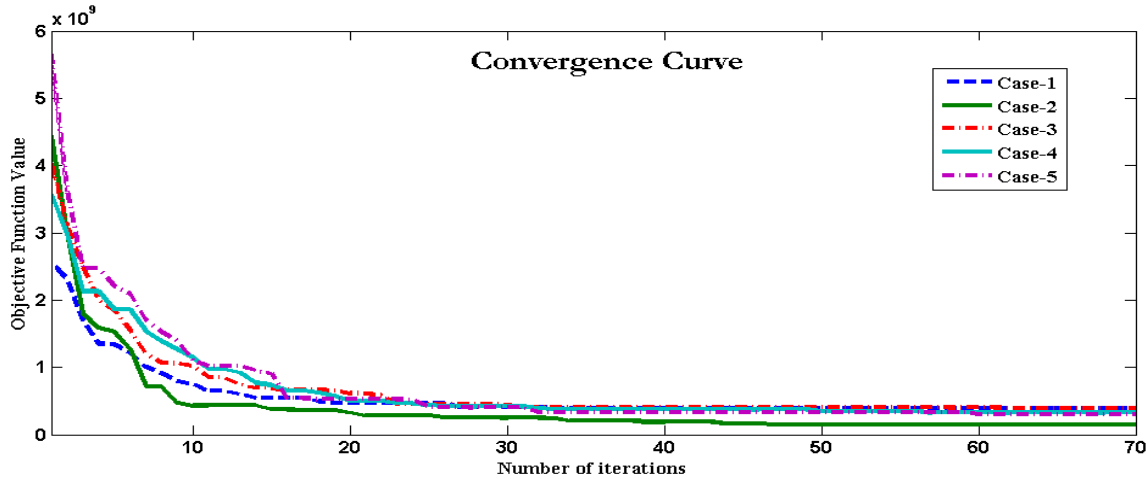


**Figure 2. Cost Convergence Curves**

**Case-3:** In this case, it is noted that with the inclusion of the running cost of the generating units the total cost of the system has increased by  $184 \times 10^6$  US \$ with regards to case-2 study.

**Case-4 and Case-5:** In both the cases after implementation of DR programs, it is noted the load demand reaches to 8122.5 MW from 8550 MW. With implementation of TOU program,

the transmission line cost, the running cost and the total cost has reduced to 55%, 17% and 53% as compared with case-3 respectively. Similarly, after EDRP the transmission line cost, the running cost and the total cost has reduced to 56%, 13% and 55% as compared with case-3 respectively. The load characteristics after implementation of DR program is displayed in Figure 3.

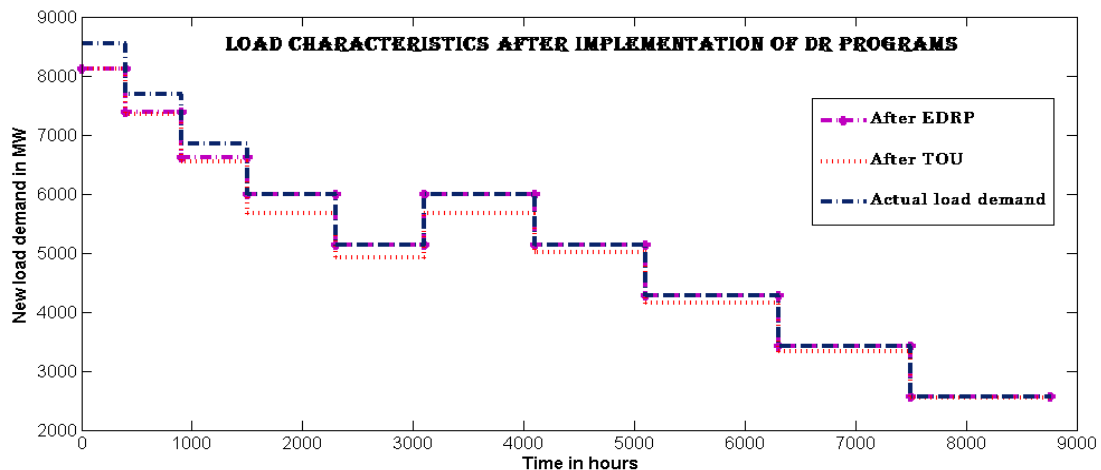


**Figure 3. Load Curves after DR Implementation**

The implementation of EDRP saves  $8 \times 10^6$  US \$ &  $7 \times 10^6$  on the transmission line cost as compared with TOU. Data presented in Table 2 represents that the EDRP program gives better

results than TOU-DR. The details of new transmission lines connected for all the cases are displayed on Table 3.

**Table 2: Overall Results**

Cases	Results				
	CTL (US \$)	RC US (\$)	DRC (US \$/h)	TC (US \$)	Total new lines added
1	390,000,000	-	-	390,000,000	12
2	152,000,000	-	-	152,000,000	5
3	322,000,000	14,585,959.889	-	336,585,959.889	8
4	144,000,000	11,993,734.76	31,153	156,024,887.8	4
5	136,000,000	12,628,945.3	17,881	148,646,826.3	5

**Table 3. Details of New Transmission Lines Added for All the Cases**

Cases	Total new lines added	Details
1	12	$L_{1-5}$ (1), $L_{3-24}$ (1), $L_{6-10}$ (1), $L_{7-8}$ (2), $L_{14-16}$ (1), $L_{15-24}$ (1), $L_{16-17}$ (2), $L_{16-19}$ (1), $L_{17-18}$ (2)
2	5	$L_{6-10}$ (1), $L_{7-8}$ (2), $L_{10-12}$ (1), $L_{14-16}$ (1)
3	8	$L_{2-6}$ (2), $L_{3-24}$ (1), $L_{7-8}$ (2), $L_{9-12}$ (1), $L_{14-16}$ (1), $L_{16-17}$ (2)
4	4	$L_{6-10}$ (1), $L_{7-8}$ (2), $L_{10-12}$ (1), $L_{13-14}$ (1)
5	5	$L_{1-5}$ (1), $L_{6-10}$ (1), $L_{7-8}$ (2), $L_{11-13}$ (1)

The comparison between other optimization techniques with the presented method is displayed in Table 4. It is noted that the GABC

method is able to obtain the optimal result as compared with other methods.

**Table 4. Result Comparison Table for Cases 1 and 2**

Methods	Transmission line cost (US \$)	
	IEEE 24-bus system	
	Case-1	Case-2
B-and-B (Romero, Asada, Carreno, & Rocha, 2007)	-	152,000,000
HSA (Verma, anigrabi, & Bijwe, 2010)	390,000,000	-
CHA (Romero, Rocha, Mantovani, & Sanchez, 2005)	438,000,000	-
New DA (Fang & Hill, 2003)	-	224,000,000
CBGA (Silva, Rider, Romero, Garcia & Murari, 2005)	-	152,000,000
<b>GABC</b>	<b>390,000,000</b>	<b>152,000,000</b>

**Conclusion**

It is noted from the overall results that the implementation of DR helps in reduction of the overall cost of the system. The major points concluded from all the cases studied are as:

- For the cases-1 and 2, the results obtained are compared with the existing literatures.

On comparing it is noted that the GABC algorithm achieve a better (i.e., minimum) the CTL than optimization techniques such as CHA for case-1 and New DA for case-2. However, the CTL found is similar in nature with B-and-B, HSA and CBGA methods for cases 1 and 2.



- With implementation of demand response the load profile has been changed which leads to reduction in the fuel cost, the transmission line cost and the total cost.
- It is noted that the gives EDRP better results than TOU-DR program.

### References

1. Aalami, H. A., Moghaddam, M. P., & Yousefi, G. R. (2010). Demand response modeling considering interruptible/curtailable loads and capacity market programs. *Applied Energy*, 87(1): 243-250.
2. Albadi, M. H., & El-Saadany, E. F. (2008). A summary of demand response in electricity markets. *Electric power systems research*, 78(11): 1989-1996.
3. Fang, R., & Hill, D. J. (2003). A new strategy for transmission expansion in competitive electricity markets. *IEEE Transactions on power systems*, 18(1), 374-380.
4. Gbadamosi, S. L., & Nwulu, N. I. (2020). A multi-period composite generation and transmission expansion planning model incorporating renewable energy sources and demand response. *Sustainable Energy Technologies and Assessments*, 39:100726.
5. Karaboga, D., & Basturk, B. (2007). A powerful and efficient algorithm for numerical function optimization: artificial bee colony (ABC) algorithm. *Journal of global optimization*, 39(3): 459-471.
6. Kazerooni, A. K., & Mutale, J. (2010, June). Network investment planning for high penetration of wind energy under demand response program. In *2010 IEEE 11th International Conference on Probabilistic Methods Applied to Power Systems* (pp. 238-243). IEEE.
7. Rathore, C., & Roy, R. (2016). Impact of wind uncertainty, plug-in-electric vehicles and demand response program on transmission network expansion planning. *International Journal of Electrical Power & Energy Systems*, 75: 59-73.
8. Rider, M. J., Garcia, A. V., & Romero, R. (2008). Transmission system expansion planning by a branch-and-bound algorithm. *IET generation, transmission & distribution*, 2(1): 90-99.
9. Romero, R., Asada, E. N., Carreno, E., & Rocha, C. (2007). Constructive heuristic algorithm in branch-and-bound structure applied to transmission network expansion planning. *IET generation, transmission & distribution*, 1(2), 318-323.
10. Romero, R., Rocha, C., Mantovani, J. R. S., & Sanchez, I. G. (2005). Constructive heuristic algorithm for the DC model in network transmission expansion planning. *IEE Proceedings-Generation, Transmission and Distribution*, 152(2): 277-282.
11. Saxena, K., & Bhakar, R. (2019). Impact of LRIC pricing and demand response on generation and transmission expansion planning. *IET Generation, Transmission & Distribution*, 13(5): 679-685.
12. Silva, I. D. J., Rider, M. J., Romero, R., Garcia, A. V., & Murari, C. A. (2005). Transmission network expansion planning with security constraints. *IEE Proceedings-Generation, Transmission and Distribution*, 152(6): 828-836.
13. Ude, N. G., Yskandar, H., & Graham, R. C. (2019). A comprehensive state-of-the-art survey on the transmission network expansion planning optimization algorithms. *IEEE Access*, 7: 123158-123181.
14. Verma, A., Panigrahi, B. K., & Bijwe, P. R. (2010). Harmony search algorithm for transmission network expansion planning. *IET generation, transmission & distribution*, 4(6): 663-673.

